3-2022

Characterizing Wake Roll-Up and Vortex Structure for Delta Wing Configuations Featuring Flow Control Devices at Low Reynolds Number

Jeffrey M. Layng

Characterizing Wake Roll-Up and Vortex Structure for Delta-Wing Configurations Featuring Flow-Control Devices at Low Reynolds Number

THESIS

Jeffrey M. Layng, Capt, USAF

AFIT-ENY-MS-22-M-303

DEPARTMENT OF THE AIR FORCE
AIR UNIVERSITY

AIR FORCE INSTITUTE OF TECHNOLOGY

Wright-Patterson Air Force Base, Ohio

AFIT-ENY-MS-22-M-303

CHARACTERIZING WAKE ROLL-UP AND VORTEX STRUCTURE FOR DELTA-WING CONFIGURATIONS FEATURING FLOW-CONTROL DEVICES AT LOW REYNOLDS NUMBER

THESIS

Presented to the Faculty

Department of Aeronautics and Astronautics

Graduate School of Engineering and Management

Air Force Institute of Technology

Air University

Air Education and Training Command

in Partial Fulfillment of the Requirements for the

Degree of Master of Science in Aeronautical Engineering

Jeffrey M. Layng, BS

Capt, USAF

March 24, 2022

AFIT-ENY-MS-22-M-303

CHARACTERIZING WAKE ROLL-UP AND VORTEX STRUCTURE FOR DELTA-WING CONFIGURATIONS FEATURING FLOW-CONTROL DEVICES AT LOW REYNOLDS NUMBER

THESIS

Jeffrey M. Layng, BS
Capt, USAF

Committee Membership:

Lt Col Michael M. Walker, PhD
Chair

Dr. Mark Reeder
Member

Maj John Hansen, PhD
Member

Adedeji B. Badiru, PhD
Dean, Graduate School of Engineering and Management

Abstract

Various configurations of a cropped delta wing featuring a NACA 0012 wing-section were evaluated experimentally at a Reynolds number of 5.0 x 10^5 in the Air Force Institute of Technology Low-Speed Wind Tunnel facility. The effects of active flow control (AFC) and passive boundary-layer fences (BLF) were shown to improve high angle of attack delta wing performance. The AFC BLFs were shown to replicate the performance enhancements found in passive BLFs without incurring a drag penalty. An experimental characterization of the wake region is presented to compare the wake roll-up and leading edge vortices for these baseline, passive BLF, and AFC BLF delta wing configurations. Using a tuft mesh and a constant temperature anemometry triple wire probe, the wake was characterized at several discrete planes of interest aft of the trailing edge. This wake data was used to visually examine causes for AFC BLF configuration's 60.3% increase in maximum lift coefficient. The present study shows this aerodynamic improvement is largely attributed to strengthening the leading edge vortex (LEV) and truncating spanwise flow common to delta wings. Both of these phenomena delay the breakdown of the primary LEV and thereby the global wing stall. The presence of either an active or passive boundary layer fence is shown to shift the core of the LEV inboard and increase the coherence of the wing tip vortex and LEV. As the angle of attack increases, these vortex cores migrate toward the wing tip. Initial breakdown of the primary LEV begins about 4.5" aft of the trailing edge.

This research coincided with unprecedented difficulty for the whole earth in the form of pestilence, wars, and rumors of wars. As creation groans, I have become acutely aware of my dependence on the Lord Jesus Christ for mercy and grace to even face another day. In Him I live, move, and have my being. I am so grateful and undeserving of His faithfulness and provision of my daily bread. He is my portion.

I would like to dedicate this thesis to my beautiful and patient wife for her tireless support while I holed up for hours on end, studying, collecting data, and writing like a madman. I would like to thank my precious daughter for the consistent moral support in the form of giggles, smiles, and poopy diapers.

Also, for my day-one boys, Jinhee Byun and Ross Kellet. Couldn't have done it without you.

Acknowledgements

I would like to thank Lt Col Walker for his guidance and assistance throughout the whole of his AFIT experience. Lt Col Walker has been a tremendous support, both in and out of the classroom, regarding research advice as well as professional advice. His mentorship and support through these difficult months has been a gracious gift from the Lord.

I also owe a massive debt of gratitude to Maj Shawn Naigle for his generous support of this research. He conducted all of the computational runs used in this experiment, without which the research would have been far less compelling. The computational data reported in this study was collected in part by a grant of computer time from the DoD High Performance Computing Modernization Program at ERDC DSRC.

I would also like to thank Dr. Reeder for the tremendous help, at all hours of the day, in debugging strange wind tunnel matters, discussing questionable results, and for helping refine the scope of this open-ended research topic. Thank you for helping to constrain the matter and focus on what was important.

I also would like to thank Maj John Hansen for his advice in writing and finishing this thesis.

Thank you to Dr. Aaron Altman from AFRL for sponsoring this research and for all of his aerodynamic and experimental insight needed to collect the data.

Jeffrey M. Layng

Table of Contents

Page

List of Figures

List of Tables

CHARACTERIZING WAKE ROLL-UP AND VORTEX STRUCTURE FOR DELTA-WING CONFIGURATIONS FEATURING FLOW-CONTROL DEVICES AT LOW REYNOLDS NUMBER

I. Introduction

1.1 Motivation and Background

The 2018 National Defense Strategy (NDS) describes the urgency required in modernizing the US military in order to facilitate a credible deterrent in the present threat environment. Peer adversaries are advancing technologically and tactically, refining their strategies, and are rapidly closing the air superiority gap once held by the US. To maintain a competitive edge, the NDS calls for building a more lethal force. In order to do this, the document calls for modernizing key capabilities. Accomplishing this end requires that "[i]nvestments will prioritize ground, air, sea, and space forces that can deploy, survive, operate, maneuver, and regenerate in all domains while under attack" (2018 NDS).

Similarly, in 2021 address to the House Armed Services committee, the Undersecretary of the Air Force for Acquisitions, Technology, and Logistics, recognized that the Air Force "must accelerate change to its fighter force structure to meet the threat posed by China and Russia, ensuring the Air Force can achieve air superiority and dominance over peer adversaries" (SAF/AQ). As a part of this clearly stated goal to achieve and maintain air superiority and dominance, the Air Force invests much time, effort, and money into research. The technology required to maintain superiority is multidisciplinary; electronics, mechanics, aerodynamics, a host of human factors, and

logistics problems present themselves as hurdles required to overcome. Adversaries are working equally as hard to gain competitive advantage over the US in aerial combat. The nation that can deny its enemy use of the air and space can effectively deny them any advancement at all.

The present study investigates flow control technology that can be used to augment aerodynamic performance of delta-wing aircraft. As discussed in the 2018 NDS, "maneuverability", agility, and superlative performance is demanded of our fighter force to maintain air superiority and dominance.

Delta wings are prominently featured on early and modern fighter aircraft because of their aerodynamic advantages that make them suited for fast and agile flying. Hitzel et al. (2016) describes their benefits as a unique combination of "docile" take-off and landing characteristics and "enhanced agility" and performance in trans- and supersonic flight conditions. Continually optimizing performance in US weapon systems is required to maintain competitive advantage in the skies. For this reason, there is much interest in understanding the driving aerodynamic mechanisms used to keep these aircraft competitive. Understanding the nuanced phenomena that allow for engineers to expand the flight envelope for similar platforms and improve their utility is important to military strategists and tacticians alike. Delta wings induce leading-edge vortices (LEV) by which they decrease pressure on the upper surface. These vortices result in increased lift performance at higher angles of attack (AoA) compared to straight and swept rectangular wings.

Vortex generation, propagation, and breakdown is especially important for delta wings because of their centrality in their performance at high angles of attack. Stability issues have been known to arise from unsteadiness associated with breakdown (wing rock) as well as a tendency for abrupt stall. Both of these issues are critical and require great attention and knowledge to address in sustainment and future de-

velopment of delta-wing aircraft. Hitzel et al. (2016) again describes past efforts to overcome such delta wing challenges by the use of active passive, dynamical control devices, such as slats, spoilers, and other pneumatic devices. The greater the sweep angle of delta-wing configurations, he argues the greater need for more elaborate methods of improving these shortcomings. The present study aims to investigate application of momentum-adding active flow control (AFC) devices on rounded-leading edge delta wings with cropped wing tips.

It has been shown in previous research [Walker, Demoret, Tedder] that the use of both passive and active flow control devices can be used to prevent the propagation of spanwise flow, delay separation, and ultimately increase the maximum lift angle of attack. Active flow control applications have the advantage of being able to be activated only when needed, thereby reducing possible disadvantages in off-design conditions.

1.2 Problem Statement

The present study intends to characterize the wake of cropped delta-wing configurations featuring different flow control devices. All the configurations in this study feature NACA 0012 wing sections. Where as past research efforts have shown that performance enhancements can be expected with the use of active flow control devices, the present study intends to explain why.

1.3 Research Questions

The present study will seek to qualitatively and qualitiatively explain the performance enhancements noted in Demoret's and Tedder's work by examining the near-body wake. Ultimately, the question regarding the importance of truncating spanwise flow and energizing leading edge vortices.

This study also aims to characterize the evolution of the leading edge voritices as the angle of attack increases and the vortex propagates downstream. Mean velocity values in all three cartesianal directions, turbulence intensity, turbulent kinetic energy, and vorticity will discussed.

Additionally, flow features are will be qualitatively compared to show magnified how certain configurations result in larger flow field changes, comparing passive flow control to active flow control to the baseline configuration.

1.4 Assumptions and Limitations

The active flow control device used in this research effort relies on pressurizing chambers within the wings and ejecting that air through slots in the wing surface. It will be shown that the assumption of uniform flow does not hold true, as its profile was determined by means of Schlieren imagery. The jet profile was similar in uniformity to Walker's swept wing jet.

II. Literature Review

A review of literature pertaining to active flow control (AFC) boundary-layer fences (BLF) is presented in this chapter. Special emphasis is placed on aerodynamic theory pertaining to delta-wing performance, vortex generation, decay, and breakdown, passive boundary-layer fences, and related applications of active flow control. Delta wings rely on such vortices as their primary source of lift, as the vortex cores are regions of low pressure.

2.1 Wing Geometry Comparisons

While wing-sections and finite-wings generate lift in similar manners, three-dimensional (3D) effects present in finite wings introduce a layer of complexity that compounds when considering geometric properties. A notional comparison of two-dimensional (2D) and 3D flow scenarios offers insight into complexity present in the wake of even the most simple wing designs. Small alterations in geometric configuration can impact the downstream flow field, wake, and ultimately the global force coefficients of the body dramatically. Unintended alterations to geometry can adversely impact aerodynamic performance while carefully tuned modifications can decrease drag, increase lift, and even delay stall. Understanding the physical phenomena that account for such performance changes is necessary when postulating about flow control implemented to augment a flow field.

This section will compare wing sections, straight and swept rectangular finite wings, and delta wings in order to lay the groundwork for understanding the mechanisms of influencing the flow field of a delta-wing geometry. These fundamental aerodynamic principles will aid the discussion of experimental setup and ultimately provide a framework for understanding the results of the study. These principles will

also be drawn on to postulate on the effects of AFC BLF application. This discussion will systematically present relevant theory necessary for application of AFC in this research.

There are differences worth noting with respect to the mechanisms of generating lift in straight wings, swept wings, and delta wings, as compared in Figure 1.Tracing a streamline over a straight wing, it is evident the path predictably follows the contours of the wing surface, namely the shape of the airfoil. Swept wings alter the angle experienced by the impinging flow. The wing perceives this shifted angle as spanwise flow, which effectively decreases the lift of the wing. Delta wings similarly experience this offset angle, but the penalty on lift is not as dramatic due to the according change in chord. The longer inboard chord length at the wing root makes up for the drop in effective left caused by spanwise flow at low angles of attack.

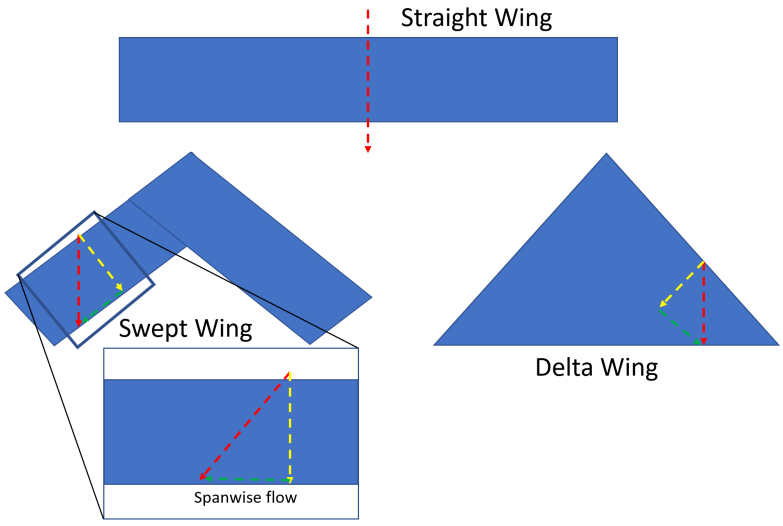

Figure 1. Planform comparison of straight wings, swept wings, and delta wings

Wing-sections, and to a lesser extent straight, high aspect-ratio wings, generate lift by maintaining velocity differences on the top and bottom surface, which drives differences in pressure and ultimately generates force perpendicular to the freestream velocity. Air traversing over the top of an airfoil accelerates and causes a drop in static

pressure. Conversely, the impinging flow on the bottom accelerates less than the top, resulting in a relatively higher pressure. The lift force, normal to the direction of freestream velocity, is directly attributed to this pressure difference, and ultimately caused by the net 'turning' of the flow. As the AoA increases for three-dimensional, finite wings, the tendency for flow to move from high to low pressure regions is exaggerated, which results in increased spanwise flow and strengthened wingtip vortices. Both phenomena contribute to decreasing lift (Anderson, 2017).

The spanwise pressure gradients appear because of the staggered pressure profiles along the wing, tapered back by the wing sweep. Demoret et al. (2020) discusses this phenomena in sufficient detail for the scope of this description. Figure 2 shows this clearly with the offset peaks aligned in the direction of the sweep. It is because of these offset pressure peaks that impinging flow turns outboard, since fluids always move in the direction of lower pressure regions. In the case of a backward swept wing, this motion is always outboard (Harper and Maki, 1964).

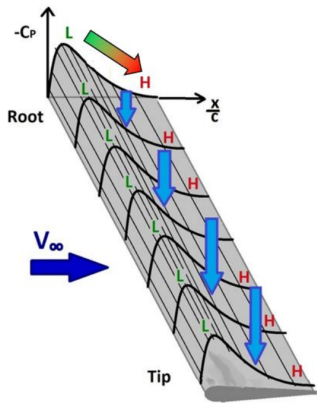

Figure 2. Staggered pressure profiles on swept wing (Demoret, 2020)

Stall characteristics of swept wings were first investigated in 1935 by Adolf Busemann, a German aerodynamicist, who showed that normal and tangential components of the flow traversing the wing could be treated as independent of each other (Anderson, 2017). The normal component, flow parallel to the chord, is primarily responsible

for the lift generation, while the tangential component, perpendicular to the chord, detracts from the lift force because it does not result in net turning of the flow over the wing. Spanwise flow is said to be more prominent near the wingtips, corresponding to a tendency for wingtips to stall before inboard locations. For control in the roll direction, dependent on aileron effectiveness, this phenomenon can be especially problematic (Anderson, 2017).

Lift coefficient for two-dimensional (infinite span) wing sections increases predictably as the angle of attack (AoA) increases until a given angle when flow on the top of the airfoil (or suction surface) separates, diminishing the lift coefficient for subsequent increases in AoA. The wing section is said to be stalled at such a point. The two-dimensional case is ideal for lift generation because there is no wing tip from which to ease the pressure gradient between the top and bottom surface. Considering the presence of a wingtip, aerodynamicists observe three-dimensional relieving effects that decrease the efficiency of a wing in flight. As the AoA increases, these relieving effects eventually result in flow exchanging streamwise motion for spanwise motion, which decreases rate at which lift coefficient varies with changes in AoA, or $C_{L\alpha}$. Additional losses are noted near the wing tips (Anderson, 2017).

Another important phenomenon brought on by three-dimensionality is the pressure difference between the top and bottom surfaces. This gradient drives the flow to equalize, which induce wingtip vortices. The combination of these wing-tip vortices and the spanwise flow instigated by staggered pressure profiles leads to greater aerodynamic inefficiencies compared to wing sections. These effects lower the $C_{L\alpha}$ and advance the onset of stall. Figure 3 shows how finite wings lose some of the pressure advantage to pressure gradients. The propagation of spanwise flow is driven by the high pressure air on the bottom surface spilling over the wingtip to the low-pressure suction surface. The result of this motion is a high-energy wingtip vortex that reduces

productive energy and leads to inefficiencies absent in two-dimensional wing sections (Anderson, 2017).

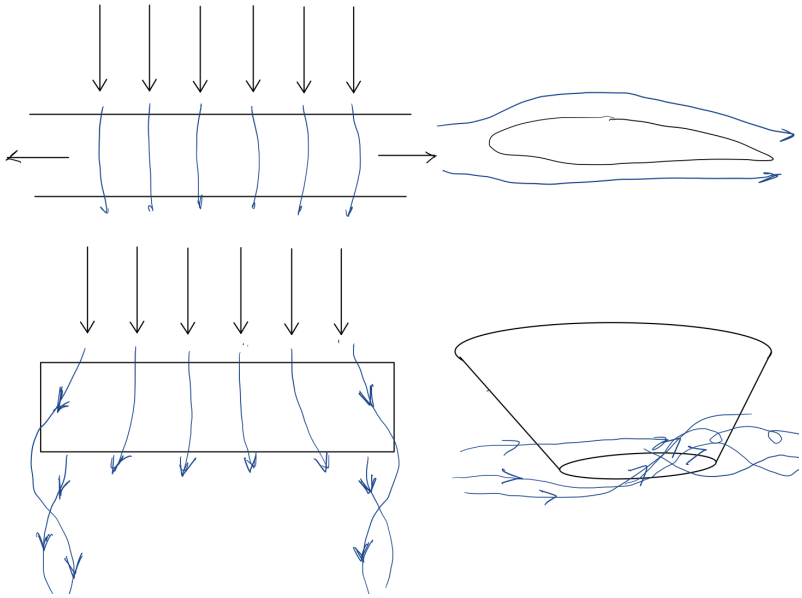

Figure 3. Comparison of 2-D and 3-D wings

Aerodynamic analysis is further complicated by considering the effects of wing sweep. Straight wings present freestream flow a right angle over which flow can traverse normally. When a wing is swept, the wing is presented to the freestream flow off-angle, which decreases lift, mimicking the effect of spanwise flow. Highly swept wings are often implemented in supersonic aircraft to reduce wave drag in the transonic and supersonic flight regimes by eliminating any part of the geometry protruding into the "Mach cone". This Mach cone is the result of a primary shockwave from the aircraft and is a function of surface inclination angle and Mach number. It can be treated as a significant discontinuity around which many losses occur and the drag spikes (Anderson, 2017).

Anderson thoroughly describes wave drag and supersonic design considerations in his treatment of compressible flow (Anderson, 2017). Due to the low-speed, incompressible nature of this study, this compressible flow discussion serves as reasons for

seeing swept wings in modern aircraft. Ultimately it is to increase the critical Mach number of an aircraft. Nevertheless, aircraft designed for high subsonic, transonic, and supersonic flight must of course be operable in low-subsonic conditions for important flight regimes (takeoff, landing, cruise, etc). Except for very few variable sweep designs, of which there are several prominent examples (F-111, B-1, MiG-27, Su-24, and), wing sweep in an aircraft is generally a fixed attribute (Anderson, 2017).

Delta wings are a special case of swept wings in which the trailing edge joins the fuselage perpendicularly from the wingtips to form an enclosed triangular shape. A generalized delta-wing geometry is shown in Figure 1. Most modern fighter aircraft feature delta wings for supersonic flight considerations, namely they reduce the wave drag at high Mach numbers and increase the maximum lift coefficient. Anderson goes on to describe that, while these aircraft are designed with supersonic missions in mind, they spend a considerable percentage of their time aloft in the subsonic flight regime (i.e. takeoff, cruise, air refueling, and landing). For that reason, special considerations of subsonic delta-wing performance is needed.

At high angles of attack, delta wings generate lift primarily by inducing leading-edge vortices (LEV). Figure 4 shows this generalized phenomena and presents a dissected view to show the direction of curl and subsequent separation region. The high energy vortex cores result in low-pressure regions on the suction surface (Anderson, 2017).

Delta wings facilitate high-energy, high-vorticity flow in the core of the vortices which create low pressure regions that contribute significantly to the lift of the wing. This is caused by strong pressure gradients near the leading edge that cause a curling of flow from the high pressure region to the low pressure. For increasing angles of attack, the vortex is strengthened and moves outboard until finally it detaches and breaks down, resulting in wing stall. The outboard motion of the vortex is indicative

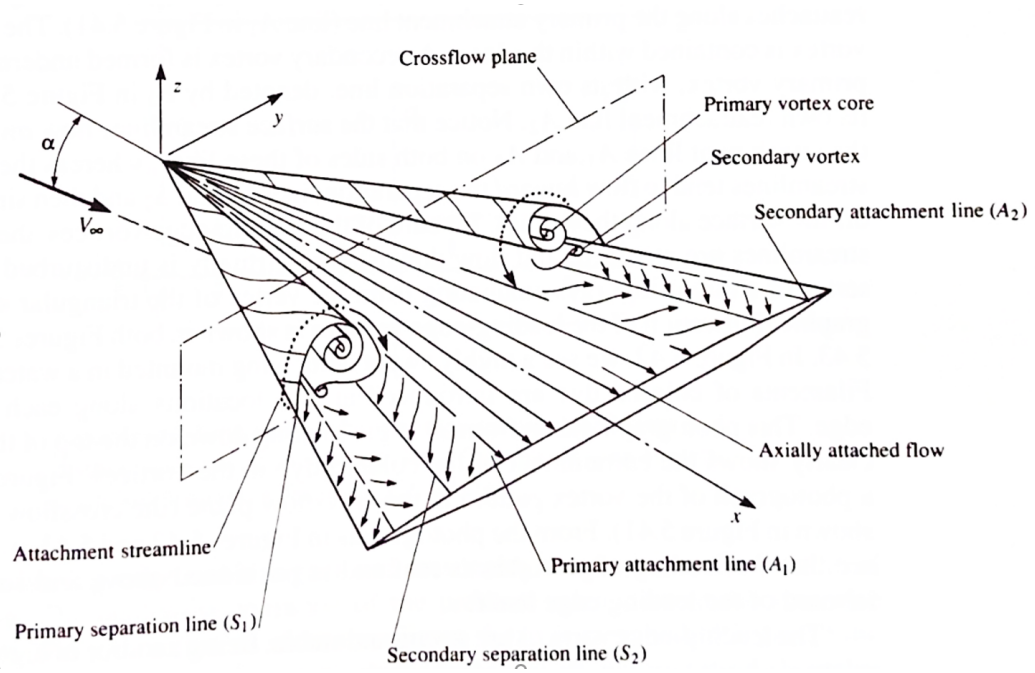

Figure 4. Schematic of the subsonic flow field over the top of a delta wing at angle of attack, (Anderson, 2017)

of spanwise flow, a primary cause for the stall of the wing (Anderson, 2017).

2.2 Aerodynamic Flow Control

Flow control is a discipline within the field of aerodynamics that is predominantly concerned with manipulating a flow field to improve aerodynamic performance. While there are many mechanisms able to manipulate flow fields, applications of flow control generally fall into one of two categories: passive and active. Passive flow control devices are geometric alterations that are used to manipulate flow patterns and active flow control devices are momentum-adding or -subtracting devices used to energize or passify the flowfield to obtain a desired performance change. These two methods form the basis of methods for manipulating the flow around an air vehicle. These mechanisms have been shown to delay transition, postpone separation, enhance lift, reduce drag, and modify turbulence (Gad-el Hak, 2000). The present study is primarily concerned with the comparison of passive and AFC BLFs. Passive flow control has been demonstrated and successfully implemented for decades. As modern computing technology enables use of robust control systems, AFC methods have become more accessible. There is now heightened interest in research, development, and implementation of AFC technology.

2.2.1 Passive Flow Control

Boundary-layer fences (BLF) are an application of passive flow control, and are generally implemented to truncate spanwise flow and prevent the onset of separation. Vortex decay and bulk spanwise flow are two primary causes of stall for delta-wing aircraft. The onset of stall for delta wings is preceded by increasing the volume of spanwise flow and closely followed by vortex breakdown, and for this reason, the wing stall is often associated with the propagation of this spanwise flow. Figure 5 shows this phenomenon on a notional swept wing.

Modern fighter aircraft rely on superior aerodynamic performance in combat to

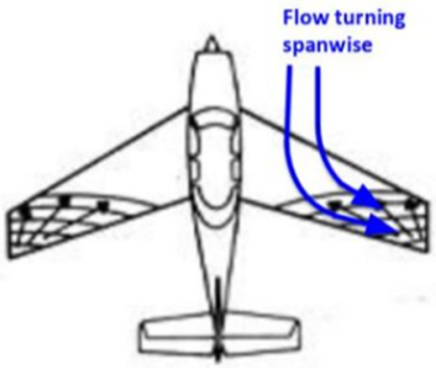

Figure 5. Schematic of the propagation of stall and spanwise flow, taken from Demoret (2020)

out-maneuver enemy aircraft as well as anti-aircraft missiles. For this reason, there are many research efforts currently aimed at improving high AoA performance of delta-wing configurations. Boundary-layer fences were implemented on many notable second-generation fighter aircraft to address the propagation of spanwise flow at high angles of attack. Boundary-layer fences delay propagation of spanwise flow and constrain the flow to streamlines in a manner that delay separation (Demoret, 2020). It was later observed in an optimization study that the outboard location of the fences plays an important role in effectively delaying separation and by consequence wing stall (Tedder, 2021). Figure 6 describes how BLFs truncate spanwise flow by caging streamlines, thereby postponing flow separation. The BLFs effectively serve as guardrails to keep flow in its lane.

There exists a technical tradeoff for engineers to prioritize either aircraft performance or efficiency. While passive boundary-layer fences can improve performance by delaying stall, they present a design challenge: they retain a drag penalty regardless of the phase of flight, whether the BLF advantage is needed or not. To achieve the aerodynamic improvement enabled by the use of passive BLFs while not incurring a persistent drag penalty, engineers have experimented with various technical alterna-

tives. The most notable alternative, and most applicable to this thesis, is the use of AFC to mimic the effects afforded by conventional passive BLFs. Such flow-control mechanisms require minimal changes to streamlined geometry and thus incur minimal increase in the drag polar. Additionally, the actuators can be toggled on-demand to optimize system resources. An added advantage to removing a physical passive BLF is that it decreases the radar cross-section (RCS) (Demoret, 2020). Considerations of the challenges of full-scale implementation, such as weight penalties and sourcing the necessary compressed air, are outside the scope of this study.

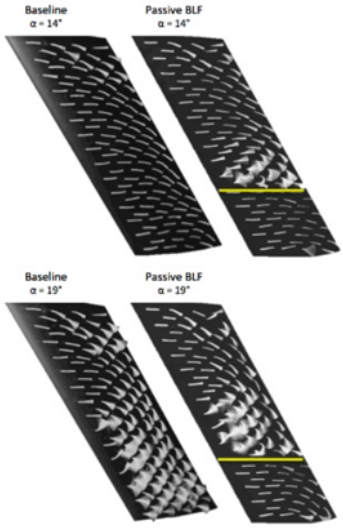

Figure 6. Experimentally tested swept wings comparing baseline to BLF configuration pre- and post-separation Demoret (2020)

Demoret studied the effect of varying the spanwise locations of passive BLFs on maximum lift coefficient C_{Lmax}, an important parameter considering its immediate relation to the stall angle of attack. Naturally, aircraft that can delay stall to higher angles of attack are able to outmaneuver aircraft that cannot. The competitive edge for aerodynamic performance rests greatly in an aircraft's ability to stave off stall and maintain controlled flight, ultimately expanding the flight envelope. All testing was conducted in the AFIT low-speed wind tunnel using a six degree-of-freedom (DoF)

force balance to record aerodynamic coefficients (Demoret, 2020). The results showed an 8.9% improvement of C_{Lmax} in the configuration where the fence was positioned at 70% span.

Williams et al. (2010) discuss the effects of passive BLFs on the performance of a T-38 Talon. The study was conducted computationally, experimentally, and in flight test in order to validate the results of each. Noteworthy differences between the configurations tested in Williams et al. (2010) and the scope of this thesis is the wing geometry and consideration of a fuselage. The T-38 features a far less swept wing, so the delta-wing aerodynamic theory discussed earlier is not entirely applicable. Nevertheless, there are several valuable takeaways (Williams et al., 2010). Experimental wind tunnel configurations were manufactured and tested in the AFIT low-speed wind tunnel. Computational analysis showed consistent results compared to experimental and flight test results for a clean configuration and a configuration in which a BLF was positioned at 82% span. Spalart-Allmaras turbulence model was chosen for its robustness and applicability to external flow. The results of the CFD testing were validated experimentally and visualized with tufts. Additionally, eleven hours of flight testing were conducted at Edwards AFB to validate the CFD model and wind tunnel data. In this testing, influence of the BLFs at high AoA attitudes was shown to be consistent with CFD and experimental data (Williams et al., 2010). The results of the flight test showed that C_{Lmax} was not significantly impacted by the presence of a BLF below 12°, but revealed comparable improvements to C_{Lmax} for AoAs above 13.9°. This finding, that BLFs are mostly effective at higher AoAs, is consistent with wind tunnel data in Demoret (2020).

2.2.2 Active Flow Control

Active flow control (AFC) is primarily concerned with influencing or manipulating a flowfield about an air vehicle without changing its geometry or attitude (Williams et al., 2010). AFC methods have been studied as a possible means of replacing physical control surfaces, augment existing control surfaces, and moreover improve aerodynamic performance of air vehicles. Past research efforts have shown that novel AFC mechanisms have incredible potential for improving stability, efficiency, and responsiveness of air vehicles (Wang et al., 2021). This technology is presently one of the leading research fields within the aerodynamics discipline (Tousi et al., 2021).

There are several classes into which most AFCs can be organized, as discussed in Tousi: 1) moving body actuators, 2) plasma actuators, and 3) fluidic actuators (Tousi et al., 2021). Moving body actuators induce fluid movement without adding or subtracting momentum and for this reason are not relevant for this current discussion. Plasma actuators inject ionized flow into the boundary-layer to achieve flow manipulation in predictable, cyclic manner. Fluidic tank actuators inject flow into the boundary-layer sourced from a reserve (compressor or tank). The latter of these three classes is of primary concern for the scope of this thesis and will be the focus in this section.

Walker (2018) studied the effectiveness of AFC on straight and swept wings. The authors noted that an AFC fence positioned at 70% spanwise location delayed stall onset long than a passive boundary-layer fence at the same location. The swept-wing configurations saw even greater stall delaying capability and C_{Lmax} improvement than the straight wings when using the AFC fences. After testing a 30° swept-wing configuration, Walker (2018) determined a maximum of 12.8% positive change in C_{Lmax} when using AFC at 70% spanwise location.

De Giorgi et al. (2015) compare two leading applications of AFC to discuss aerody-

namic effectiveness and efficiency. The two modes of AFC are synthetic jet actuators (SJA), a type of plasma actuator, and continuous jet actuators (CJA), an example of a fluidic actuator. Both applications function by energizing the boundary layer through the addition or subtraction of high-momentum flow. By injecting or removing momentum, flow profiles, and subsequently global aerodynamic performance, can be augmented.

Synthetic jet actuators operate cyclically generally in the following manner: 1) energy is added to a small cavity containing air in a constant-volume heating process, 2) the high-energy air is ejected from the cavity driven by the pressure difference between the inlet and outlet, passing though a nozzle, and 3) the pressure in the cavity drops below ambient conditions and transiently recovers ambient conditions. Continuous jet actuators operate as their name would suggest: a steady stream of flow, sourced by any means, is actuated on demand and ejected through a nozzle to increase the momentum in a specific region. Different applications of CJAs can operate in reverse order in order to remove momentum Wang et al. (2021).

Figure 7 visualizes the effects of energizing the boundary layer using AFC methods. The two CJA visualizations feature two different momentum coefficients. All cases consider an AoA of 16.6°. The baseline case with no actuator (top left) shows significant flow separation when compared to the SJA (top right) and CJA (bottom left and right). The results showed non-trivial delay of separation and thus increased C_{Lmax} for both AFC cases. It was shown that SJAs were able to achieve the same effectiveness as the CJAs with lower momentum coefficient, thereby showing SJAs to be more efficient between the two Tousi et al. (2021).

Tousi et al. (2021) performed a computational optimization study to determine the most efficient and most effective configuration of an AFC nozzle varying the following five parameters: jet position, jet width, momentum coefficient, forcing fre-

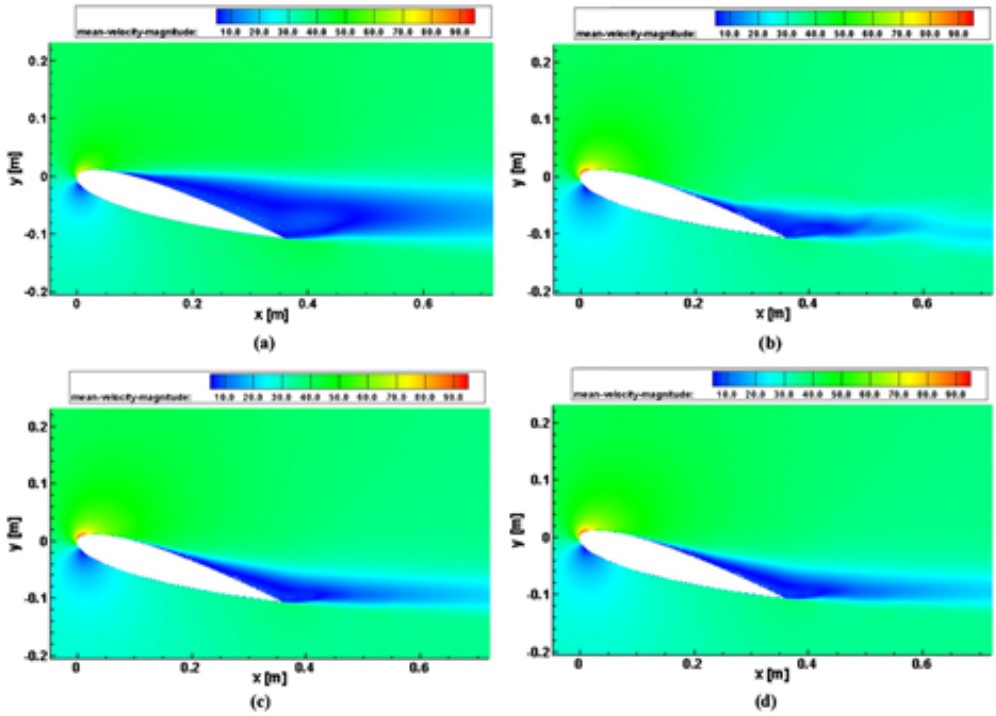

Figure 7. Comparison of two AFC methods. Baseline (top left), SJA (top right), and CJA (bottom left and right), Tousi et al. (2021)

quency, and inclination angle. The airfoil and freestream conditions for all tests were identical, using an airfoil based on the SD7003, which is similar to a NACA 1408. The Reynolds number for all cases was 60,000. Preliminary results showed that the effect of AFCs were more pronounced at higher angles of attack, notably in regions of greater separation. The authors attributed this to the addition of momentum in the boundary-layer and ultimately delaying separation, as shown in Figure 7.

2.3 Reynolds Effects

The Reynolds number is a nondimensional parameter that governs the motion of viscous flows resulting from the Navier-Stokes governing equations. When two flows match in Reynolds numbers, regardless of any other dissimilarities, they are said to be similar to one another. It is described most succinctly as the ratio of a flow's inertial forces to its viscous forces. Thus, flows with high Reynolds numbers

are less influenced by viscous effects while flows with low Reynolds numbers are more influenced by viscous effects. The Reynolds number is presented in Equation (1). The parameter ρ represents the fluid density, the parameter, U is the freestream velocity, the parameter L is a characteristic length, and μ is the fluid viscosity.

$$Re = \rho U L/\mu \tag{1}$$

Fluid entrainment is a viscous flow phenomenon that accounts for mass flow increases along shear layers as fluid elements at the boundary of a shear layer are entrained to conserve momentum and mass flow. This phenomenon is evident in AFC devices in which the flow ejected from an orifice or slot increases momentum as distance from the slot increases. The mass flow rate and subsequent energy of a slot compounds on itself and thereby increases efficacy of the control device. Because the effect is induced by viscous effects at shear layers, lower Reynolds numbers will result in greater flow entrainment.

Polhamus (1996) provides a comprehensive description of the effect Reynolds number has on a number of geometric planforms in order to characterize stall propagation. He first discusses two-dimensional wing-section stall characteristics as a starting point for discussing related, yet different, phenomena in three-dimensional wings. In NASA Technical Report 4745, Polhamus references a method wing-section performance data using lifting-line theory to predict full and finite wing performance outlined in Sivells and Neely (1947). Equation (2) is the direct result of Polhamus' observations. The factor k_p is the lift curve slope at zero AoA and k_v is the induced drag curve slope also at zero AoA. The parameter α represents the angle of attack.

$$C_L = k_p \sin(\alpha)\cos^2(\alpha) + k_v \cos(\alpha)\sin^2(\alpha) \tag{2}$$

The transition from considering two-dimensional wing sections to three-dimensional wing geometry is accompanied by the "onset and spanwise progression of turbulent reseparation near the leading edge" Polhamus (1996). The Reynolds number drives the location of transformation from re-separation flow, near the leading edge, to vortex flow on delta-wing planforms. The leading-edge vortices' (LEV) evolution and breakdown are Reynolds-dependent.

Polhamus considers the attached flow suction force and the normal force produced by the separated vortex flow to be equal, which simplifies the analysis by linearizing the problem. While the methods discussed in Polhamus (1996) use highly simplified and aged methods, they are well-established and provide a basis for understanding the very real physical phenomena responsible for vortex propagation on delta-wing geometry. Nevertheless, modern applications of computational aerodynamics can provide far more accurate data and useful visualizations than these methods do.

Where efficiency is concerned, higher sweep angles result in less similarity between base wing section and three-dimensional lift performance. Figure 8 shows that increasing the sweep results in divergent domains of wing efficiency; higher corrected efficiency is found in wings with higher sweep. For straight wings, the ratio of wing-section lift coefficient to wing lift coefficient (C_l/C_L) follows the 2D lift coefficient with slight inefficiency. At higher sweep angles, there exist regions significant inefficiencies instigated by the "cotangent loading parameter" correction (Polhamus, 1996). This highlights the important physical truth that lift in delta wings is generated by fundamentally different means than in their straight-wing counter parts. The lobes in performance increase and decrease correspond to attitudes in which lift is actually higher in the three-dimensional case than in the 2D case, showing the nontrivial advantage of LEVs at high angles of attack (Polhamus, 1996) The converse of this is true as well - there are regions in which delta wings perform lower than their

straight-winged counterparts.

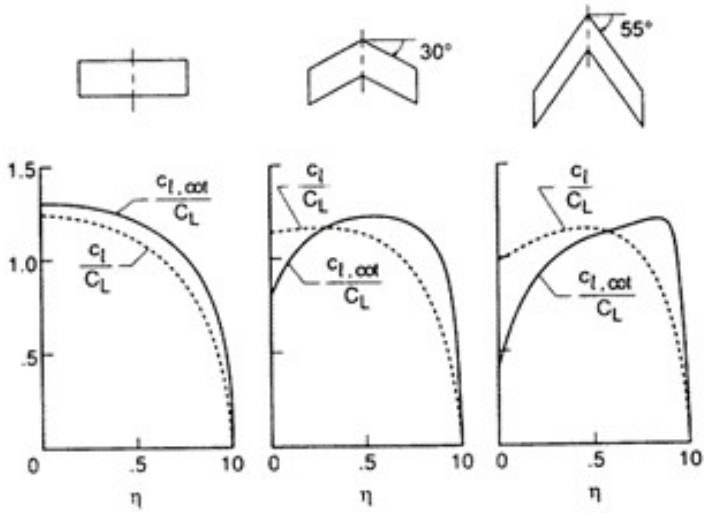

Figure 8. Comparison of wing section and finite wing lift generation varying sweep angle (Polhamus, 1996)

The early work of Brown and Michael (1954) addressed flows that do not have "restrictive amounts of viscous dissipation". The authors present several flow examples: vortex shedding and swept wings with separated flow. The lift curves for bodies in such flow fields are nonlinear because of leading-edge (LE) separation associated with high sweep wing geometries. In their study, the authors use potential flow theory to predict the aerodynamic forces acting on a slender delta-wing.

One important observation in Brown and Michael (1954) is shown in Figure 9 that the spanwise wing loading profile shows clear inboard motion for delta-wing geometries for increases in AoA. Where low AoAs still allow for attached flow, the wing loading shows relatively consistent loading across the span. At near-stall AoAs, the peak loading occus farther inboard and does not follow the consistent distribution. The spike appears where the primary vortex core physically resides.

Burtsev et al. (2021) studied the effects of aspect ratio on flow stability in the wake of swept, finite wings. The authors discovered that the most unstable mode

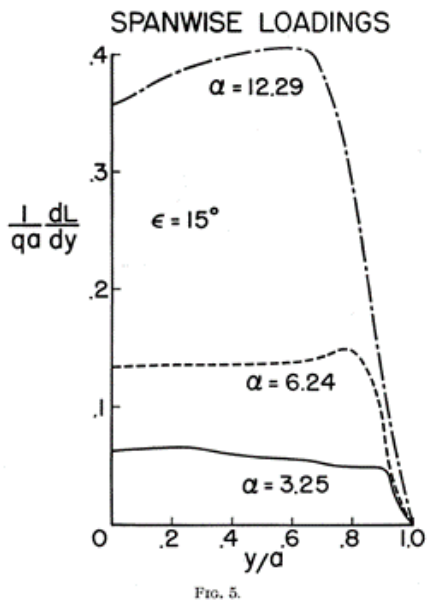

FIG. 5.

Figure 9. Comparison of wing section and finite wing lift generation varying sweep angle (Brown and Michael, 1954)

peaked in the mid span region in the wake and tended to move outboard for configurations with higher sweep. The dominant instability mode for unswept wings was Kelvin-Helmholtz type, similar to the instabilities found in two-dimensional wing-section analysis. For swept wings, which includes delta wings, there is an interaction mode which complicates stability analysis. The authors discuss how the interaction mode instabilities in high aspect ratio, swept wings "evolve into elongated streamwise vortices" Burtsev et al. (2021). For low aspect ratio, swept wings, these instabilities "become indistinguishable from tip-vortex instability" Burtsev et al. (2021).

Burtsev et al. are primarily concerned with characterizing causes of separation in finite wings, both swept and unswept. During their analysis, Burtsev et al. make special note of limited understanding of the instabilities that lead to three-dimensional separation on a wing surface. Their takeaway was that what physically causes the unsteadiness of two-dimensional vortices is the result of a "stationary three-dimensional global mode" Burtsev et al. (2021). An important parameter for this discussion is the Strouhal number. It is defined in Equation (3) Burtsev et al. (2021). The factors

f and c represent the frequency in question and propagation speed, respectively. The factors U_∞ and α represent the freestream velocity and angle of attack, respectively.

$$St = fc \sin \alpha / U_\infty \tag{3}$$

Low Strouhal numbers are indicative of low frequency vortex shedding and breakdown relative to the freestream velocity. Figure 10 shows how the interaction mode is primarily only of concern for low Strouhal numbers and high sweep angles.

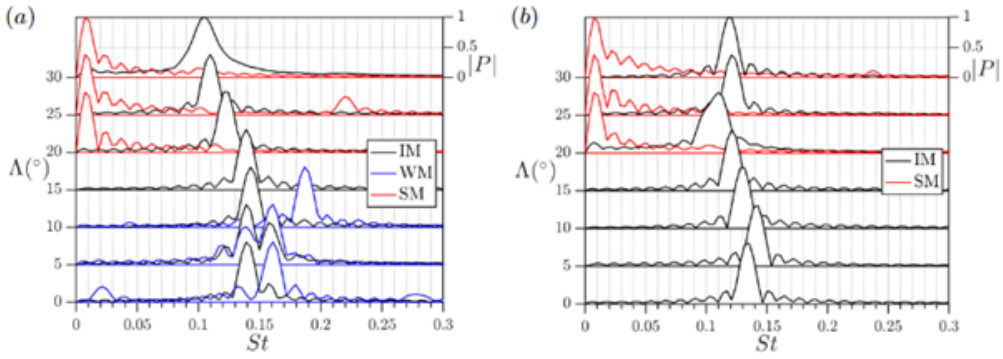

Figure 10. Instability modes as functions of Strouhal numbers and wing sweep

2.4 Vortex Generation and Decay

Circulation is a global fluid quantity describing the net turning of the flow over a body. It is the sum of the local changes due to an imbalance of rotational forces. Vorticity is then a quantity describing the local rotation of a fluid element. Increases in vorticity within the flow field can result in increases in the total circulation, which is proportional to the global lift of an aerodynamic body. Therefore, vorticity plays a significant role in shaping the lift mechanisms in aerodynamic bodies.

The vorticity transport equation for incompressible, Newtonian flows is listed in Equation (4). The substantial derivative of the vorticity describes the motion of vorticity in space and time as a function of the velocities, pressure, density, and body

forces within a flow field. Term (*i*) describes the tilting and stretching of vortex filaments. The term (*ii*) describes the creation of vorticity due to misaligned pressure and density gradient. Term (*iii*) represents the torque due to non-conservative body forces. Term (*iv*) describes the diffusion of vorticity associated with viscous torque.

$$\frac{D\omega}{Dt} = \underbrace{(\omega \cdot \nabla)\mathbf{u}}_{\text{i}} + \underbrace{\frac{\nabla\rho \times \nabla p}{\rho^2}}_{\text{ii}} + \underbrace{\nabla \times \mathbf{x}}_{\text{iii}} + \underbrace{\nabla \times \mathbf{F}_{\mathbf{viscous}}}_{\text{iv}} \tag{4}$$

Analagous to the mass flow continuity equations, vortex tubes decrease in area and increase in rotational velocity as they stretch. Stretching and tilting occur when in specific velocity gradients; that is, when a flow is accelerating, vortex tubes subject to the flow field will be impacted much like how quiescent flow is entrained by a fluid jet's shear layer. Stretching occurs when a vortex tube is exposed to a streamwise-accelerating velocity gradient, and tilting occurs when the vortex is exposed to a cross-flow velocity gradient.

Marzanek (2019) shows strong correlation between a vortex's tilting and the increase of circulation, which is accounted for in term *(i)*. Particular emphasis on the effects of this term are important for comparing vortices over various delta wings. The life cycle of a LEV on a delta wing correlates to the performance of the wing. The generation of the vortex corresponds to a change in the mechanism for generating lift. The vortex strengthens at higher angles of attack which in turn causes the lift to increase. Similarly, the onset of its separation precedes the wing's stall. It is therefore critical to properly characterize these phenomena, and understand their causes, when studying delta-wing aerodynamic performance.

Hitzel et al. (2016) investigated methods of predicting the onset of flow separation in response to a NATO task group seeking studies on the topic. The authors employed experimental and computational methods to answer this problem. Comparing wind

tunnel data visualized with particle image velocimetry (PIV) and computational fluid dynamics (CFD) methods, the experimenters were able to validate their models and characterize vortex generation on a delta wing. The focus of the study was a delta wing with 53° sweep, rounded-edge delta wing with 30° trailing-edge (TE) sweep.

Figure 11 shows streamwise flow turning in the outboard spanwise direction as a result of the staggered pressure peaks along the wing sweep. Subsequent generation of a primary vortex driven by pressure gradient at the leading edge. The assembly of secondary and tertiary vortices are visualized as well. The breakdown of the vortex is shown to begin in the center of the chord aft of the location of its generation. As discussed in section 2.1, the vortex formation on the leading edge is a function of the wing sweep angle, the angle of attack, and to a lesser extent, the Reynolds number and Mach number.

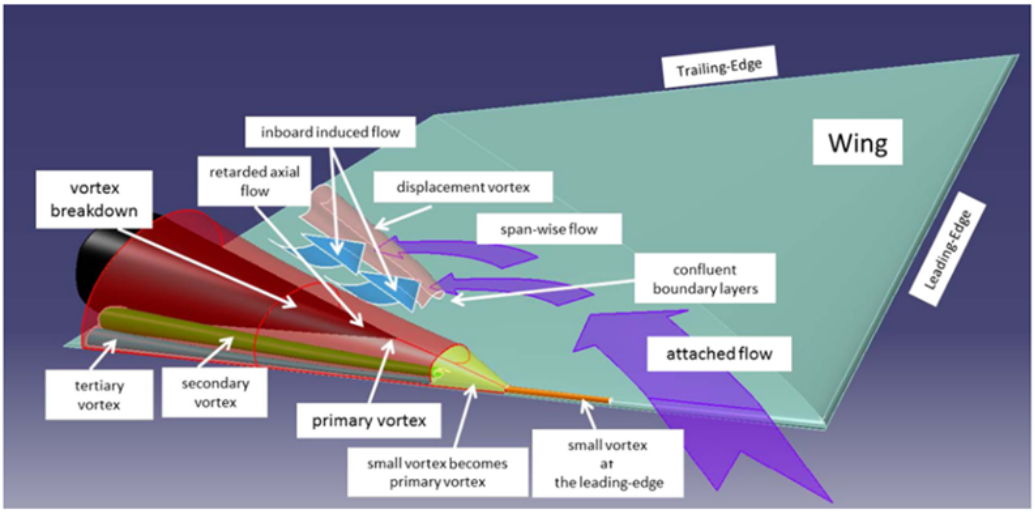

Figure 11. Propagation and decay of a leading-edge vortex (Hitzel et al., 2016)

Wentz and Kohlman (1968) describes shortcomings in capturing the breakdown of the vortices in theoretical vortex-driven lift models. While Polhamus (1996) is able to estimate lift gain from the low pressure vortices, characterizing their bursting and breakdown is difficult to predict. It is their breakdown that causes a sharp decline

in wing performance for higher AoAs. The authors in Wentz et al. conclude that vortex decay is primarily affected by LE sweep and subsequent pressure gradient. They describe this breakdown as a sudden increase in the physical size of the vortex core which causes diffusion of its energy (Wentz and Kohlman, 1968).

The location of breakdown (both spanwise and chordwise locations) is of primary concern when characterizing vortex decay. Measurements are generally discussed in percent of the chord to describe locations forward and aft, and in percent of the wing span to describe locations left and right. The relevant and highly succinct results of this study are shown in Figure 12. The relative location of vortex bursting is mapped to AoA and LE sweep. The most relevant takeaway for the scope of this thesis is the apparent positive correlation between LE sweep and breakdown position. For an increase in sweep, experimenters should expect a proportional increase in chordwise breakdown location.

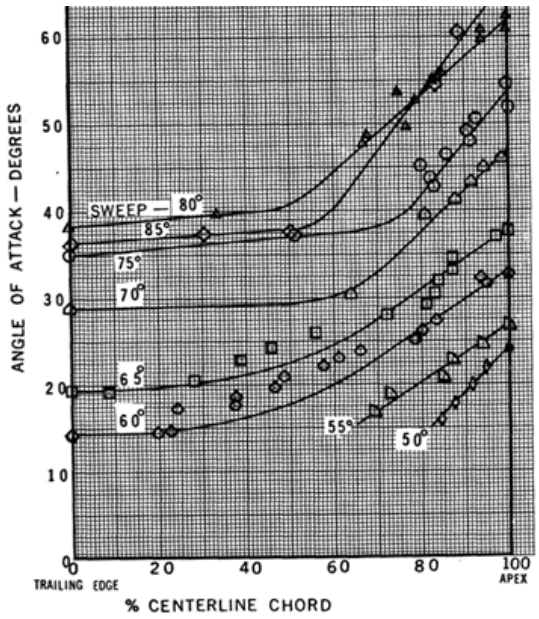

Figure 12. Breakdown location as function of leading-edge sweep and angle of attack (Wentz and Kohlman, 1968)

Marzanek (2019) discusses separated flows over non-slender delta wings such as

the case is in the present study. Nonslender describes delta wings whose leading-edge sweep is less than 55°. He suggests that favorable pressure gradients facilitate reattachment of separated flow leading to enhanced lift performance associate with these types of delta wings. He argues that the primary vortex is perpetuated and remains coherent because of vortex tilting. The tilting of the LEV is shown to stabilize the structure at higher angles of attack.

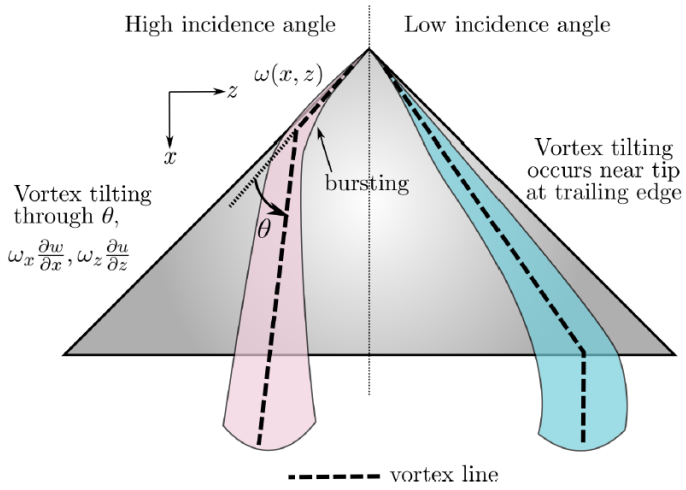

Figure 13. Delta wing vortex tilting (Marzanek, 2019)

The effect of slenderness of a delta wing is studied in Ol and Gharib (2003). They compares two delta wing geometries: a slender wing having leading-edge sweep of 65° and a nonslender wing whose LE sweep was 50°. They evaluated these two wings at various angles of attack and compared the normalized circulation. The slender delta wing was found to exhibit far higher peak circulation, which is proportional to the to the global lift generated by the wing.

Luckring (2004) examines how LE bluntness effects the propagation of the LEVs in slender delta wings. While the scope of the present study focuses on non-slender wings, there is value in noting some of his findings in predicting and understanding the locations and movement of LEVs. He finds the between sharp and blunt LE delta wings concerns the location of the LEV origin. For sharp LEs, the vortex is anchored

at the wing's apex. In delta wings with blunt LEs, the LEV origin is displaced aft of the apex and its location is said to be a function of the angle of attack, Reynolds number, and ultimately the radius of the LE, among others.

Fink (2015) examined incipient separation on a 53° swept diamond delta wing configuration. The author showed that peak *tke* aligns with the center of the vortex core. With this in mind, the *tke* can be used to track the location of vortices in a flowfield. Figure 14 shows two important takeaways from Fink's paper. Subfigure (a) shows the core of the LEV forming on the leading edge and pressed against the surface of the delta wing as it propagates downstream. Subfigure (b) shows the dissipation of *tke* as a function of streamwise distance from the point of formation. This suggests that while *tke* is a valid way of identifying the vortex core and tracking its movement. The *tke* gradually increases approaching the point of LEV separation and subsequently decreases linearly aft of that point. This is an important finding to say the vortex strength itself decreases downstream of the separation point.

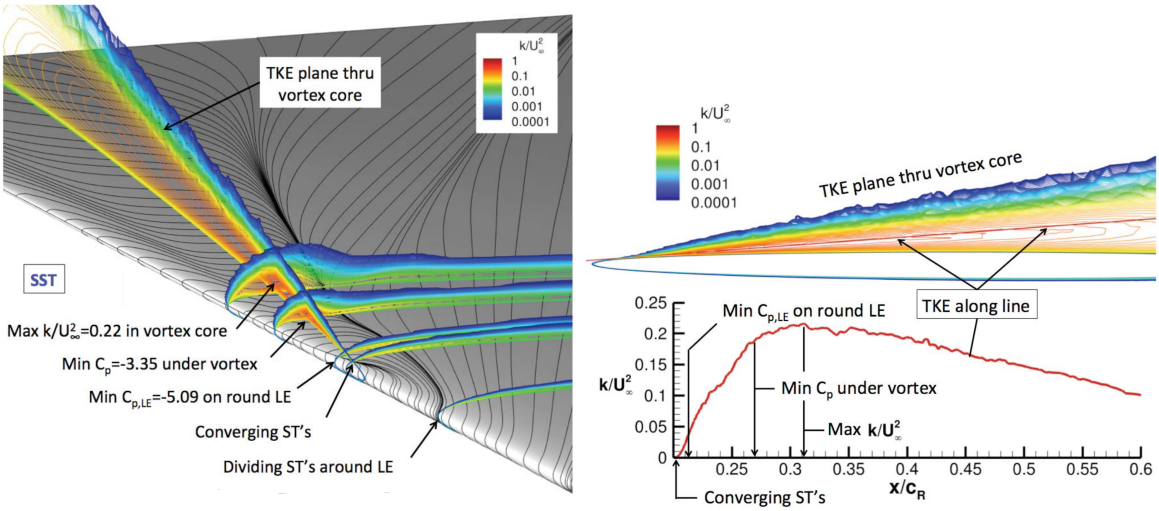

(a) TKE field contours at key stations, 12° **(b) TKE profile along vortex core**

Figure 14. Demonstration of *tke* presence in vortex core (Fink, 2015)

Wentz and Kohlman (1968) also investigated the effects of surface roughness on vortex breakdown. The authors tested one delta-wing configuration with two different

grit sandpapers affixed to the upper surface. Surface roughness was shown to have little impact on the initial breakdown phenomena, but did play a role in stabilizing the position of the breakdown. The stabilizing effect was equally matched by both grades of sandpaper, although the authors reported that despite the unchanging position of breakdown for the various sandpapers, Schlieren imagery showed non-trivial flow-pattern discrepancies. The smooth configuration showed laminar waves in the flow preceding breakdown while the rough configurations showed completely turbulent wake Wentz and Kohlman (1968). Much like straight wing flow, the presence of surface roughness served as an effective boundary-layer trip.

III. Methodology

3.1 Chapter Overview

Cropped delta-wing configurations were tested in the Air Force Institute of Technology (AFIT) Low-Speed Wind Tunnel (LSWT), where special emphasis is placed on studying wake structures. Several different data collection methods were employed in this study to compare quantitative results found in Demoret (2020) and Tedder (2021). Triplewire anemometry was used to characterize flow properties in two-dimensional planes intersecting the wing surface, both spanwise and chordwise. These data surfaces allow for direct comparison to the swept-wing study conducted by Walker (2018), and also to capture qualitative phenomena inferred in Demoret (2020). Additionally, smoke visualization and Schlieren imagery were employed to capture more qualitative phenomena and characterize the flow field of active flow control slots in the AFC configuration. Strain-gauge force balance data was also collected to validate wind tunnel and computational data previously collected.

3.2 Facility

The AFIT LSWT was used for this experiment. Low-speed designation implies its limitation to the incompressible flow regime. It is an open-circuit wind tunnel, meaning that it operates by ingesting quiescent, ambient air and accelerates it up to the test section. The air is subsequently ejected out of a diffuser. The wind tunnel was was constructed by Aerolab. The fan is driven by an electric motor and can operate continuously up to 67 m/s (Mach 0.2). It features a rectangular test section measured at 1.04 meters wide and 0.84 meters high. It extends 1.8 meters in the streamwise direction. The wind tunnel inlet uses a honeycomb mesh flow straightener to minimize freestream turbulence and instabilities created by the inlet. Figure 15

shows a notional open-circuit wind tunnel diagram and all of its basic components.

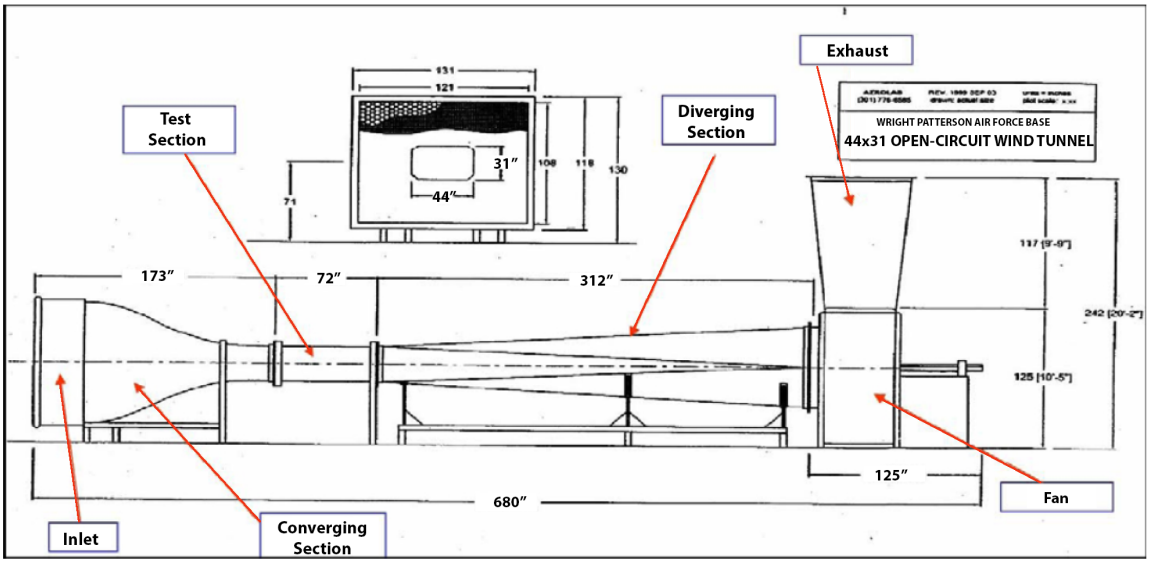

Figure 15. AFIT Low-Speed wind tunnel diagram

3.3 Model Fabrication and Implementation

Three model configurations were used in this study: a) baseline (clean), b) passive boundary-layer fenced, and c) AFC configuration. All of these are shown in Figure 16.

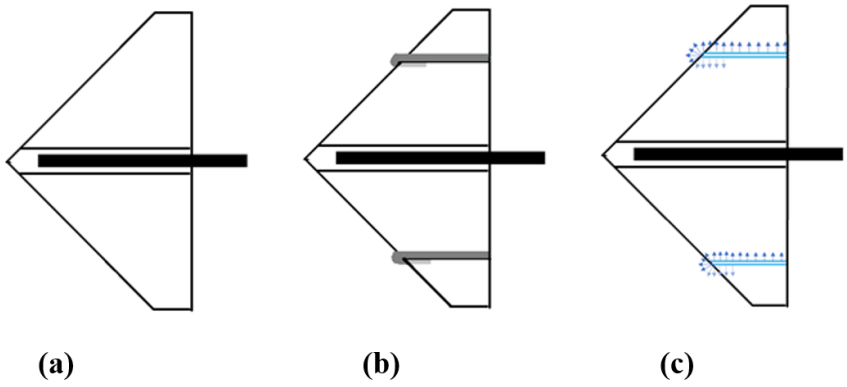

Figure 16. Comparison of configurations in present study

The basic geometry was designed around a NACA 0012 wing section and extruded

to form a 45 degree cropped delta wing with a rounded leading edge. The sting mount forms a sloped protrusion at the underside midsection of the wing with plumbing access for the AFC slots. The models were printed via stereolithography in three separate parts: the left and right wings, and the midsection. Figure 17 shows these three distinct parts.

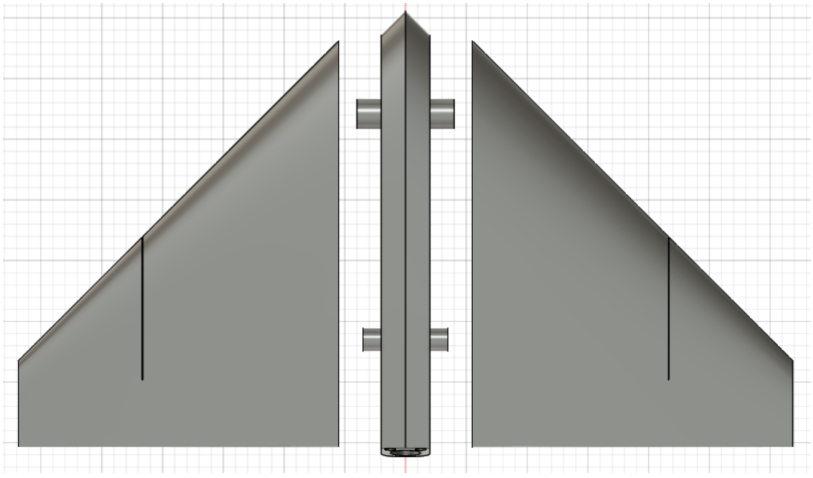

Figure 17. AFC slot configuration used as example of CAD wing geometry

Stereolithography (SLA) is an additive manufacturing method in which gel resin is cured with a laser in incremental layers. A motorized table is flooded with the resin mixture and a laser traces each layer as the table it rests on moves downward. The result of the process is a solid body model following the shape of the laser pattern. The uncured material can be reused for subsequent prints. The primary advantages of SLA are the strength of cured material and relatively low waste for each print.

All three models have hollowed cavities in the wings to form pressurized cavities. Only the AFC model uses these chambers in which there is a streamwise slot at 70% span extending from the front quarter chord length on the bottom to the back three quarters on the upper surface. Figure 18 shows these cavities, the plumbing, and the support columns used to maintain structural integrity while under load. The cavities and plumbing passages are highlighted in blue, the support columns are in white, and

the sting mount is highlighted in orange.

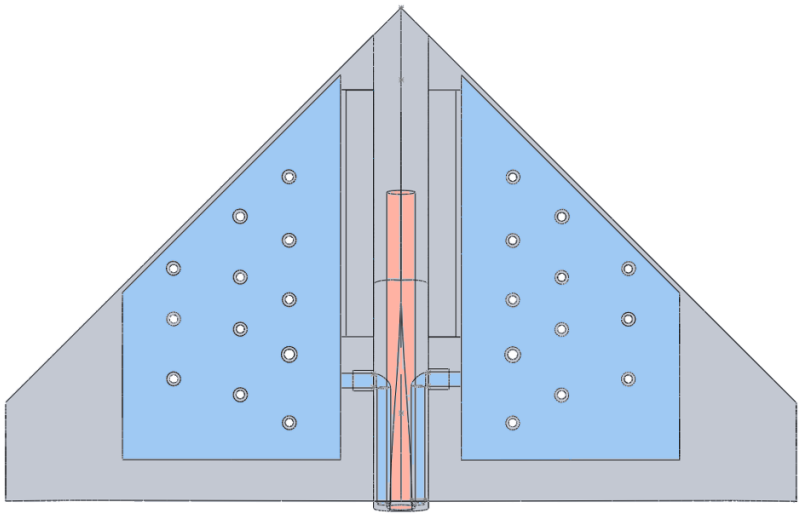

Figure 18. Wire diagram showing pressure cavities

3.4 Instrumentation and Data Acquisition

3.4.1 Measuring Forces and Moments

The AFIT six degree-of-freedom (DoF) force balance was used in all wind tunnel testing for this experiment. The six components of the force balance include three orthogonal forces (normal, side, and axial) and three moments (pitch, roll, yaw). The force balance measures stress by means of a series of strain gauges positioned throughout the device. Its normal directions are limited to 50 lbs and its axial direction is limited to 10 lbs. It was used to reproduce some data collected in Demoret's study for validation is used to provide a quantitative baseline for interpreting the wake structures, the primary concern for this study. For this same reason, only two of the degrees of freedom, namely normal and axial force, were used. The present study addresses lift and drag exclusively, so moments and side force are not addressed.

Lift and drag forces are derived from the normal and axial forces captured by the force balance as a function of the model's angle of attack, α. Eqs. (5) and (6) show

these geometric transforms applied to derive the lift (L) and drag (D) forces. Figure 19 shows those same transformations visually. The factors N and A represent the normal force and axial force, respectively.

$$D = N \sin \alpha - A \cos \alpha \tag{5}$$

$$L = N \cos \alpha - A \sin \alpha \tag{6}$$

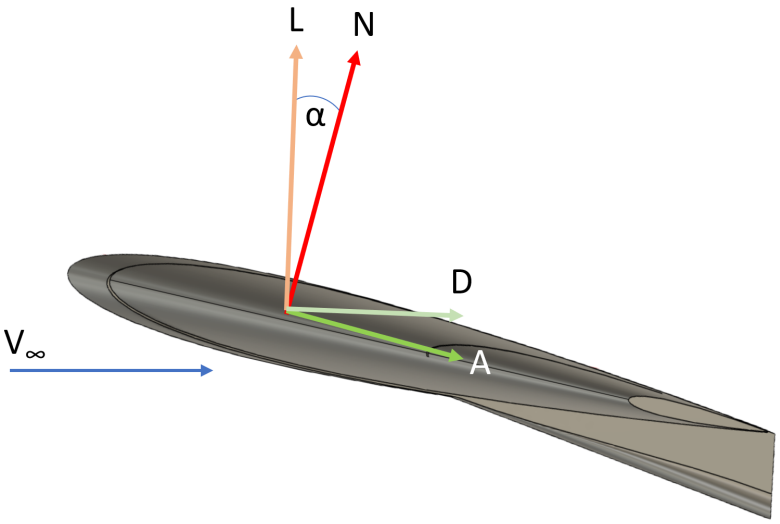

Figure 19. Force transformations, lift and drag

Both of these forces can be non-dimensionalized to find the force coefficients, which are more helpful in relaying subscale wind tunnel data. Eqs. (7) and (8) show these non-dimensionalized force coefficients. The dynamic pressure, q, is defined as the difference between the measured total pressure and static pressure in the test section. The parameter S is a the wing's planform area.

$$C_L = \frac{L}{qS} \tag{7}$$

$$C_D = \frac{D}{qS} \tag{8}$$

The pitching moment coefficient (C_M) is likewise found in Equation (9) by non-dimensionalizing the pitching moment (M) along a characteristic length. The mean chord length, $\bar{c} = 10$", was used.

$$C_M = \frac{M}{qS\bar{c}} \tag{9}$$

Flow straightness in the test section was verified by comparing force data of the baseline delta-wing configuration up-side down and right-side up. The curve formed by the angle of attack versus the normal force would show any variations of the flow direction between the two configurations, ultimately revealing asymmetry in the test section (Barlow et al., 2015). Figure 20 shows the results of that experiment in the AFIT LSWT. The flow was determined to be offset by far less than 1°, and thus the assumption of straight flow holds for this study.

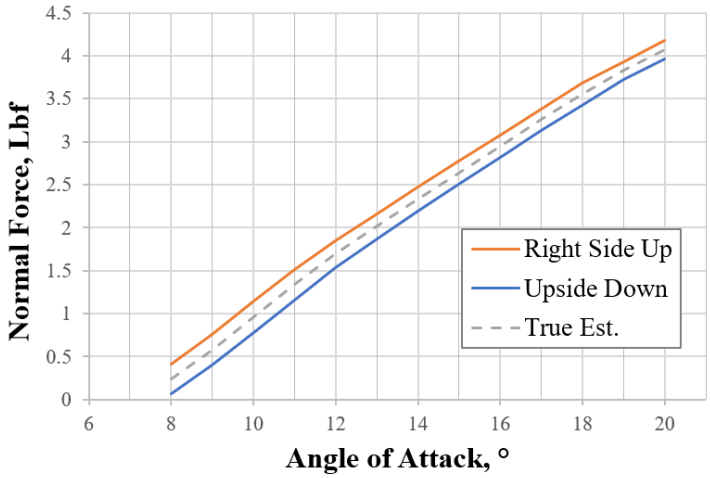

Figure 20. Flow Angularity Test

3.4.2 Measuring Flow Properties

Atmospheric data were collected to determine tunnel speed conditions and for use in final data reduction. The total pressure was determined by a pressure transducers

placed outside the wind tunnel. The static pressure was determined with a pressure transducer at a forward location in the test section. Test section velocity was readily found with this data.

In Gamble and Reeder (2009), the authors were able to characterize the wake of a propeller by traversing a hot wire throughout various regions of interest aft of their model. Similar to how Gamble and Reeder traversed a hotwire through the wake of the propeller, the present study swept a hot wire in the wake of the aforementioned delta wing configurations to capture pertinent wake data.

A Dantec 55P95 three-component, constant temperature anemometry (CTA) hot wire probe was used to capture velocity data at specific locations in the flowfield. The probe features a unique tri-axis wire configuration that allows its control software to resolve orthogonal, laboratory-frame velocity components by a series of coordinate transformations. Figure 21 is a graphic from Dantec with dimensions in millimeters. Thin copper filaments are affixed to the ends of each prong and connect to the computer controller. Dantec advertises that its mutually-orthogonal wires allow for velocity "acceptance cone" of 70.4°. The sensor wires are made from platinum-plated tungsten, have a diameter of 5 μm, and have an effective sensor length between the poles of 1.25 mm. This model is able to measure flows between 0.5 and 200 m/s at frequencies ranging from 1 to 400 kHz. The orthogonal wires are offset by

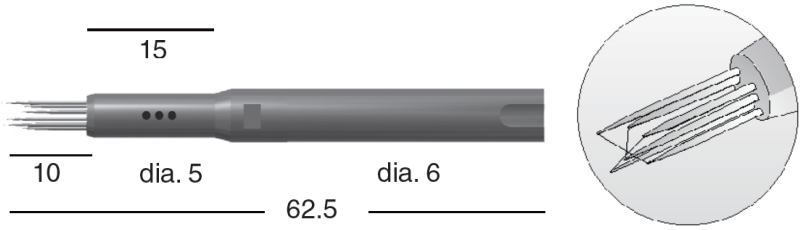

(a) Triple Wire Device **(b) Triple Wire Prongs**

Figure 21. Dantec hot wire probe

The computer controller records the voltage required to maintain constant tem-

perature on all of the hot wire filaments and are later correlated to velocity using a calibration file. While the probe is subjected to fluid motion in the wind tunnel, the airflow transfers heat by convection around the probe. The logged voltage data is directly related to the velocity experienced by the probe by heat transfer relationships. A fourth-order polynomial calibration is used and is sufficient to relate the voltage to velocity.

Specialized wind tunnel ceilings were fabricated at the AFIT model shop to allow hot wire probes to navigate inside the test section. The primary ceiling used in this study is shown notionally in Figure 22. The slots were 0.5 inches wide by 12 inches long, separated by one-inch increments. It is from this design that the data plane numbering is defined. Data plane #1 is formed using the farthest forward slot and each subsequent slot increments by one.

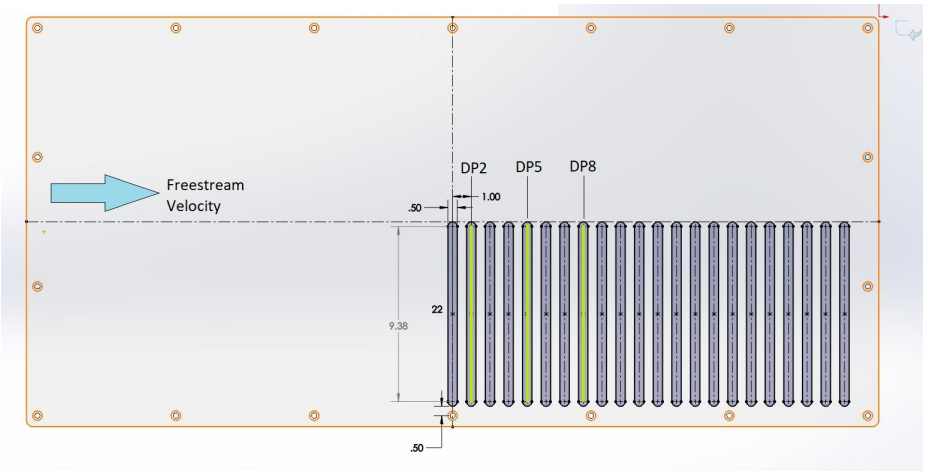

Figure 22. Wind tunnel ceiling design with slots for traverse probe

These slots permitted the traverse probe to collect CTA velocity data along data planes similar to what is shown in Figure 23. Time averaged flow velocity data were captured along the traverse path forming Y-Z planes at various positions in the X-direction. The mean and root mean square velocities were recorded for all three components.

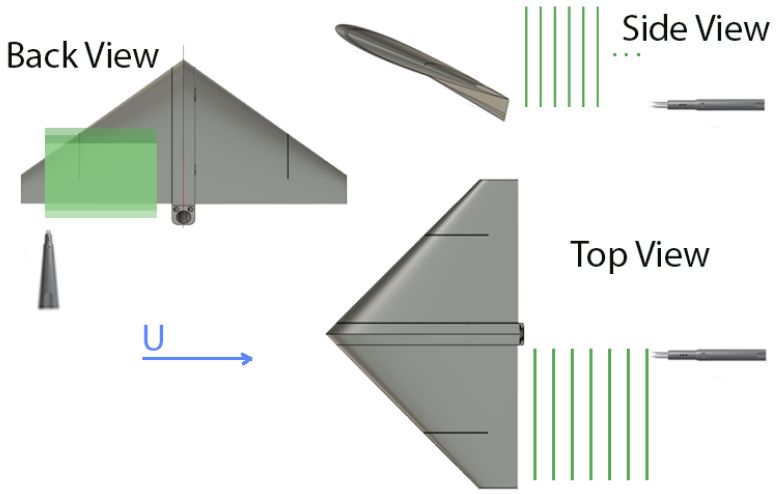

Figure 23. Three-view diagram of data planes aft of wing model

A Dantec three-axis traverse system affixed to the top of the wind tunnel allowed for precise movement of the probe in the wind tunnel test section. For the initial study of the separation region, the data plane was wide enough to encompass the region of the LEV only, and not the wing tip vortex.

3.5 Test Methodology

3.5.1 Identifying Locations of Vortices

Data collection via hot wire traversing is time consuming, so in order to optimize and focus on particular regions of interest, tufts were used to identify the regions of interest quickly. A wire mesh was positioned aft of the sting mount to examine the wake and helped determine the approximate locations of both leading edge and wingtip vortices. Chickenwire having dimensions 18" (width) by 23" (height) and grid spacing of a half-inch was used. Strands of 1.5" long florescent thread affixed to the mesh every inch formed the tuft grid. Figure 24 shows the mesh grid at a low

angle of attack.

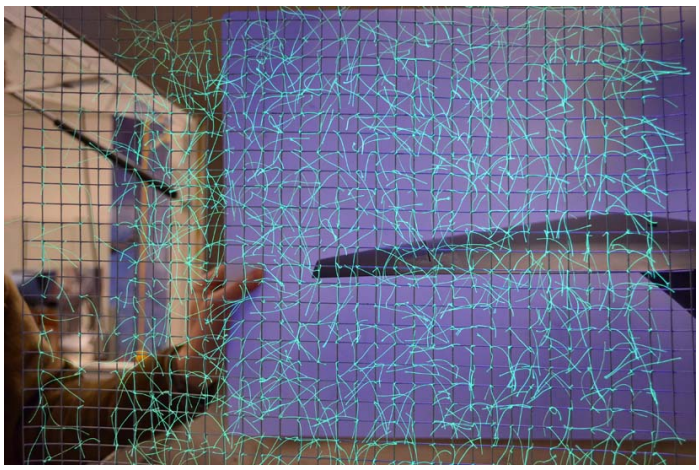

Figure 24. Tuft mesh

Figure 25 shows the position of the wing in the camera's field of view to show relatively where the mesh is for perspective when interpreting the vortex locations. The center of pitch rotation is approximately collocated with the half-chord location, so as the AoA increases, the trailing edge drops.

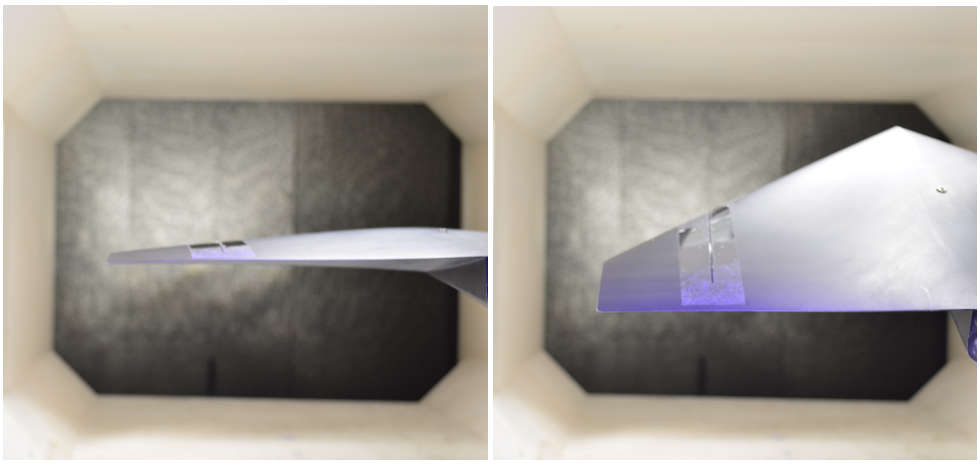

(a) AoA = 3° **(b) AoA = 28°**

Figure 25. Camera perspective for referencing tuft locations at AoA extrema, AFC configuration

3.5.2 Hot Wire Test Methods

Once the approximate locations of the vortices were determined using the tuft images, a refined hot wire traverse mesh was executed. The special wind tunnel ceiling used to traverse the probe in data planes did not extend far enough to encompass the half-span of the wing, so the triple wire probe was rotated 45° and value transformations were applied in post-processing.

Streamwise distance in the wake is measured in percent chord (% x/c). Table 1 shows generalizes the plane locations by relating their relative distances to discrete data plane (DP) numbers.

Table 1. Vortex Location Experiment Test Points

Data Plane #	Location, x/c
DP 1	70%
DP 2	90%
DP 3	110%
DP 4	130%

The dimensions of the first set of standardized data planes used in this experiment are shown in Figure 26. The three primary data planes numbered by their corresponding channel in the wind tunnel ceiling tile. Data plane (DP) 1 corresponds to a Y-Z plane whose X-position is roughly four and one-half inches forward of the trailing edge (TE). The DP 2 was positioned three inches aft of DP 1 and DP 3 was three inches aft of DP 2. They were located roughly at the the TE and three inches aft of the TE, respectively.

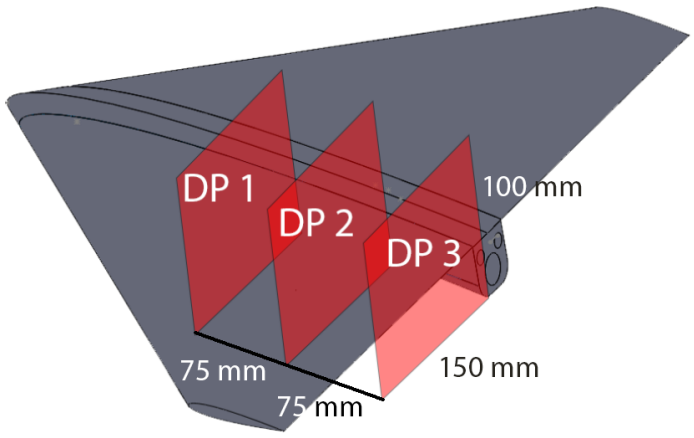

Figure 26. Data plane dimensions and locations

The data planes used to capture the locations of the LEV and wing tip vortices varied in size and position compared to the prior separation region data planes. Their dimensions are shown in Figure 27. The plane was elongated in the chordwise direction to be able to view both the wing tip as well as LEV structures. The entire plane was shifted down in order to center around the vortex cores. Post-processing and determination of quantities in the reigons of interest depend on a full picture of the vortices.

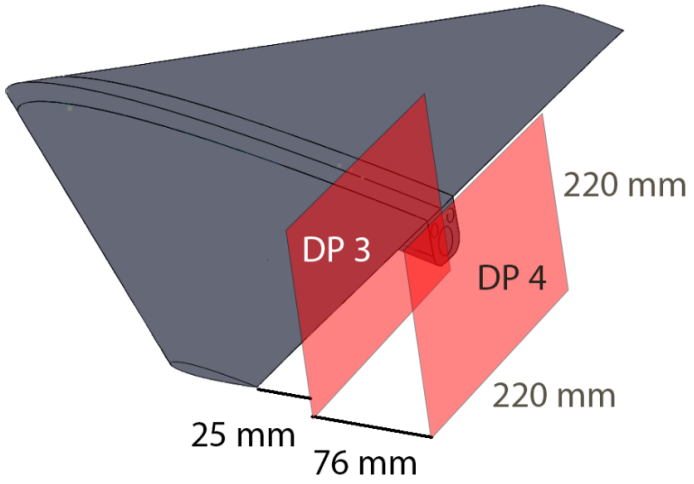

Figure 27. Data plane dimensions and locations for vortex ID

Each DP used to characterize the separation regions were 150 mm wide by 100 mm high. There were 30 data points collected at each grid point such that the y-direction step size was 5.17 mm and the z-direction step-size was 3.45 mm. The bottom of DP 3, which is fully clear of the trailing edge, was vertically positioned roughly at the rotation axis of the sting mount. At lower angles of attack (AoA), this positioned the data plane closer to the trailing edge, while at higher AoAs it was higher than the trailing edge. The two data planes in which the probe was over the body, it was required to offset the plane's starting point to avoid collision with the probe. The DP 2 was offset by 10 mm and the DP 1 was offset by 40 mm. These vertical offsets were accounted for in the reduction and plots by holding axis limits constant.

The reduced data was plotted in Matlab and non-dimensionalized to display both y- and z-coordinates in terms of percentage of the half-span. The origin is aligned with the center of the wing body and the bottom of the refernce plane at approximately the pitch fulcrum. Furthermore, the velocity data is all presented in percent change from freestream conditions, thus a value near the freestream condition will be displayed as zero and changes, negative and positive, will denote percent changes. Figure 28 shows the non-dimensional coordinates and the reference length used to define the scale. By non-dimensionalizing the frame, all the visualized data is readily compared to show trends. Because the scope of this study includes characterizing wake geometry and vortex development, non-dimensional values serve to communicate effect for low-speed flows of interest.

The probe mount had to be angled outward to be able to traverse past the wing tip for the vortex data plane runs, so an coordinate transform about the Z-axis was necessary to reduce the data in laboratory reference frame. Walker (2007) demonstrated this transformation using a similar hot wire set up. The transformations are listed in Equations (10), (11), and (12).

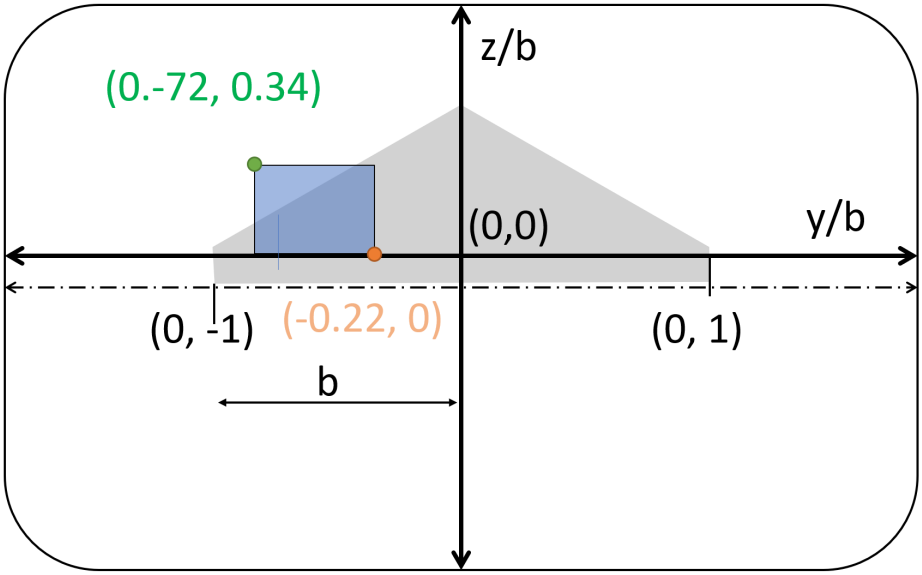

Figure 28. Non-dimensional test section reference

$$u_t = u_0 \cos\theta - v_0 \sin\theta \tag{10}$$

$$v_t = u_0 \sin\theta - v_0 \cos\theta \tag{11}$$

$$w_t = w_0 \tag{12}$$

Figure 29 shows these transformations visually. The transformed streamwise velocity component, u_t, is aligned with the laboratory X-axis and the transformed spanwise component, v_t, is aligned with the Y-axis. The transformation is made by rotating the frame about the Z-axis. An angle of 45° was used for this experiment.

The reduced hot wire data was subsequently non-dimensionalized with the freestream velocity in both applications. The result yielded plots showing percent change from freestream condition, which is zero. Any variation from that would show up on contour plots as positive or negative percentages of the freestream. Equation (13) shows the the expression as it applies to the u-velocity.

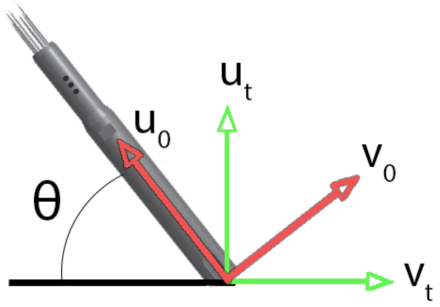

Figure 29. Laboratory frame transformation about the Z-axis

$$u = \frac{u - U_\infty}{U_\infty} \tag{13}$$

For the v-velocity, the values are non-dimensionalized also with reference to the mean freestream velocity. This results in spanwise flow being listed as a percentage of the freestream u-velocity. This is shown in Equation (14).

$$u = \frac{v}{U_\infty} \tag{14}$$

Turbulence information was determined using the root-mean-square (rms) data collected by the hot wire in all three components. Two turbulence parameters of interest were computed: turbulence intensity, Tu, and turbulent kinetic energy. The turbulence intensity was derived by dividing the velocity components' rms values by the freestream velocity, as shown in Equation (15). These values were plotted in certain cases to highlight regions of higher turbulence. This data will be especially valuable for tailoring CFD setups in future studies. The u_{rms} term is the streamwise rms velocity term collected by the hot wire.

$$Tu = \frac{u_{rms,i}}{U_\infty} \tag{15}$$

The turbulent kinetic energy, *tke*, was computed using Equation (16). The terms

u_{rms}, v_{rms}, and w_{rms} are the three rms components of velocity in the laboratory reference frame.

$$tke = \frac{u_{rms}^2 + v_{rms}^2 + w_{rms}^2}{2U_\infty^2} \tag{16}$$

In order to better identify the LEV and wing tip vortices cores and find the shear layers, the local turbulent kinetic energy values were normalized by the maximum turbulent kinetic energy.

3.5.3 Computing Relative Vortex Strength

Equation (17) is the general definition of the circulation in a velocity field. In order to fully capture the circulation of the vortex, velocity data from the entire effected vortex is required. The limited plane view of the field obtained in the wind tunnel did not capture the LEV completely. By applying two simplifying assumptions, the vortex circulation was estimated. The first assumption was that the plane view captured exactly half of the LEV. The second assumption was that the vortex was symmetric about that half.

$$\Gamma(r) = \int_0^{2\pi} rV(r,\theta)d\theta \tag{17}$$

For appropriate scale comparisons of the vortices, the circulation values obtained were normalized by the magnitude of the lowest circulation case. That assumption will be made for the data reduction and calculations to simplify computations. The circulation from the data presented will be multiplied two-fold to account for the bottom half that is out of view. Equation (18) shows this assumption applied: the integral extends around only one-half of the vortex and is scaled by two to account for the other half not visible.

$$\Gamma(r) = \int_0^{\pi} 2rV(r,\theta)d\theta \tag{18}$$

Because the hot wire yields discrete data points and not a continuous velocity field, it is necessary to discritize the circulation by summing the velocity values weighted by the cell size. The traverse steps, Δy and Δz, were used to compute the areas. The circulation is then found by summing up the product of the velocity in each cell by the corresponding area in the region defining the vortex core. The vortex region is discriminated by accounting for cells having turbulent kinetic energy values greater than 70% of the freestream. circle containing the vortex and the velocity within the LEV across the half arc shown in the data. This data is multiplied by a factor of two to account for the LEV's lower half.

$$\Gamma(A) = 2\sum_{i=1}^{n} V_i \Delta y \Delta z \tag{19}$$

Equation (20) shows the definition of vorticity, which is the curl of velocity. For the vorticity calculations, discrete values in the velocity field were numerically processed to estimate the curl by means of finite differencing. The streamwise component of the vorticity is shown in Equation (21).

$$\overrightarrow{\omega} = \nabla \times V \tag{20}$$

$$\omega_x = \frac{V_{y+1,z} - V_{y,z}}{\Delta z} - \frac{V_{y,z+1} - V_{y,z}}{\Delta y} \tag{21}$$

3.5.4 Reynolds Stress

The Reynolds stresses, $u_i v_j$, are the components of a symmetric, second-order tensor where the main diagonal is comprised of the normal stresses and the off-

diagonal components are shear stresses (Pope, 2000). The values were subsequently by the freestream velocity squared for scale comparisons, $u_i'v_j'/U_\infty^2$. The Reynolds stresses can be used to fine tune turbulence modeling in computational applications, so were collected in this study to provide a basis for future CFD studies.

In addition to providing verification and validation to CFD codes, the Reynolds stresses can help identify regions of anisotropy and provide one more method of identifying shear layers in the vortices. The Reynolds stress term represents the averaging of slower masses of fluid moving into higher momentum flow, and conversely faster moving masses of fluid moving into lower momentum flow. The three directions of Reynolds stress, *u'v'*, *v'w'*, and *u'w'* encompass the three possible ways a fluid element can be interjected into a flowfield of disparate momentum. Because of this, the Reynolds stresses aid in identifying regions of higher momentum transfer due to turbulent stresses, which are oftentimes shear layers or pockets of rotation.

3.5.5 Computational Aerodynamics

Maj Shawn Naigle, an AFIT doctoral student, conducted several computational fluid dynamics (CFD) simulations on the baseline, fenced, and AFC configurations using ANSYS Workbench and Fluent in support of this study. The cell density for the half-wing simulation were set to approximately 7-8 million, depending on the configuration. The boundary-layer cell height was 0.002 mm to yield a $Y^+ < 1$. All of the computational data reported in this study comes from the same methodology presented in Naigle et al. (2022) with modifications to model the passive BLF and AFC slot configurations. All simulations were run with a Generalized k-ω (GEKO) turbulence model and in freestream conditions of 20 m/s. The AFC configuration was set up to blow air out of the jets at 153 m/s, which corresponded to a mass flow rate of 1,000 SLPM. Three AoAs for each configuration were run to compare to the

experimental data collected for the present study.

Data reduction and post-processing of these computational results allowed for accurate comparisons of flow properties at similar locations aft of the wings. There is observable consistency between the CFD flow visualizations and experimental tuft images at comparable locations aft of the body.

IV. Results and Analysis

4.1 Overview of Results

The use of active flow control (AFC) devices modified the baseline flow field sufficiently to explain performances differences noted in previous studies. There are two primary components of investigation in the scope this study: 1) identifying vortex location and movement and 2) characterizing wake and separation regions on and near the body. The first part, identifying vortex locations, was initially examined by long-exposure photography of a tuft mesh in the wake of the configurations. These preliminary images served as the starting point for conducting a more focused look using the triple wire traverse method described in Chapter II. The second part relied also on hot wire data planes to capture separation region growth for the various configurations as angle of attack increases and further validated separation observations in the tuft images. Computational data from an unpublished study in line with (Naigle et al., 2022) is examined to shed light on the expanding pressure gradients that form at the wing tips and cause the inboard motion of the wing tip vortices.

Two data planes were examined using the tuft mesh at 1.5 inches and 4.5 inches aft of the trailing edge. Data was collected for all three aforementioned configurations. Table 2 generalizes the matrix of test cases used in this study.

Table 2. Vortex Location Experiment Test Points

Config	AoA (°)	Data Plane
Clean	3, 8, 13, 18, 23, 28, 33	3, 4
Fence	3, 8, 13, 18, 23, 28, 33	3, 4
AFC	3, 8, 13, 18, 23, 28, 33	3, 4

The generalized experimental test matrix for characterizing the separation region is shown in Table 3. The two planes, #2 and #5, are forward of the trailing edge, as discussed previously.

Table 3. Separation Experiment Test Points

Config	AoA (°)	Data Plane
Clean	13, 18, 23	1, 2, 3
Fence	13, 18, 23	1, 2, 2
AFC	13, 18, 23	1, 2, 3

After obtaining preliminary vortex location information using the tuft plane, new runs with larger data planes were conducted in regions of greater interest. These data planes, discussed in Chapter III, were located at the seventh and tenth ceiling slots. This allowed for data collection at the 110% x/c (slot #7, DP 3) and at 130% x/c (slot #10, DP 4). Table 4 shows this test matrix.

Table 4. Vortex Identification Experiment Test Points

Config	AoA (°)	Data Plane
Clean	13, 18, 23	3, 4
Fence	13, 18, 23	3, 4
AFC	13, 18, 23	3, 4

Vortex breakdown and the onset of spanwise flow are two leading factors in delta wing stall. The analysis in this section will attempt to explain how these two mechanisms lead to stall by reducing velocity streams in directions that produce lift. Spanwise flow necessarily detracts from productive chordwise flow which facilitates low static pressures on the suction surface. Likewise, vortex breakdown describes a flow whose organized, energetic, spiraling core contributing to the same pressure gradients are weakened and tend towards disorder.

To objectively relate performance variations (maximum lift coefficient, stall AoA, lift curve slope, etc.) in each configuration to wake geometry, special care was taken to identify a) the relative locations of the primary vortex core, b) the relative magnitudes of spanwise flow, and c) chordwise location of initial vortex breakdown.

Figure 30, which compares Demoret's wind tunnel results of baseline, passive, and AFC configurations, shows clearly AFC lift performance diverges from the baseline

and fence model. The passive fence's impact alone, compared to the baseline, is on the order of 5% lift coefficient increase. As shown in Figure 30a, the baseline wing is shown to stall at about 18°, the fenced wing stalls at about 20°, and the maximum blowing AFC wing stalls at about 30°. Figure 30b reveals clustered drag performance for all models. The passive fence configuration shows higher drag until about 20 degrees at which point the fences are no longer exposed to the freestream flow.

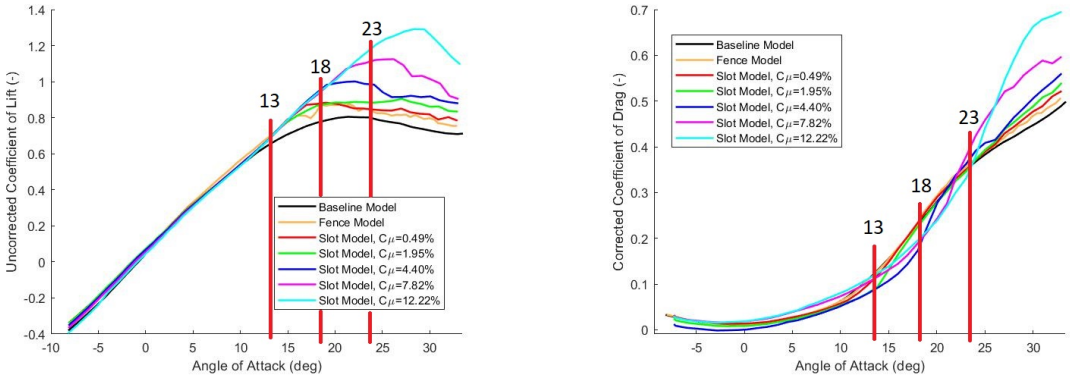

(a) Lift coefficient **(b) Drag coefficient**

Figure 30. Aerodynamic comparisons of configurations (Demoret, 2020)

4.2 Results and Discussion

4.2.1 Characterizing Vortex Structures

The main observation 10% aft of the trailing edge (DP 3) is that the clean configuration (Figure 31) shows growth of a homogeneous vortex centered around the wing tip as the AoA increases. The tufts show a unified vortex formed near the wing tip at 13° (a). As expected from delta wing aerodynamic theory, leading edge vortex (LEV) move inboard with increases in AoA, partially driven by the growing adverse pressure gradient near the wing tip. At 18° (b), around the clean wing C_{Lmax}, very little separation or recirculating flow is observed. It is not until 23° (c) until the separation region is pronounced enough to see effects leading to stall. By 28° (d), the

separation region is enlarged to about the same size of the vortex core, indicating the vortex is largely broken down.

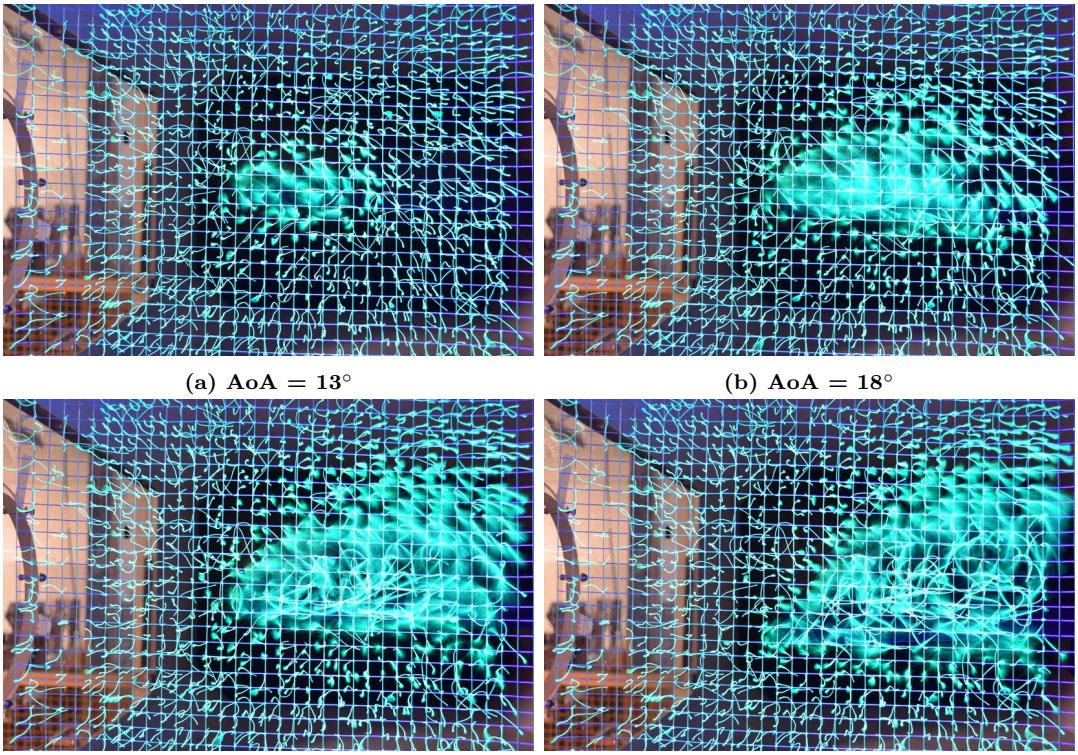

(a) AoA = 13° **(b) AoA = 18°**

(c) AoA = 23° **(d) AoA = 28°**

Figure 31. Clean configuration: tuft visualization at DP 3

In the passive, boundary-layer fence (BLF) wing (Figure 32) viewed at a distance 10% aft of the trailing edge, two distinct vortices are readily observed at 13° (a). One is identified as the wingtip vortex and the other the LEV. In this configuration, the distinct LEV directly results from the fence's truncating effect on the spanwise flow. By 18° (b), the two distinct vortex cores are still observable, but grow in magnitude. At 23° (c), separation and recirculating flow is visible in the center of the LEV, which is still distinct from the wing tip vortex. By 28° (d), the separation region is larger, but does not show the same advanced vortex breakdown that is visible in the clean configuration at the same AoA. It is evident the presence of the passive BLF delays the primary phenomena responsible for stall onset.

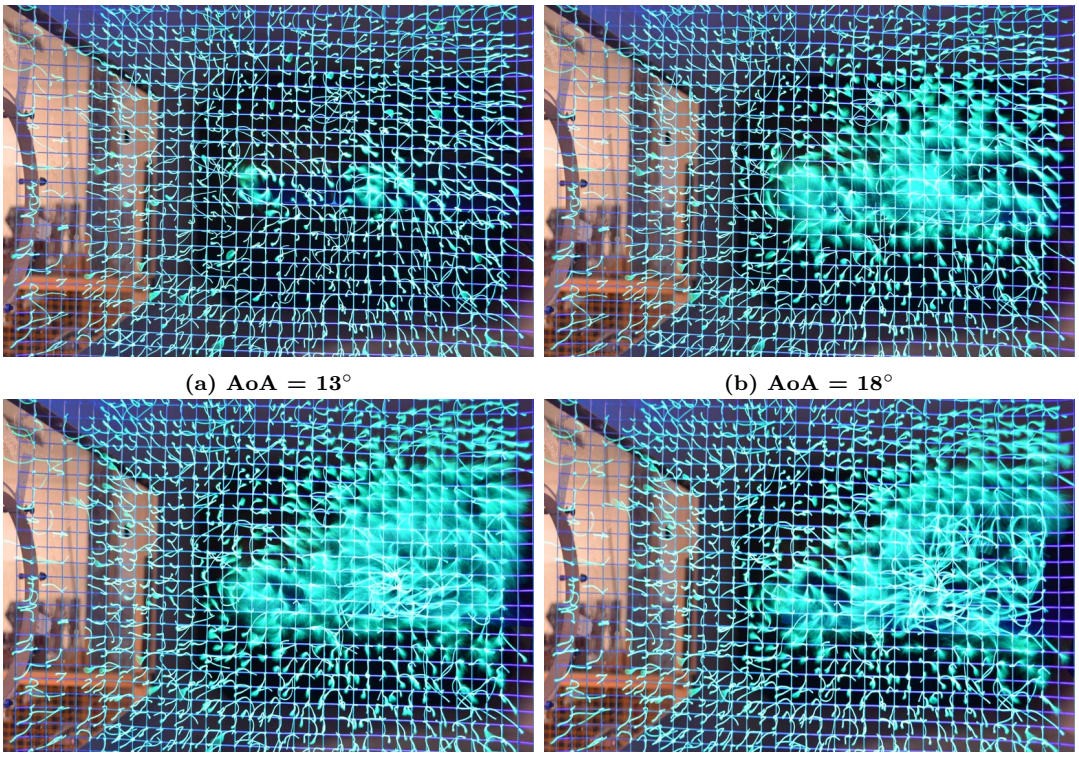

(a) AoA = 13° **(b) AoA = 18°**

(c) AoA = 23° **(d) AoA = 28°**

Figure 32. Fence configuration: tuft visualization at DP 3

In the active flow control (AFC) BLF wing (Figure 33), there are similarly two distinct vortices visible by 13° (a). Most of the observations for the passive BLF configuration are true to an even greater exttent in this AFC configuration. The wing tip vortex at 18° is smaller than the baseline and passive BLF configurations. The two vortices remain more distinct as the AoA increases and the region of separated flow is less extensive by 28° (d). At 23° (c), the separated flow region is more condensed about the center of the vortex compared to the same AoA in the passive BLF case (Figure 32).

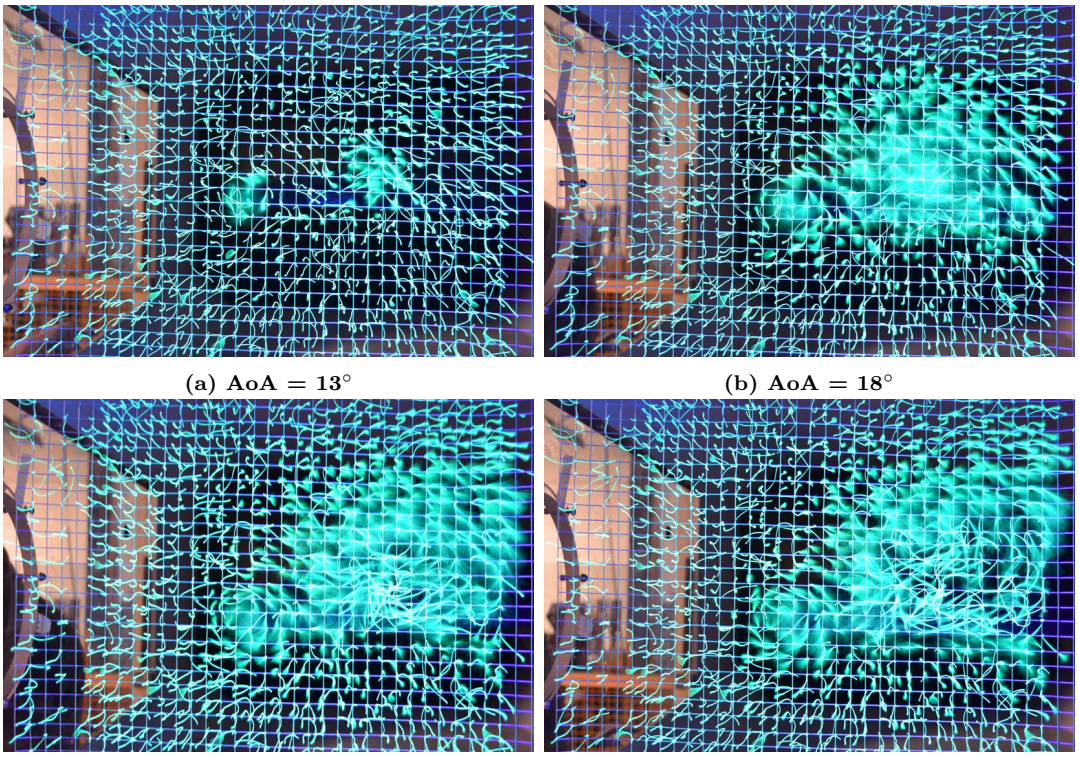

(a) AoA = 13° **(b) AoA = 18°**

(c) AoA = 23° **(d) AoA = 28°**

Figure 33. AFC configuration: tuft visualization at DP 3

The next data plane examined, affixed at DP 4, or 130% x/c, was used to track the evolution of the vortex cores as they moved downstream. Figure 34 shows the clean configuration's coalesced LEV and wingtip cores enlarged and more advanced in their breakdown. At 13° (a), the core, which was a tighter vortex forward of this location, is now widening and weakening. At 18° (b), the unified vortex has grown in diameter over the three inches it traversed from the previous data plane. Referring to Hitzel et al. (2016), the vortex breakdown begins in the center of the vortex and grows in the streamwise direction. Unsteadiness is observed at 23° (c) in the separated region because of the lack of still tufts which compounds to nearly 28° (d) that the breakdown is nearly complete and the region is primarily separated flow in the wake.

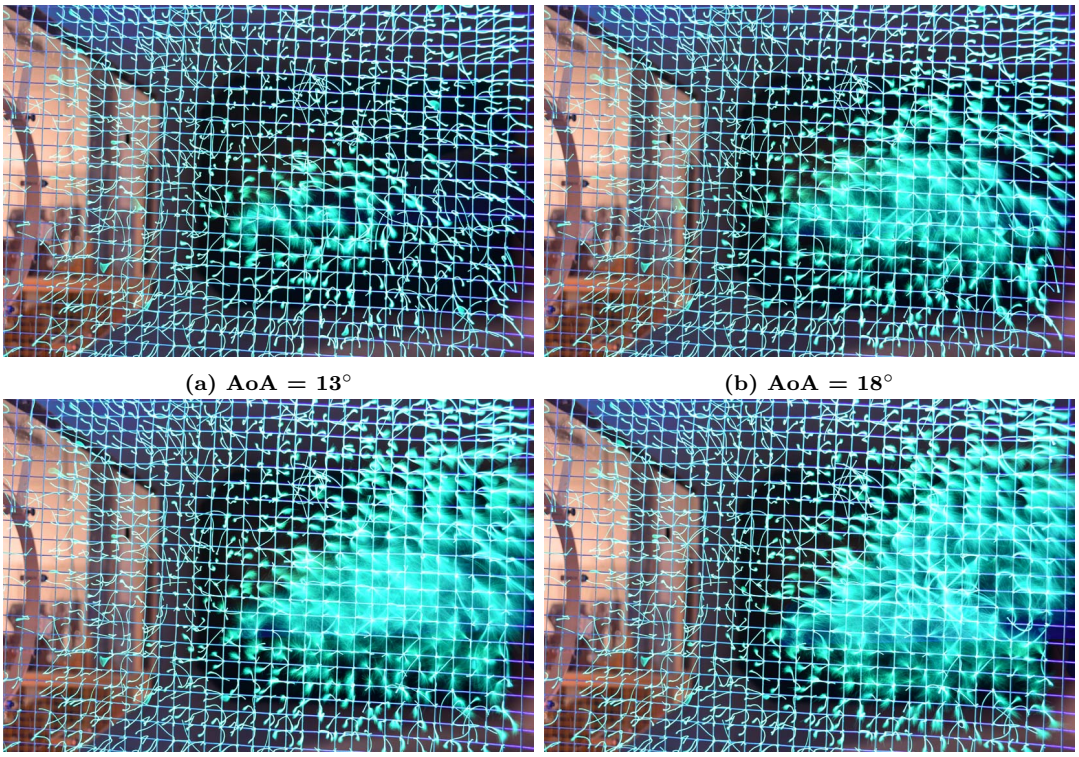

(a) AoA = 13° **(b) AoA = 18°**

(c) AoA = 23° **(d) AoA = 28°**

Figure 34. Clean configuration: tuft visualization at DP 4

The fenced configuration shows evidence of advanced vortex decay at this point downstream as well. Figure 35 (a) shows still distinct wing tip vortices and LEVs at 13°, but the collective magnitude of the disturbances to the tufts is noticeably lessened compared to the clean configuration. All the LEVs also seem to move inboard as they propagate downstream. At 18°, the LEV and wing tip vortex are still distinct. There is little evidence of re-circulation in the separated core at the same AoA it begins to onset in the clean configuration. This suggests the fence keeps the LEV more coherent at increased AoAs, as suggested by the data presented in Figure 30.

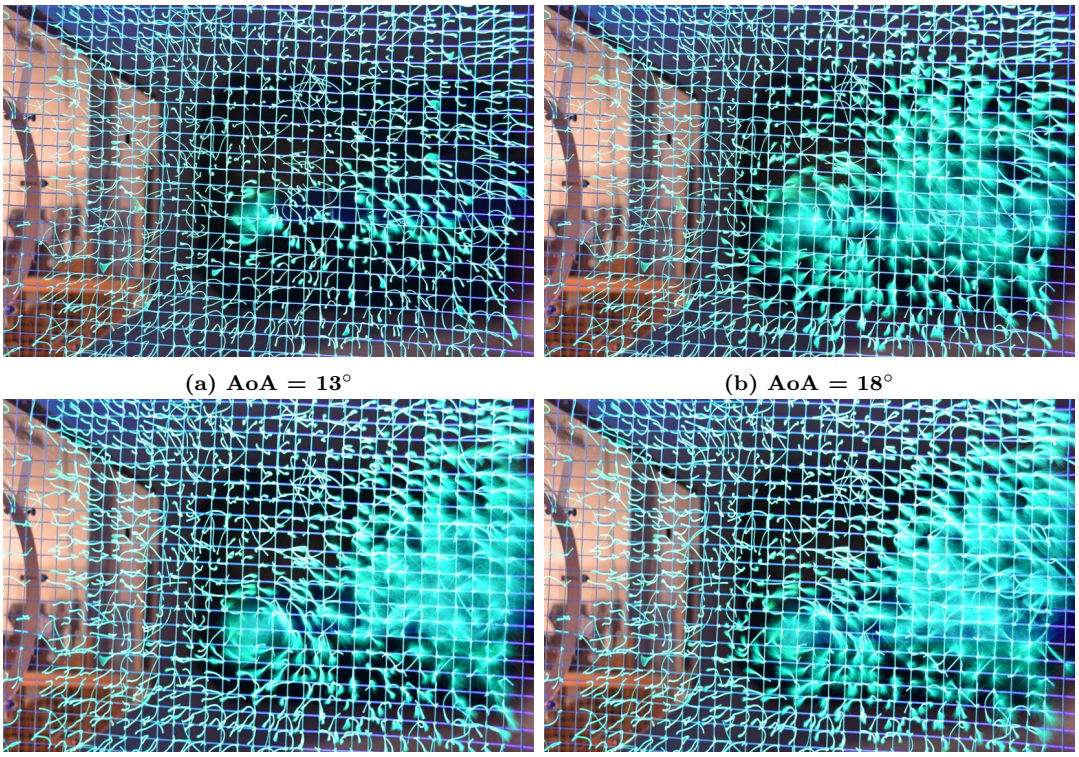

(a) AoA = 13° **(b) AoA = 18°**

(c) AoA = 23° **(d) AoA = 28°**

Figure 35. Fence configuration: tuft visualization at DP 4

The AFC configuration in Figure 36 viewed from the farther aft location shows similar, but more pronounced, features as the fenced configuration. The wing tip vortex and LEV are separate and distinct at DP 4. The vortices remain distinct even up to 28° where they are demarcated by a shear layer between them. The shear layer is not easily determined from the tufts alone, but will be further explained with the assistance of CFD in the following subsection. The decreased size of the vortices in the AFC case is especially noticeable in the tuft imagery. The momentum added to the flow field entrains fluid in the boundary layer and surrounding freestream which creates a low-pressure region between the two vortices, which draws them closer together as they propagate downstream. Higher-energy flow is observed in the more boldly blurred tufts, particularly seen at 23° and 28°.

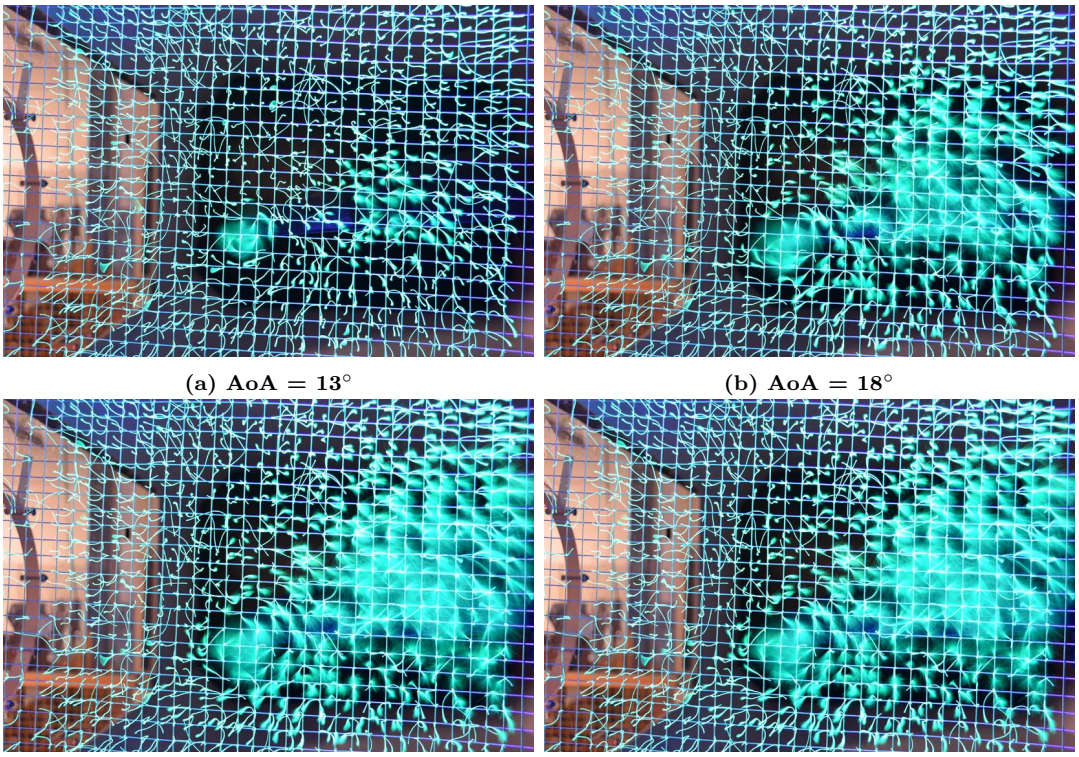

(a) AoA = 13° **(b) AoA = 18°**

(c) AoA = 23° **(d) AoA = 28°**

Figure 36. AFC configuration: tuft visualization at DP 4

Based on the locations of the vortices identified using tuft visualization, areas of interest were further examined using hot wire experimental methods and CFD. These methods captured flow properties in finite planes at discrete locations aft of the wing as discussed in Chapter II. Hot wire data are shown on the top row, CFD data are displayed in the middle row, and tuft images below that for similar configurations and distances for comparison.

Figure 37 shows a unified LEV and wing tip vortex. The lack of the AFC or passive BLF allows the LEV to migrate farther outboard and interact with the wing tip vortex to form a unified, large, and relatively weak primary vortex. The apparent merging of the two vortices results in a pressure relieving effect caused by spanwise fluid motion, ultimately leading to early separation. The separated flow leads to the eventual stall of the wing. Due to wing symmetry, the left and right wing have

counter-rotating vortex cores, which join in the middle with a downward motion, creating a pocket of low pressure air. This low pressure region incites both the LEV and wing tip vortex to join together.

These comparisons show remarkable consistency in identifying flowfield characteristics. The locations and distances between the LEV and wing tip vortex are in close agreement which provides confidence in interpreting the phenomena in one method using visualiztions from the others. The tuft images provide a baseline from which to look for two separate vortices in the AFC and BLF configurations and separation region relative size. The CFD data display the vortices with greater specificity in the form of a vector field overlaying vorticity, and the hot wire data shows the non-dimensional streamwise velocity highlighting the momentum deficit in the cores near the same locations as seen in the CFD and tuft images.

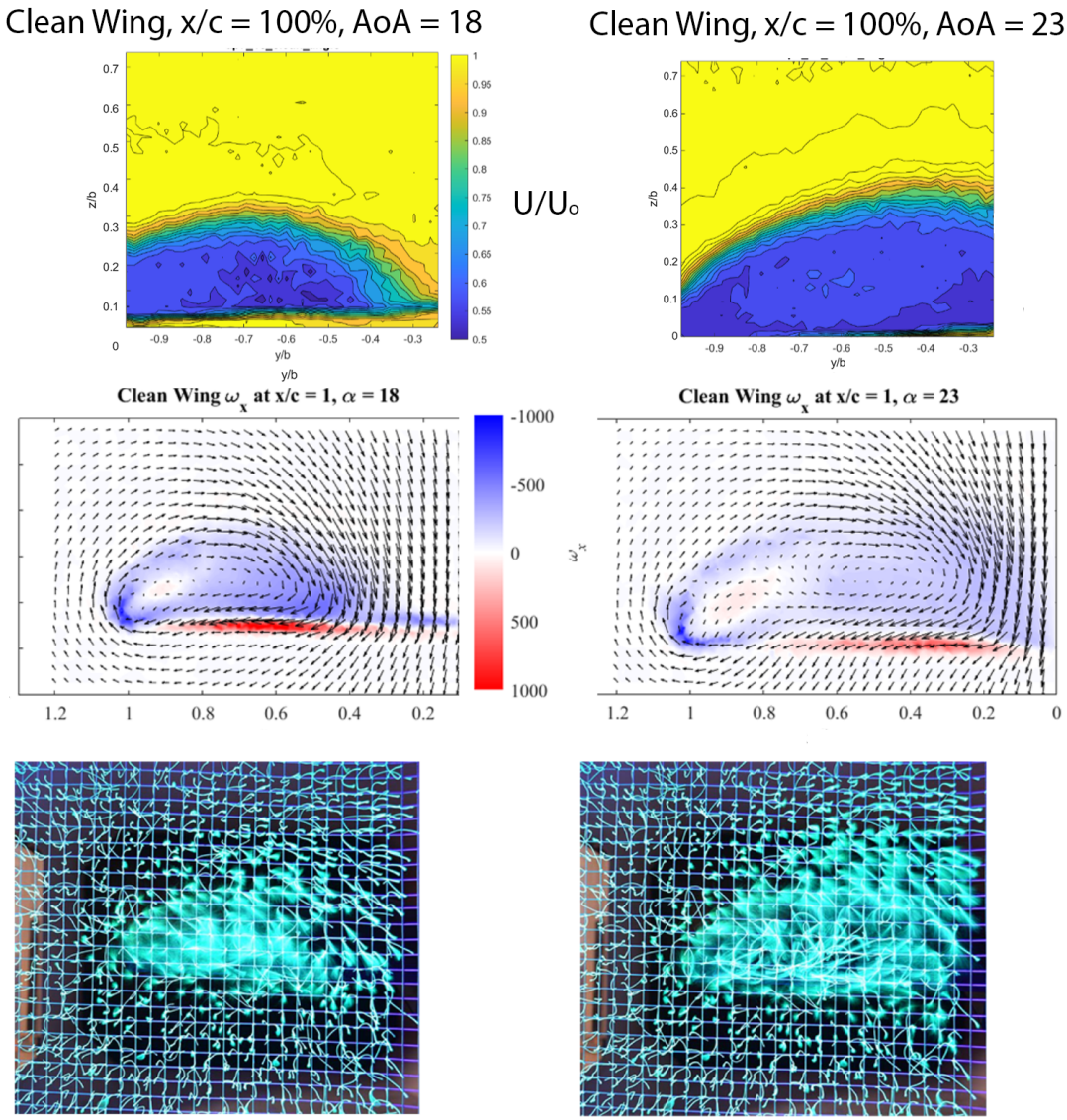

Figure 37. Clean wing data planes CFD

The fenced wing in Figure 38 shows with greater detail the distinct vortices. The wing tip vortex appears to be stronger and tighter along its path. As indicated by the adjacent red and blue contours, the vorticity shear between the two vortices is sharp. The increase in angle of attack shows an inboard migration by a nearly 10% span length. The CFD provides additional clarity of some wake features, namely the relative magnitudes of velocity at various parts of the flow field. The wing tip

vortex is far stronger than the LEV as indicated by the velocity vectors therein. The wing tip vortex proceeds uninhibited by boundary-layer spanwise flow because of the discontinuity enabled by the fence. The separation region shown in subfigure (b) corresponds to the approximate location of the separation region visible in the tufts (d). It is evident as a blurring of the vorticity as the sharp gradients lessen.

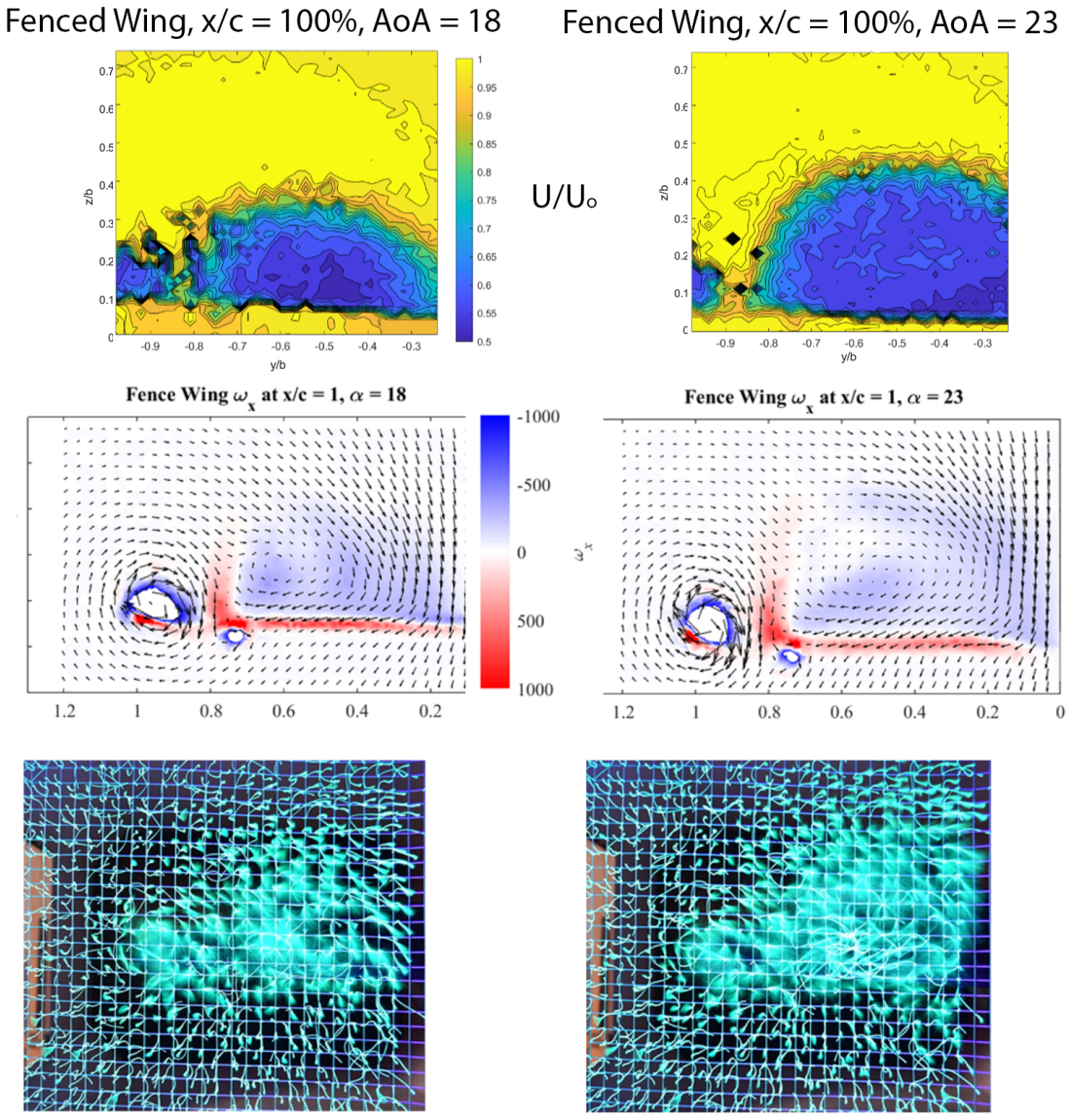

Figure 38. Fence wing data planes CFD

The AFC wing demonstrates in Figure 39 similar vortex separation seen in the

fenced wing, but with stronger vorticity gradients between the tip vortex and LEV. Most notable in this comparison is the lack of structural change from 18° to 23° in both the CFD and tuft images. The two counter rotating vortices in the AFC case demonstrate the strongest vorticiy gradients in any of the cases. The momentum added by the jet at the location of their intersection likely contributes to the increased vortex strength.

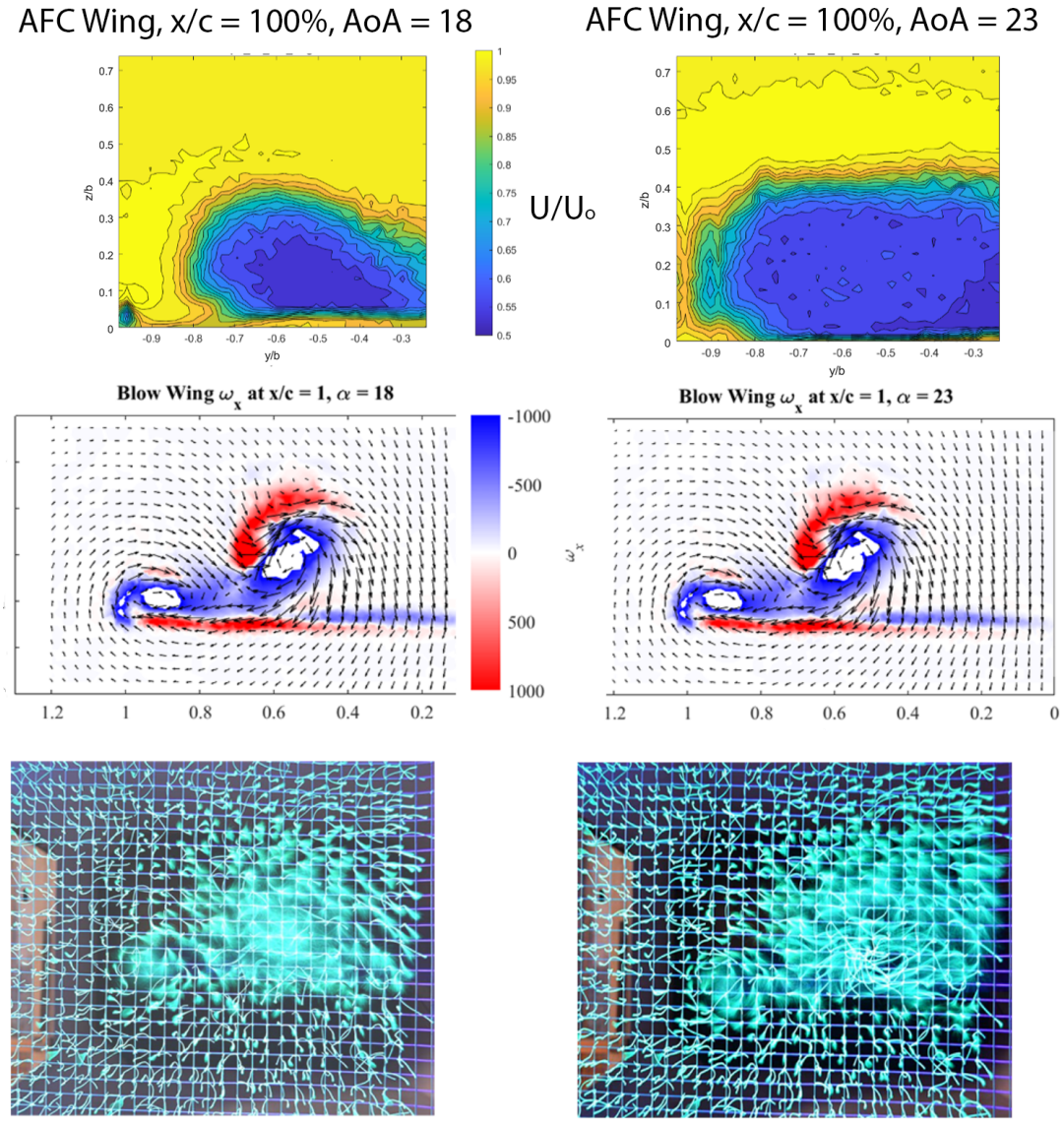

Figure 39. AFC wing data planes CFD

4.2.2 Plane Jet Performance

The plane jet flow control device was assumed in previous research to be uniform. A small investigation into the validity of that assumption showed that is not true in reality. An AFIT fluid measurements lab collected low-speed Schlieren imagery in support of this research and performed bench-top hot wire data to characterize the jet profile. The results of this study show decisively the narrow jet does not eject flow uniformly around the leading edge, but there is relatively uniform flow on the suction surface.

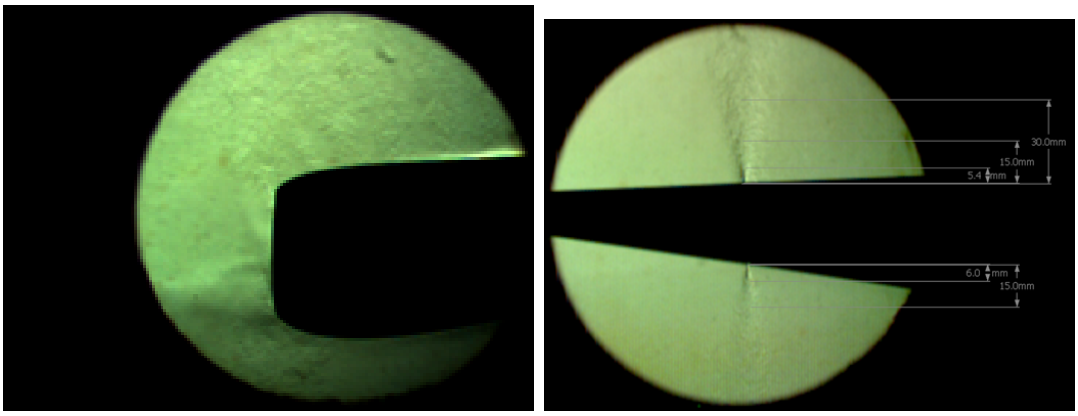

(a) View from the wing tip inboard **(b) View from the leading edge looking aft**

Figure 40. Schlieren imagery of AFC BLF blowing at 200 SLPM

4.2.3 Characterizing the Separation Region

The search for vortex cores in the hot wire data was carried out by plotting a velocity magnitude and the RMS velocity field. Because vortices are so unsteady, using RMS velocities has successfully aided researchers in past research efforts to identify their cores.

Figure 41 displays the the percent changes in streamwise velocity for the clean wing. The data was taken in the plane defined in Chapter III. Three angles of attack are presented to show the development of the separation region and highlight two

important takeaways. The first is that the spanwise flow decreases in magnitude in the separation region as it is halted by the adverse pressure gradient growing at the wing tip. The second observation is the apparent inboard motion shown by the large separation region expanding toward the center of the wing. The outer region of this visualization is collocated at the boundary of the separation region. Data plane (DP) 1, 2 and 3 are evaluated. DP 1 is approximately 4.5 inches forward of the trailing edge. Data plane 2 is three inches aft of DP 1 and DP 3 is three inches aft of DP 2.

The upper boundary of the separation region in the fence configuration, shown in Figure 41, is noticeably more shortened than in the baseline at each progressive angle of attack. The leftmost edge of the visible region shows that it is wider than the baseline configuration. The outboard edge of the region is truncated abruptly in the vicinity of the fence.

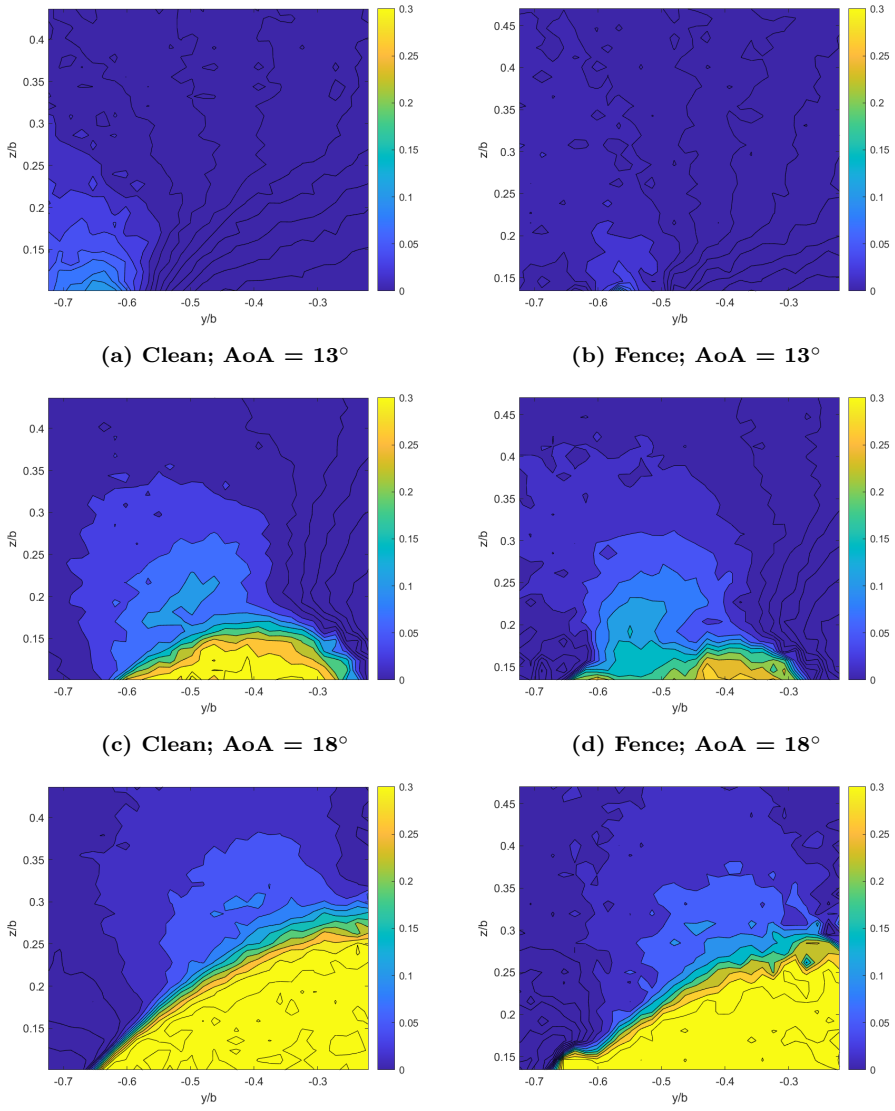

(a) Clean; AoA = 13° **(b) Fence; AoA = 13°**

(c) Clean; AoA = 18° **(d) Fence; AoA = 18°**

(e) Clean; AoA = 23° **(f) Fence; AoA = 23°**

Figure 41. Configuration comparison $\%\Delta U/U_\infty$ contour plot; at DP 1

Figure 42 shows the non-dimensional spanwise flow in the clean wing at DP 2. Comparing with the clean wing shown three inches forward in DP 1, the separation region enlarges and is shown to be outboard of the 70% span location. As the angle of attack increases to 18° (b), the separation region migrates inboard, which is consistent with the literature (Hitzel et al., 2016).

Also in Figure 42, the effect of fences is shown again to diminish the size of the

separation region in the spanwise direction and show signs of truncation around the BLF. At 13° (a), a small core, presumably the LEV, visible just inside the fence. At 18° (b), this core expands while maintaining a gap also in the vicinity of the fence. By 23° (c), the separation region encompasses the majority of the data plane's frame. The center of the core again shows inboard displacement.

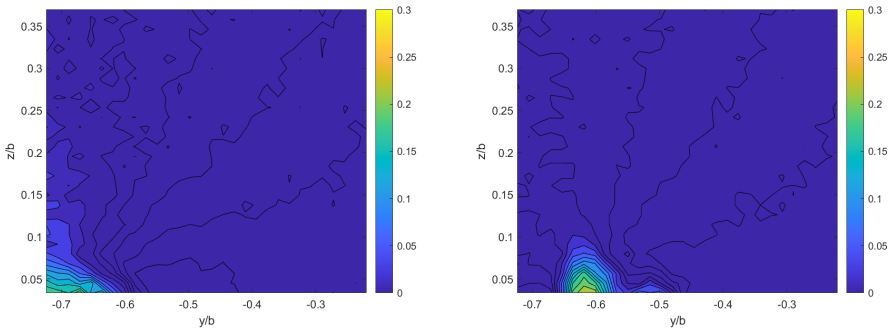

(a) Clean; AoA = 13° **(b) Fence; AoA = 13°**

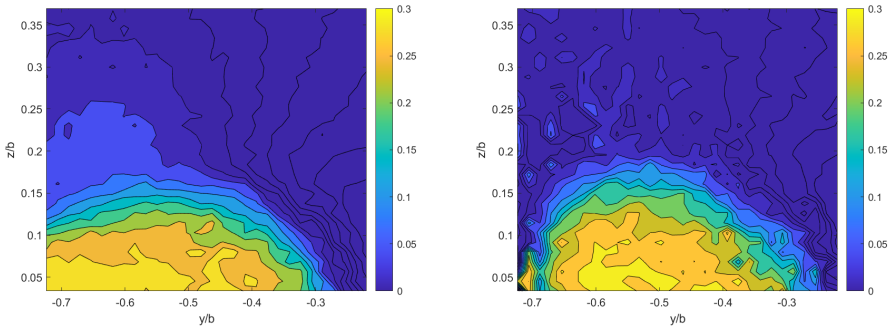

(c) Clean; AoA = 18° **(d) Fence; AoA = 18°**

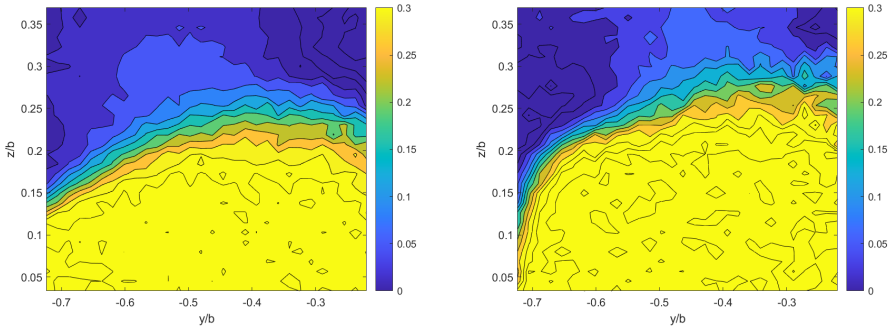

(e) Clean; AoA = 23° **(f) Fence; AoA = 23°**

Figure 42. Configuration comparison $\%\Delta U/U_\infty$ contour plot; at DP 2

Figure 43 shows configurations compared at DP 3, three inches aft of the previous

plane. The center of each core consistently shows inboard motion with increases in angle of attack. At 13° (a), the core is large and more in view than its counterpart in Figure 42. The center of the separation region at 18° (b) appears to move inboard about 10% of the span as well as grow in diameter by about two-fold. At 23° (c), the separated region is centered around the 50% span location and seems to double again in size from 18°. The passive BLF configuration viewed from data plane #8, shows a small separated region of reduced spanwise flow is visible just above the trailing edge at 65% span at 13° (a). At 18° (b), the center of the region migrates 5% z/b span inboard and the diameter increases four-fold. By 23°, the separation region grows to encompass the wing from the root to 75% and increases in diameter two-fold.

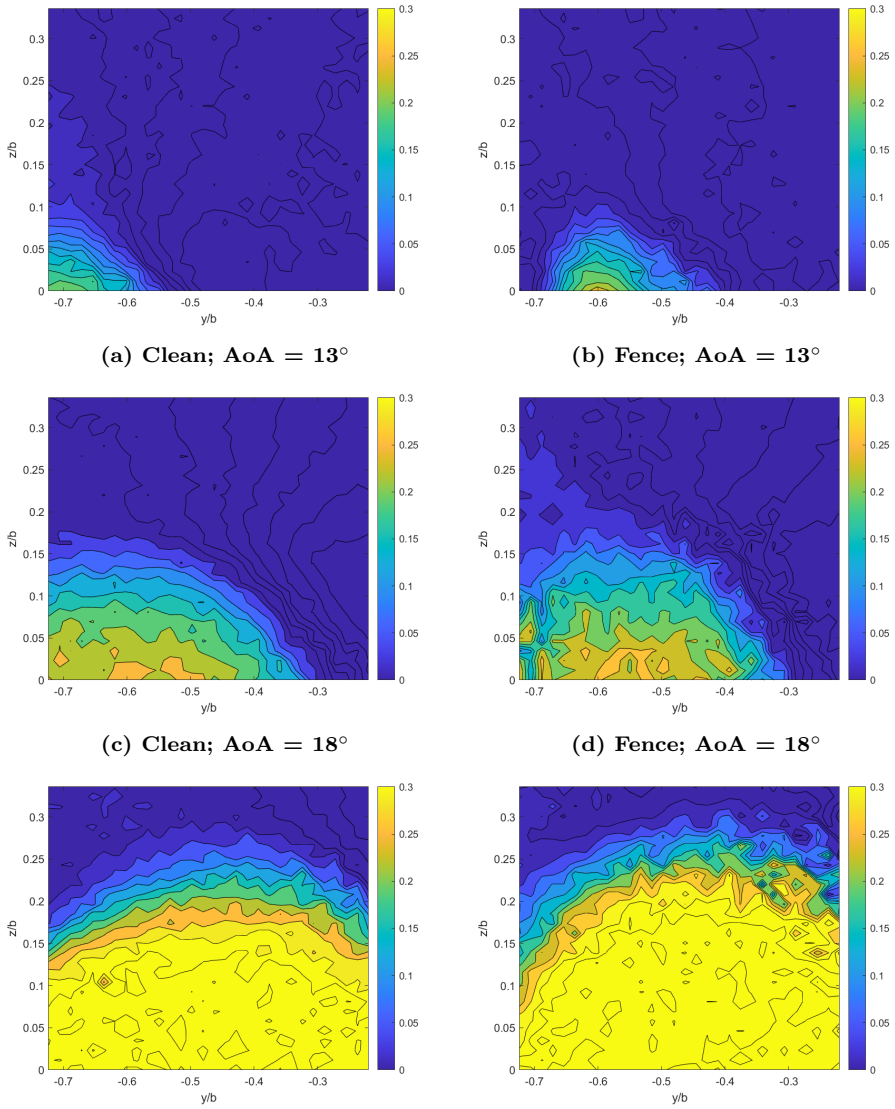

(a) Clean; AoA = 13° **(b) Fence; AoA = 13°**

(c) Clean; AoA = 18° **(d) Fence; AoA = 18°**

(e) Clean; AoA = 23° **(f) Fence; AoA = 23°**

Figure 43. Configuration comparison $\%\Delta U/U_\infty$ contour plot; at DP 3

4.2.4 Surface Pressure Gradients

Computational data shows an expanding pressure adverse spanwise pressure gradient at the wing tip, which constrains the LEV along a predictable path. Figure 44 shows the surface an expanding line of separation at the wing tip for increases in AoA from 18° to 23°. This separation line marks the boundary of an adverse pressure gradient in the spanwise direction is greater than in the streamwise direc-

tion, resulting in a streamwise path of least resistance. As the AoA increases, this growing region would account for the inboard motion of the leading edge vortices. The fence configuration's adverse pressure gradient is notably smaller at comparable AoAs because of the segmented separation regions discussed in Demoret (2020) and Walker (2018). The AFC wing in this figure shows almost no surface change. This is likely due to boundary-layer entrainment caused by the incredibly high mass flow rate being ejected out from the slot. The adverse pressure gradient at the boundary of the separation region is not visible like it is in the clean and fenced wings.

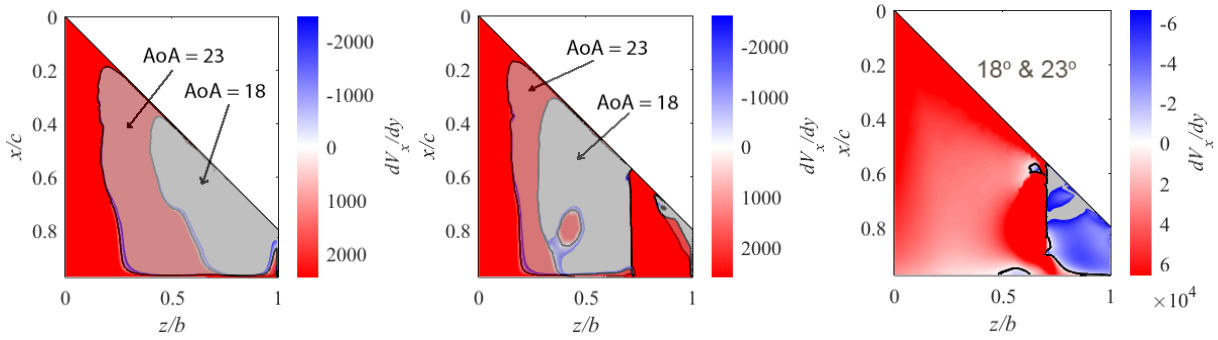

(a) Clean (b) Passive BLF (c) AFC BLF

Figure 44. Configuration surface plots

4.2.5 Turbulence Analysis

Figure 45 focuses on the normalized turbulent kinetic energy (*tke*) in the wake separation region planes. The clean wing's response to increases in the AoA is a notable, almost discrete, inboard jump in position. Referring back to Figure 44, the adverse pressure gradient for the clean wing exerts substantial enough pressure to counter the induced streamwise flow.

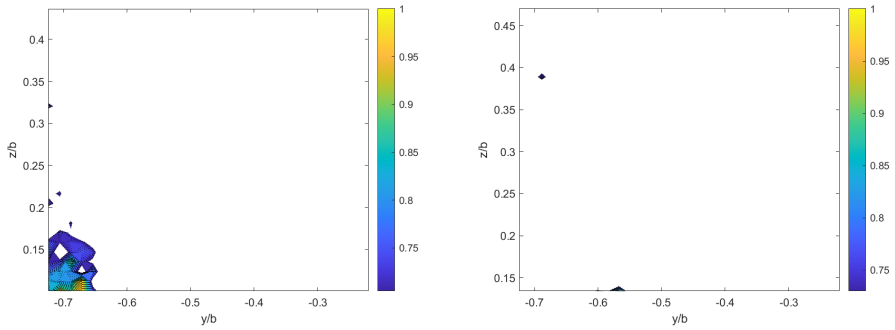

(a) Clean; AoA = 13°

(b) Fence; AoA = 13°

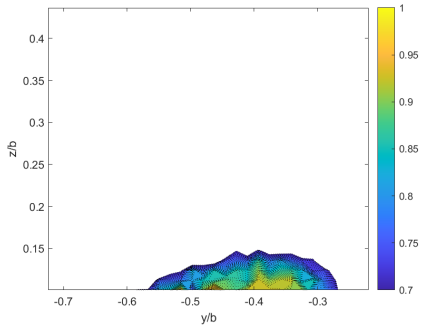

(c) Clean; AoA = 18°

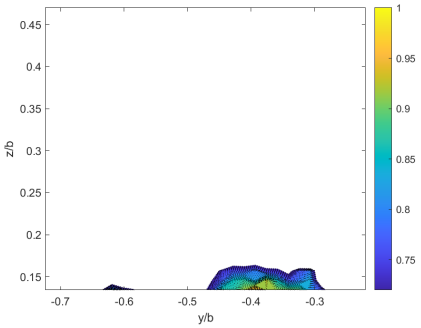

(d) Fence; AoA = 18°

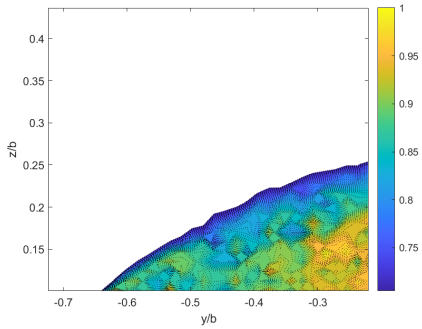

(e) Clean; AoA = 23°

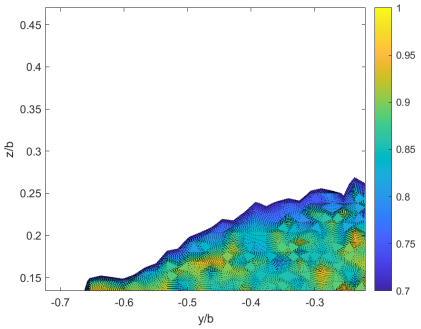

(f) Fence; AoA = 23°

Figure 45. Turbulent kinetic energy comparison contour plot; at DP 1

The fenced configuration shows a tighter and more coherent upper portion on the LEV and a smaller physical jump between AoAs. The explanation can partly be found in the smaller separation region formed by and adverse pressure gradient. The truncation of the spanwise flow permits the outboard portion of the wing to reset and regain lift effectiveness, pushing back on that region vice the clean wing.

The AFC wing demonstrates a decrease in the effective LEV diameter, an remark-

able increase in the concentrated turbulent kinetic energy, and moreover an increase in momentum. The flow entrained in the jet adds considerable mass flow to the flowfield. At 1000 SLPM, C_μ is 12% of the momentum of the whole flowfield around the wing's profile. The jet velocity, approximately 150 m/s, is strong enough to effect the flow passage in the boundary layer. The plane jet entrains fluid in the boundary layer and causes it to thin. The thinning results in delayed separation.

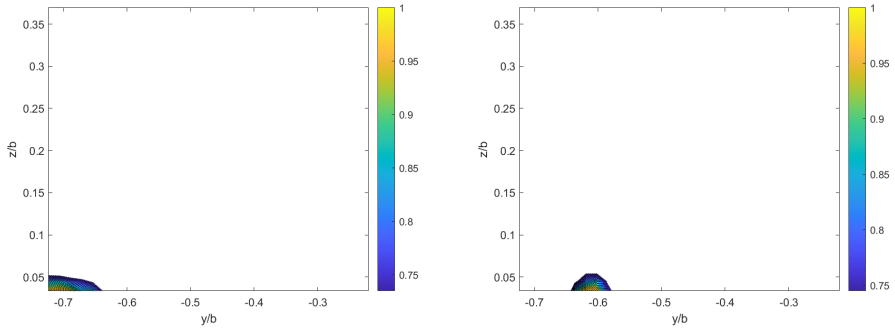

(a) Clean; AoA = 13°

(b) Fence; AoA = 13°

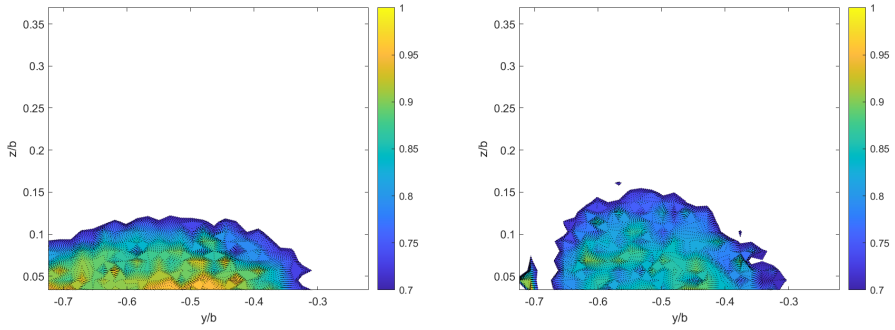

(c) Clean; AoA = 18°

(d) Fence; AoA = 18°

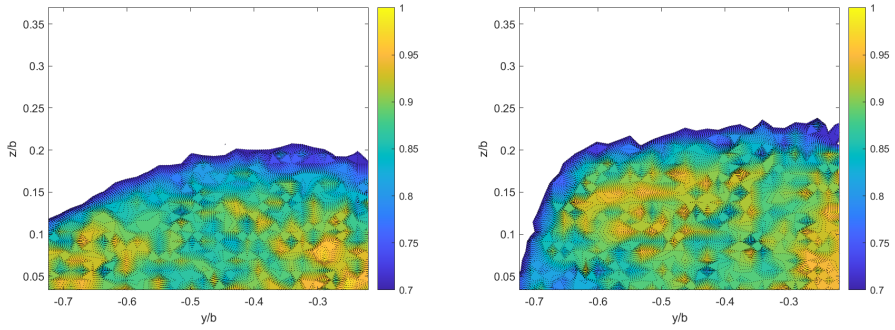

(e) Clean; AoA = 23°

(f) Fence; AoA = 23°

Figure 46. Turbulent kinetic energy comparison contour plot; at DP 2

Vortex decay is observed in the less concentrated pockets of turbulent kinetic energy and lessened gradients. By this point in the vortices trajectory, breakdown has begun. The fenced configuration remains farther inboard than the clean configuration. It can be attributed to the smaller pocket of adverse pressure pushing inboard from the fence itself. The presence of the fences truncates the spanwise flow and in so doing, permits a favorable pressure gradient inboard of the fence. The clean configuration shows the vortices following the general motion of the spanwise flow, even the boundary layer. At 18°, the fence and the clean configurations are markedly different in size and location, even more so than at 13°. Vortex inboard acceleration is noted. At 23°, the shear layer visible in the boundary between the core turbulent kinetic energy and freestream turbulent kinetic energy is deformed at the location of the fence. This visually explains the pressure gradient impact on the LEV inboard of the fence.

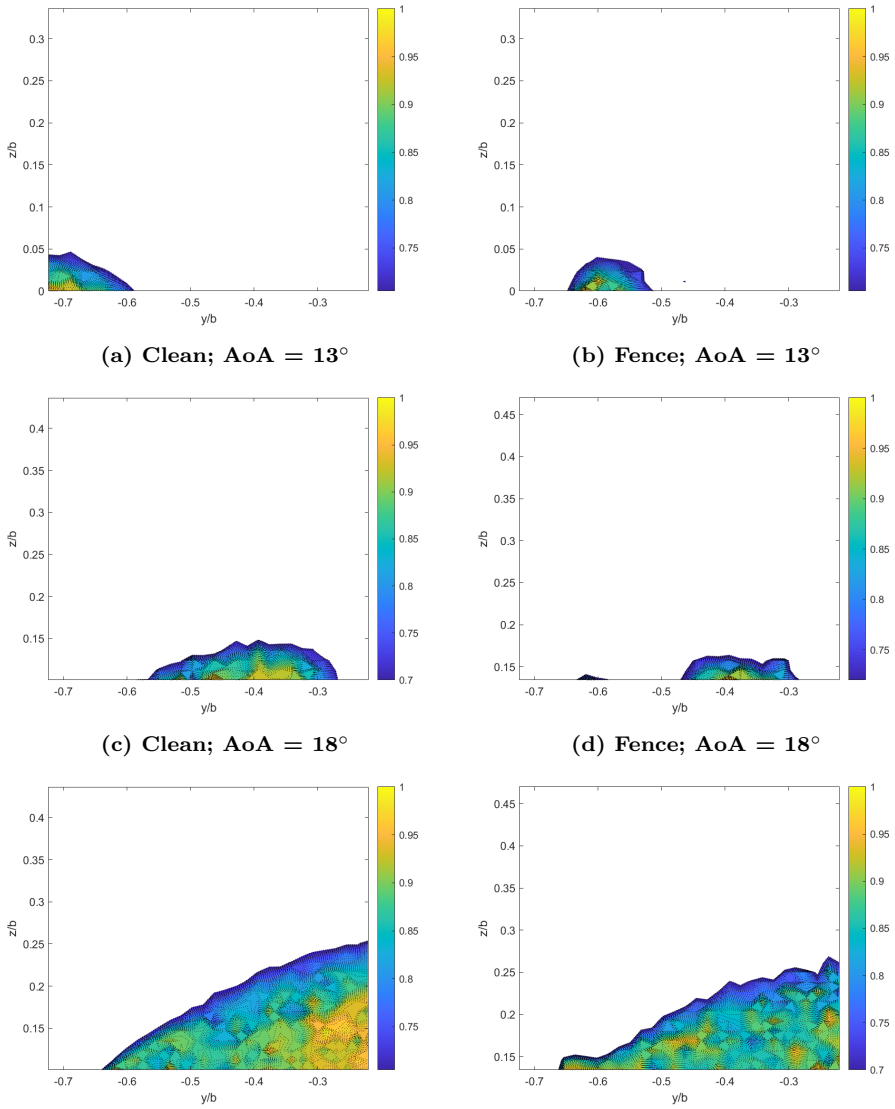

(a) Clean; AoA = 13° **(b) Fence; AoA = 13°**

(c) Clean; AoA = 18° **(d) Fence; AoA = 18°**

(e) Clean; AoA = 23° **(f) Fence; AoA = 23°**

Figure 47. Turbulent kinetic energy comparison contour plot; at DP 3

From the derived turbulent kinetic energy plots, the vortex core was determined. The vortex circulation was then found using the method described in the previous chapter and is compared in Figure 48. Note increases in AoA result in increased circulation, corresponding to the increase in the size of the vortex. The fenced configuration showed lower circulation than the clean wing closer to the wing body, but aft of the TE the trend reverses. Wings with active flow control devices indeed do

maintain the vortex core for longer along its path than wings without. A coherent LEV core is observed in Figure 45, and is quantitatively validated by the circulation estimates.

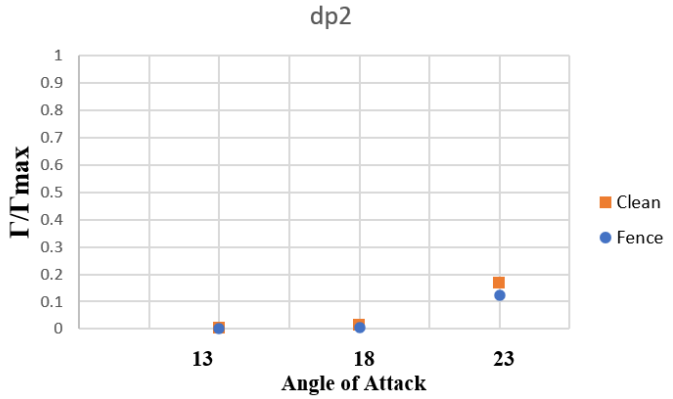

Figure 48. Circulation comparisons at DP 1

Near the trailing edge, at DP #5, the relative, normalized circulation in the LEV increases in magnitude. This suggests that as the vortices propagate downstream, the fluid they entrain causes an increase in the net turning about the vortex. The fence configuration is again shown to have less circulation than its clean counterpart. One possible explanation is the vortex is more coherent. This is enabled by the fence which constrains all the energy to a very small, effective center. The clean configuration, while larger in magnitude, is less efficient with its uncontrolled energy.

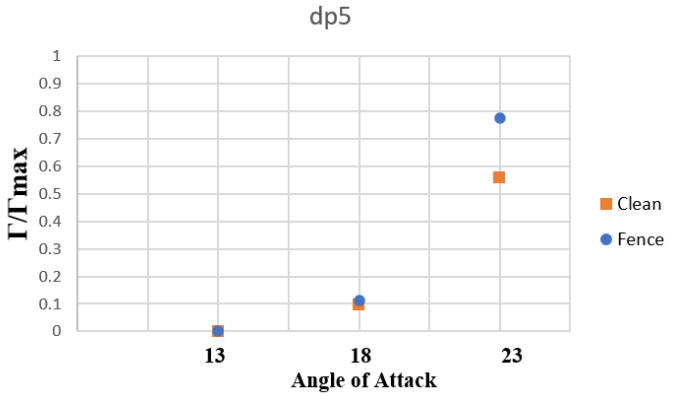

Figure 49. Circulation comparisons at DP 2

As previsouly mentioned, the circulation trend reverses aft of the trailing edge. The fenced configuration is shown to have higher circulation in at all three AoAs. If the clean wing LEV is breaking down by the time it reaches the trailing edge, the drop in relative circulation could be attributed to the comparative coherence found in the fenced wing. The clean wing LEV breaks down and immediately drops in turbulent kinetic energy, while the controlled wing maintains a coherent vortex for longer, delaying vortex breakdown and wing stall.

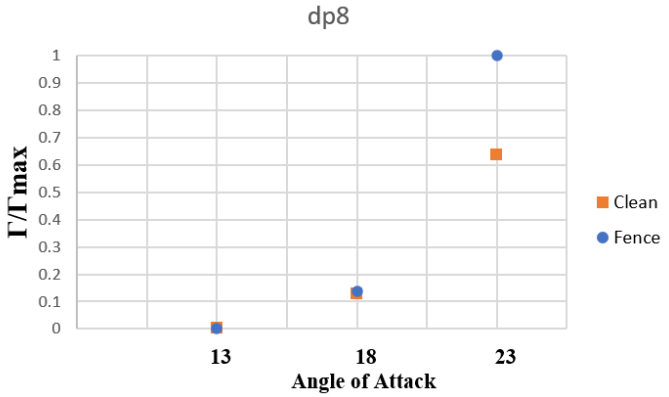

Figure 50. Circulation comparisons at DP 3

Figure 51 shows the Reynolds stressis *u'v'* in the wake at data plane #2. At 13°, both the clean and fenced wings exhibit relatively low Reynolds stresses near the freestream, and the larger magnitudes near the top of the LEVs. At 18°, the largest magnitude Reynolds stresses are found above the LEV, highlighting the shear layer. By 23°, the clean wing's shear layer is thinner and the Reynolds stress is larger, however the height of the LEV is notably larger than the fenced-wing configuration.

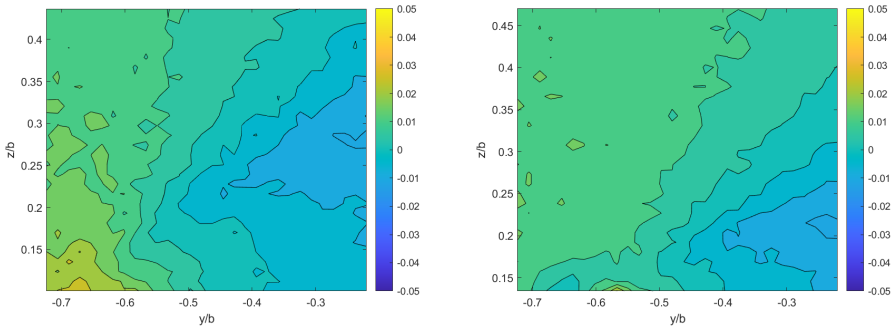

(a) Clean; AoA = 13°

(b) Fence; AoA = 13°

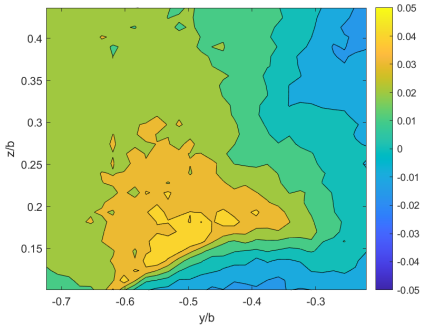

(c) Clean; AoA = 18°

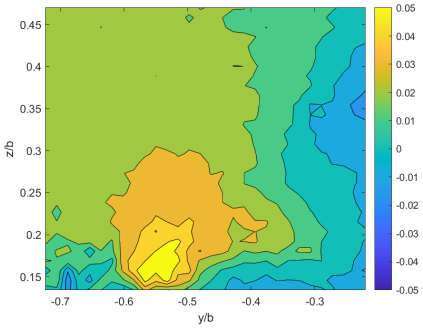

(d) Fence; AoA = 18°

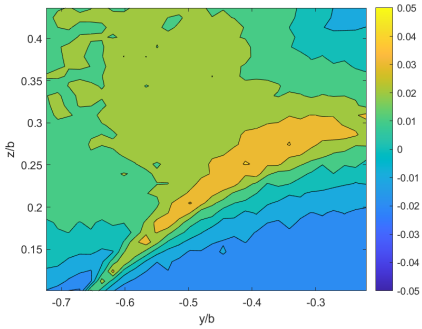

(e) Clean; AoA = 23°

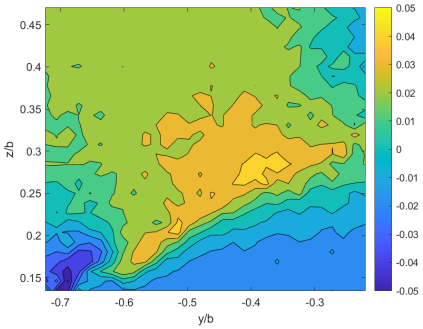

(f) Fence; AoA = 23°

Figure 51. Reynolds' Stress *u'v'* at DP 1

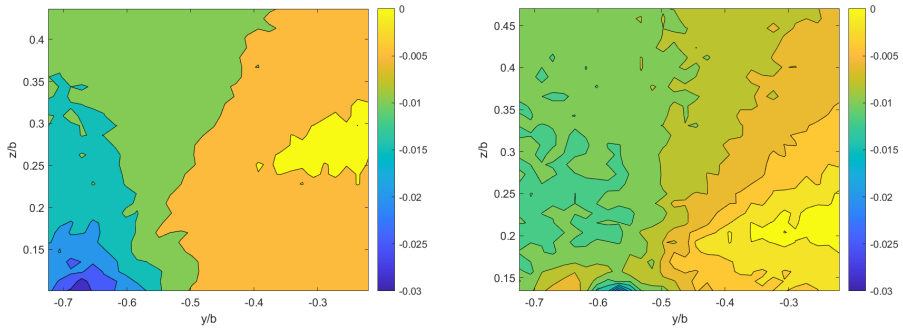

(a) Clean; AoA = 13°

(b) Fence; AoA = 13°

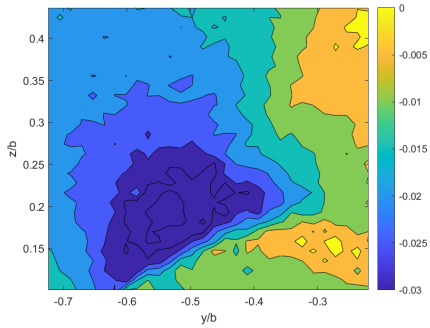

(c) Clean; AoA = 18°

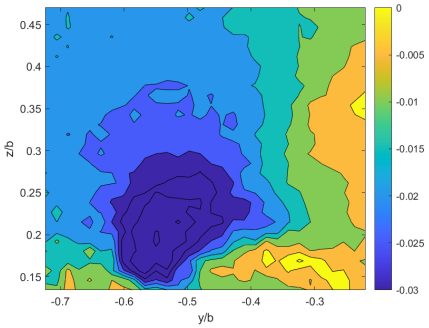

(d) Fence; AoA = 18°

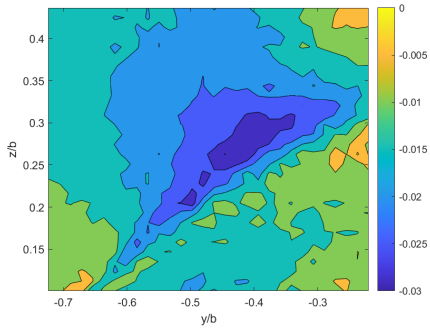

(e) Clean; AoA = 23°

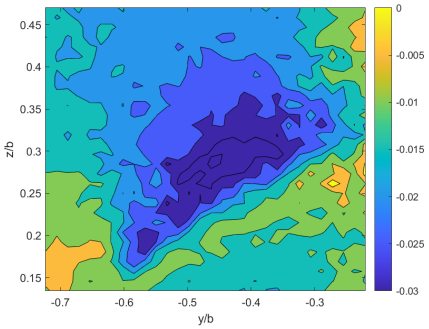

(f) Fence; AoA = 23°

Figure 52. Reynolds' Stress *u'w'* at DP 1

At data plane #8, the trends are similar, but the initial locations of peak Reynolds stress are higher off the wing. As the vortex separates, its magnitude is notably larger at 18° than at 23°. The flow becomes progressively more isotropic as the coherent vortex structure begins to break down. The lowest-magnitude Reynolds stresses occur just inside of the vortex, indicating general turbulent isotropy in the vortex core. The shear layer is readily identified at the boundary between the high-

and low-magnitude regions where the sharp gradient delineates the boundary between the LEV and freestream. The locations identified in these images are consistent with the cores identified with turbulent kinetic energy.

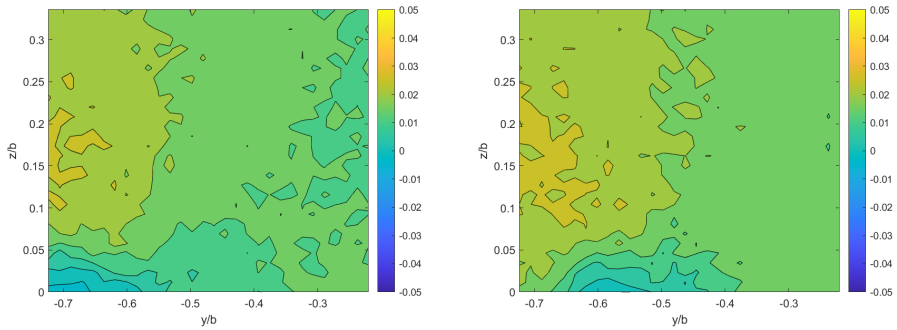

(a) Clean; AoA = 13° **(b) Fence; AoA = 13°**

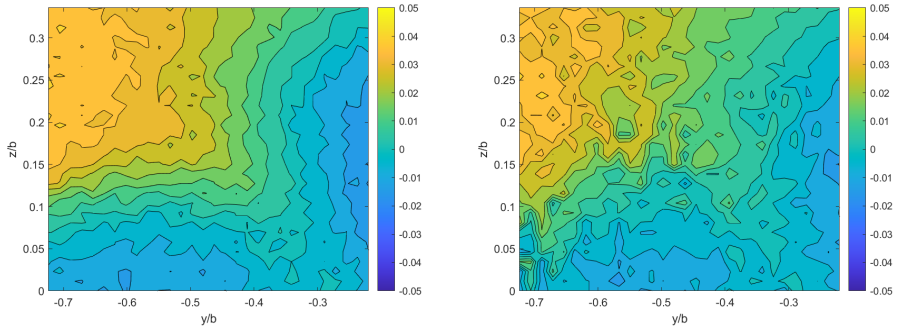

(c) Clean; AoA = 18° **(d) Fence; AoA = 18°**

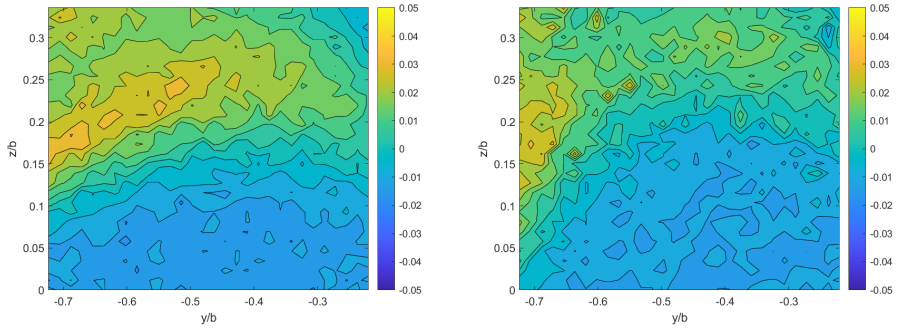

(e) Clean; AoA = 23° **(f) Fence; AoA = 23°**

Figure 53. Reynolds' Stress *u'v'* at DP 3

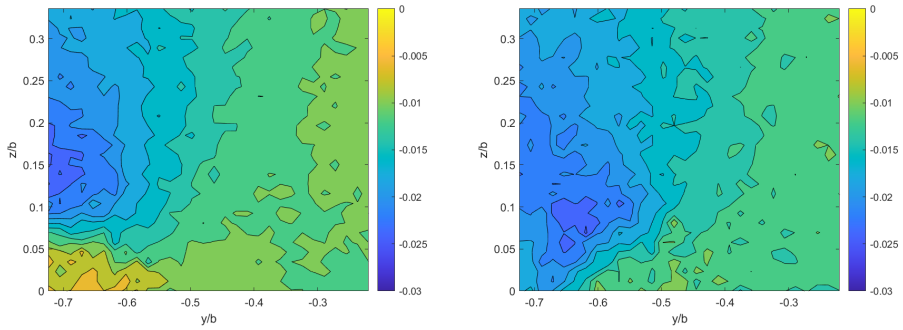

(a) Clean; AoA = 13° **(b) Fence; AoA = 13°**

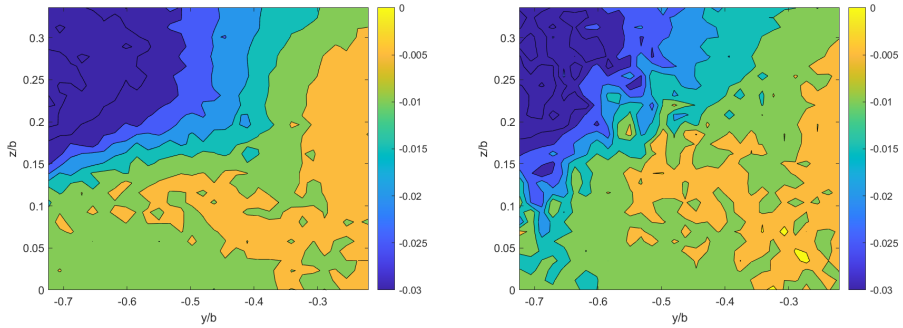

(c) Clean; AoA = 18° **(d) Fence; AoA = 18°**

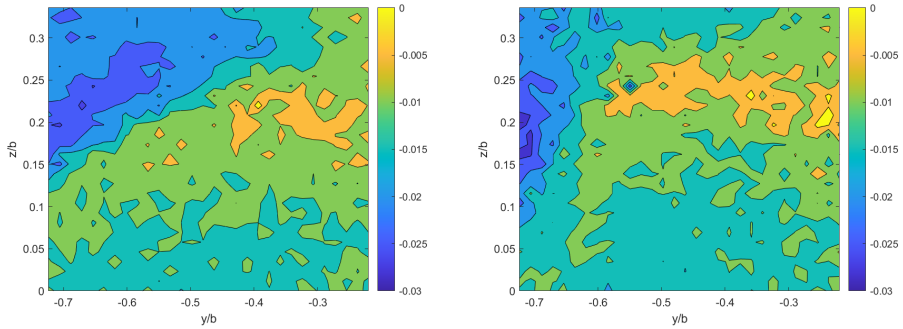

(e) Clean; AoA = 23° **(f) Fence; AoA = 23°**

Figure 54. Reynolds' Stress *u'v'* at DP 3

The normalized Reynolds stresses, both *u'v'* and *u'w'*, are in the same order of magnitude as they are in the boundary layer described in Pope (2000).

4.2.6 Reference CFD Data Planes

The following images characterize the flowfield behind the same three configurations computationally at four discrete planes in the wake. The first data plane is at

90% chordlength, the second is at 100% chordlength, the third is at 110% chordlength, and the fourth is at 120% chordlength. These data were collected on the HPC for this research effort in accord with the research conducted in **?**. Figure 55 shows each wing at 18° and Figure 56 shows the planes of each configuration at 23° displays a different configuration in each column. Subsequent data planes are incremented each row. The left-most column is the clean wing, the middle column is the fenced wing, and the right-most column is the AFC wing.

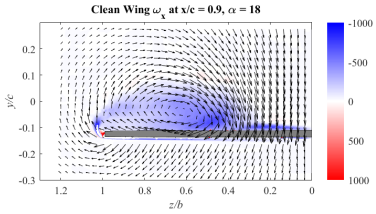

(a) Clean; 90% x/c

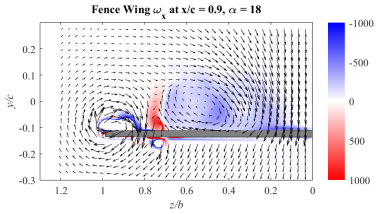

(b) Fence; 90% x/c

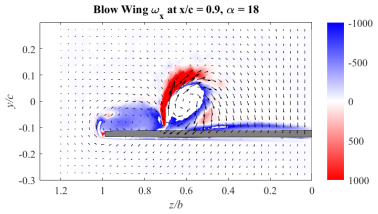

(c) AFC; 90% x/c

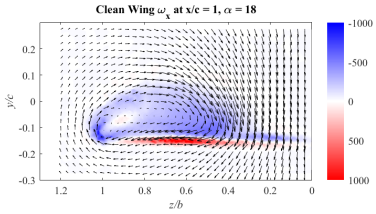

(d) Clean; 100% x/c

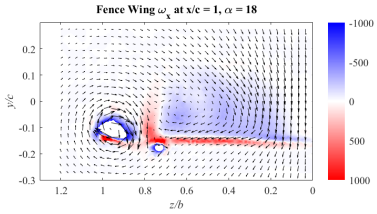

(e) Fence; 100% x/c

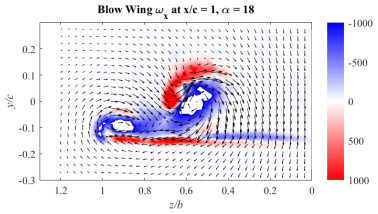

(f) AFC; 100% x/c

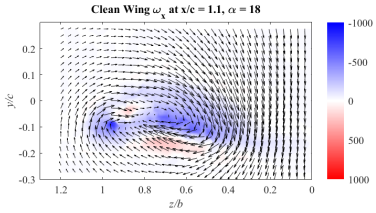

(g) Clean; 110% x/c

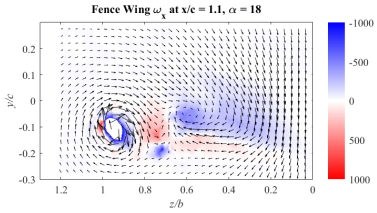

(h) Fence; 110% x/c

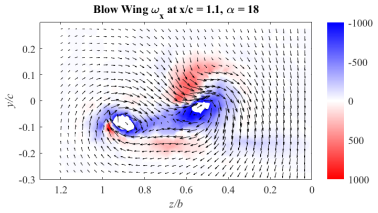

(i) AFC; 110% x/c

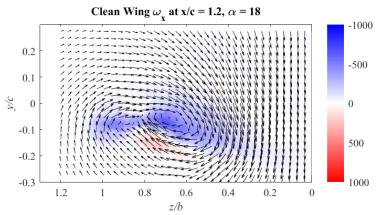

(j) Clean; 120% x/c

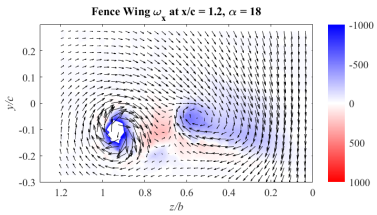

(k) Fence; 120% x/c

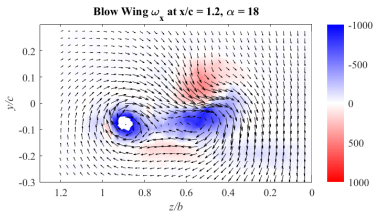

(l) AFC; 120% x/c

Figure 55. Wake data planes for CFD configurations at 18°

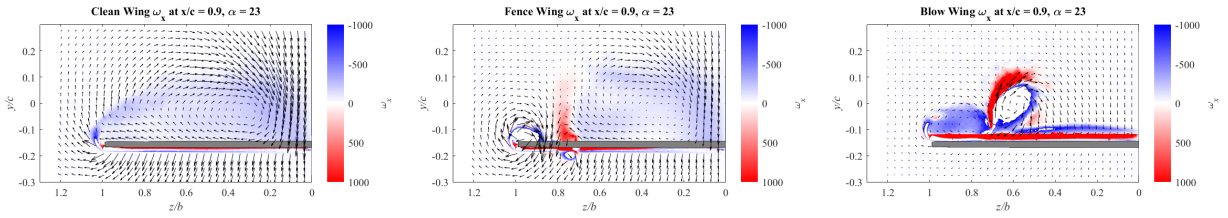

(a) Clean; 90% x/c **(b) Fence; 90% x/c** **(c) AFC; 90% x/c**

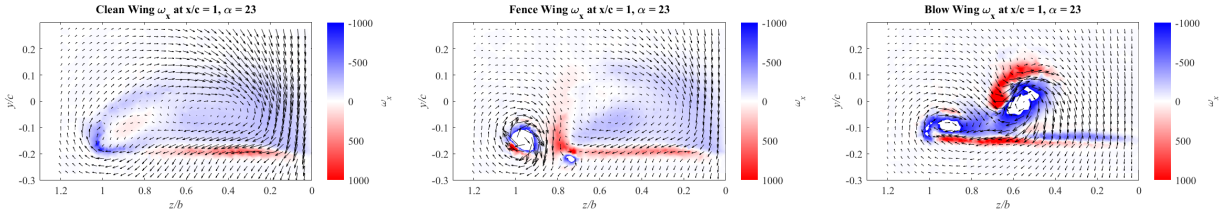

(d) Clean; 100% x/c **(e) Fence; 100% x/c** **(f) AFC; 100% x/c**

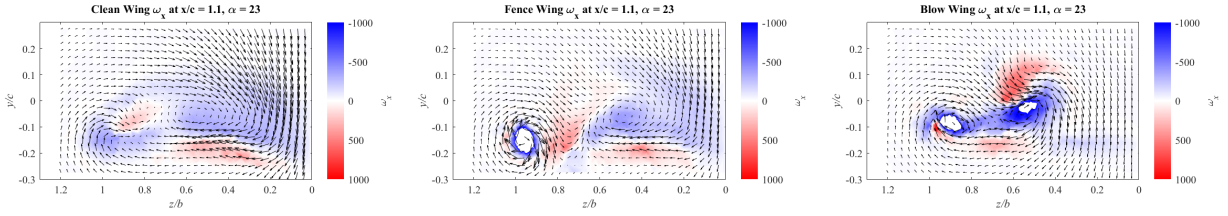

(g) Clean; 110% x/c **(h) Fence; 110% x/c** **(i) AFC; 110% x/c**

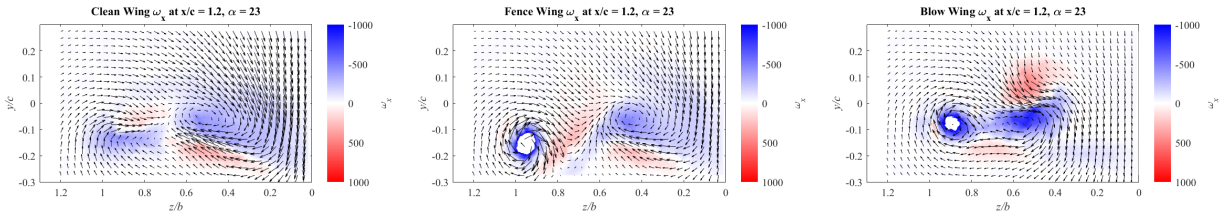

(j) Clean; 120% x/c **(k) Fence; 120% x/c** **(l) AFC; 120% x/c**

Figure 56. Wake data planes for CFD configurations at 23°

Figure 57, 58, and **??** show the non-dimensional spanwise velocity normalizied by the freestream velocity for DP 1, 2, and 3, respectively. In these, the effect of flow control is shown to truncate spanwise flow. In each configuration comparison, boundary-layer fences minimize the size of the lobe of spanwise flow near the wing.

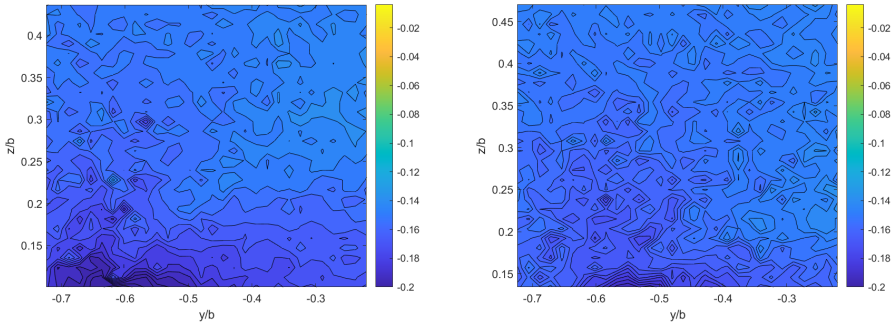

(a) Clean, 13° **(b) Fence, 13°**

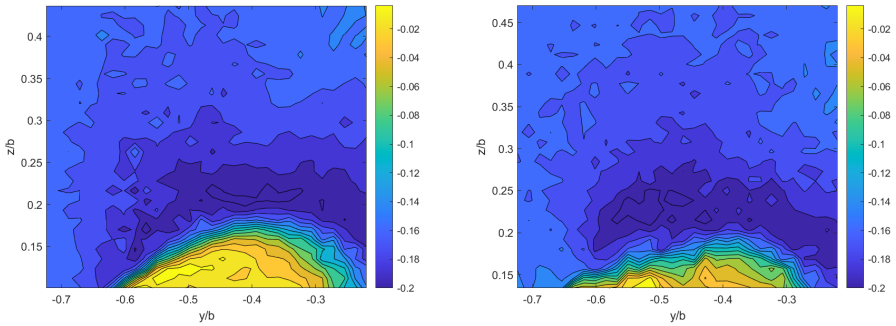

(c) Clean, 18° **(d) Fence, 18°**

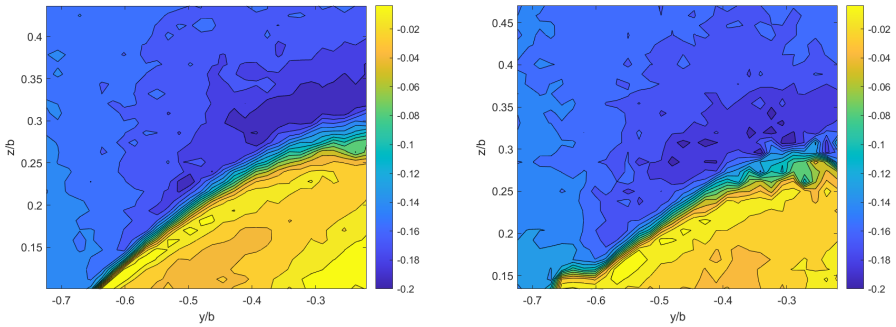

(e) Clean, 18° **(f) Fence, 23°**

Figure 57. Non-dimensional V-velocity; at DP 1

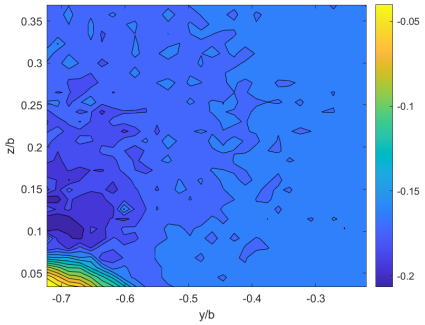

(a) Clean, 13°

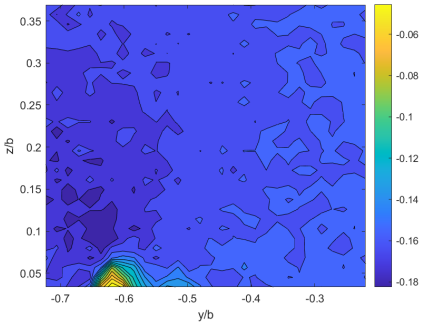

(b) Fence, 13°

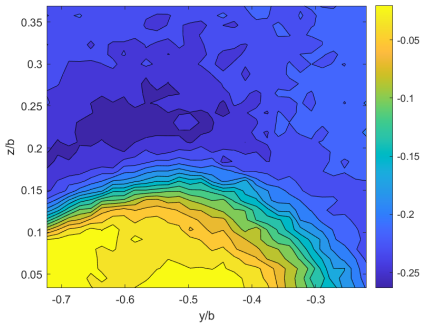

(c) Clean, 18°

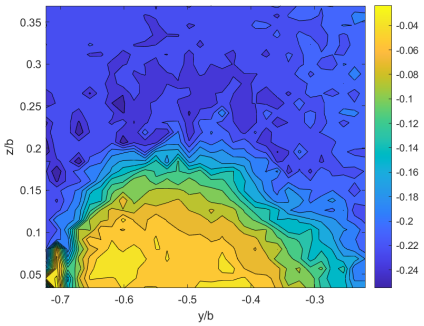

(d) Fence, 18°

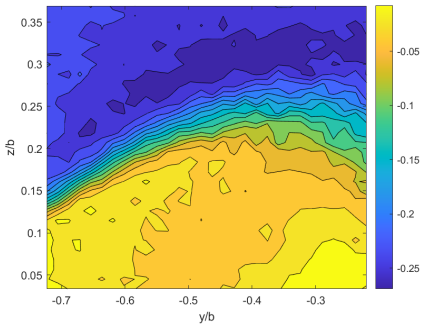

(e) Clean, 18°

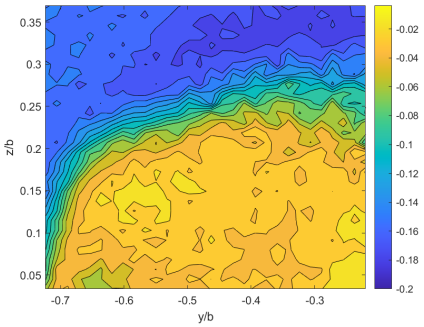

(f) Fence, 23°

Figure 58. Non-dimensional V-velocity; at DP 2

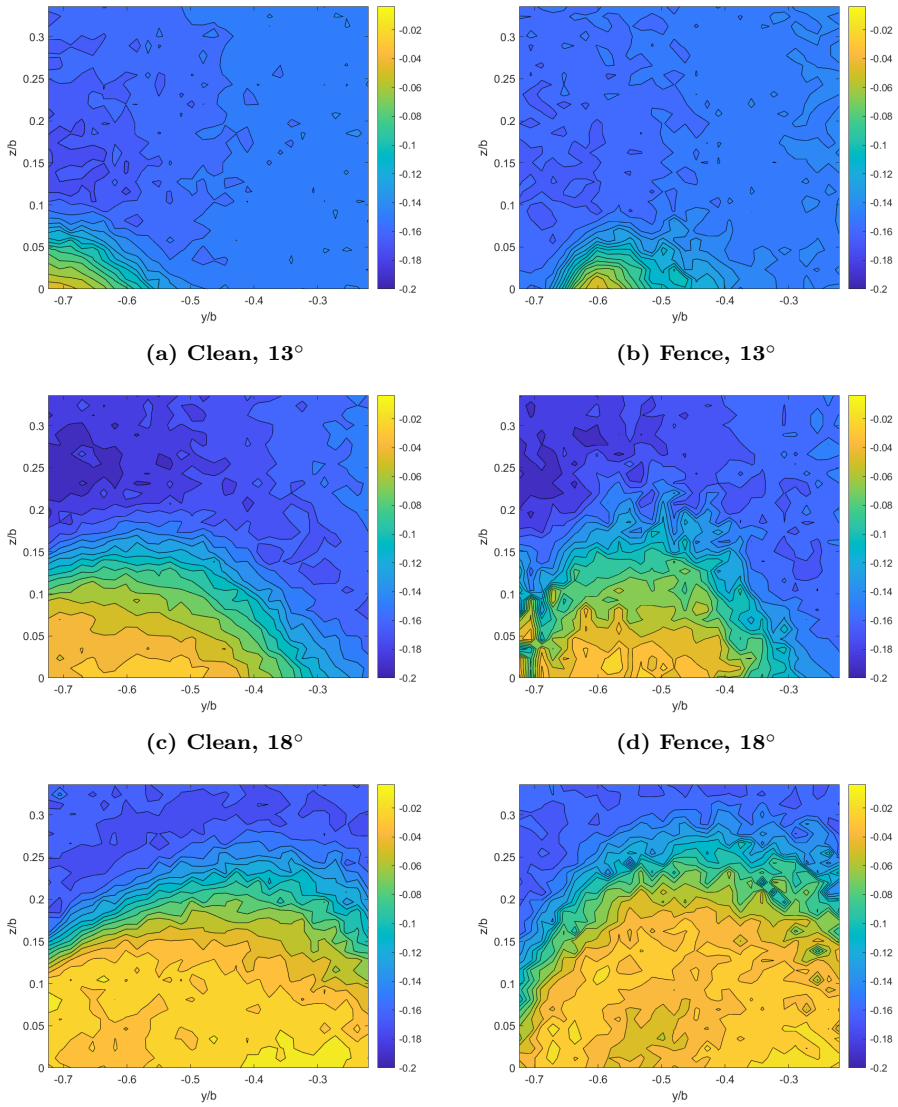

(a) Clean, 13° **(b) Fence, 13°**

(c) Clean, 18° **(d) Fence, 18°**

(e) Clean, 23° **(f) Fence, 23°**

Figure 59. Non-dimensional V-velocity; at DP 3

Figure 60, 61, and 62 show the non-dimensional downward velocity component normalizied by the freestream velocity for DP 1, 2, and 3, respectively. In these, the entrainment of freestream flow into the LEVs are seen. The region of highest downward motion is seen immediately above the primary LEVs, indicating the high-energy vortex is drawing nearby flow into itself. These patterns appear similar to the *u'v'* and suggest a relationship between the two parameters. They help identify the

shear layer between the vortex and the freestream flow as well as the location of the fence.

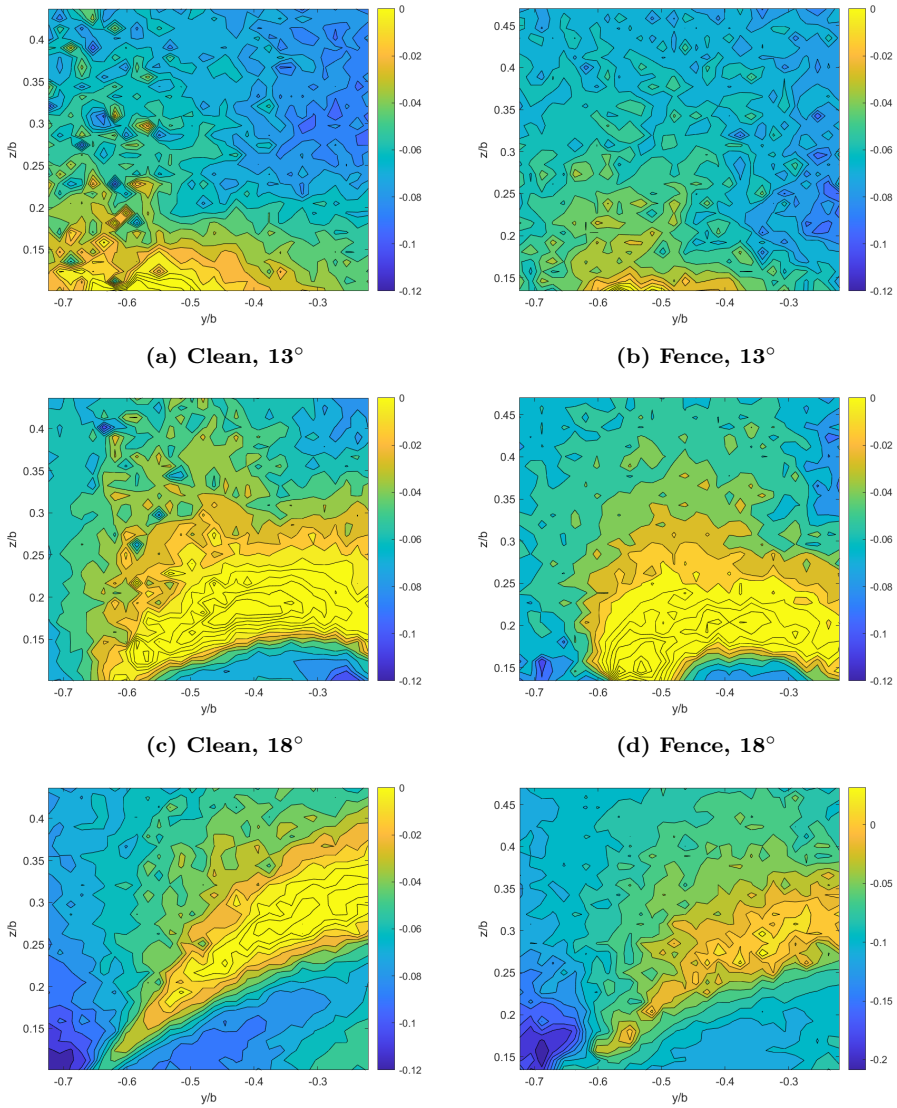

(a) Clean, 13° **(b) Fence, 13°**

(c) Clean, 18° **(d) Fence, 18°**

(e) Clean, 23° **(f) Fence, 23°**

Figure 60. Non-dimensional W-velocity; at DP 1

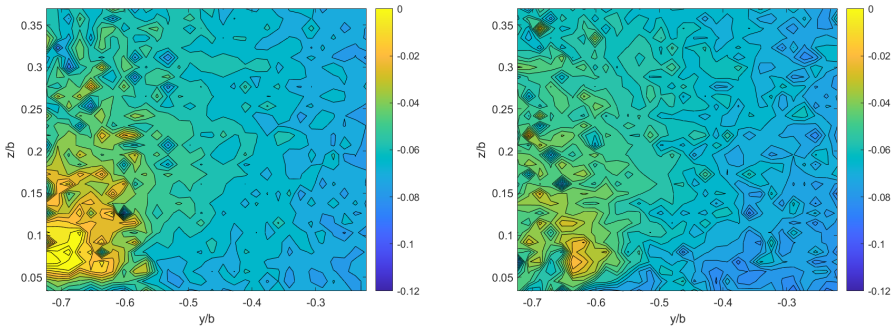

(a) Clean, 13° **(b) Fence, 13°**

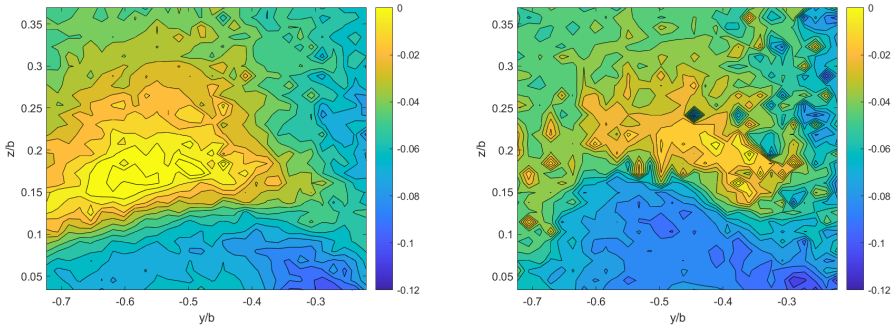

(c) Clean, 18° **(d) Fence, 18°**

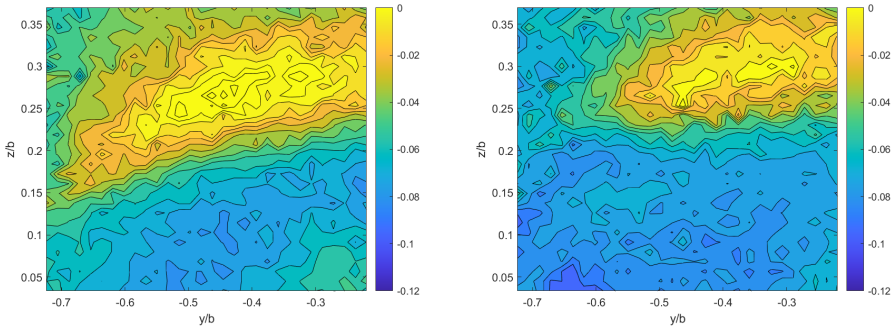

(e) Clean, 23° **(f) Fence, 23°**

Figure 61. Non-dimensional W-velocity; at DP 2

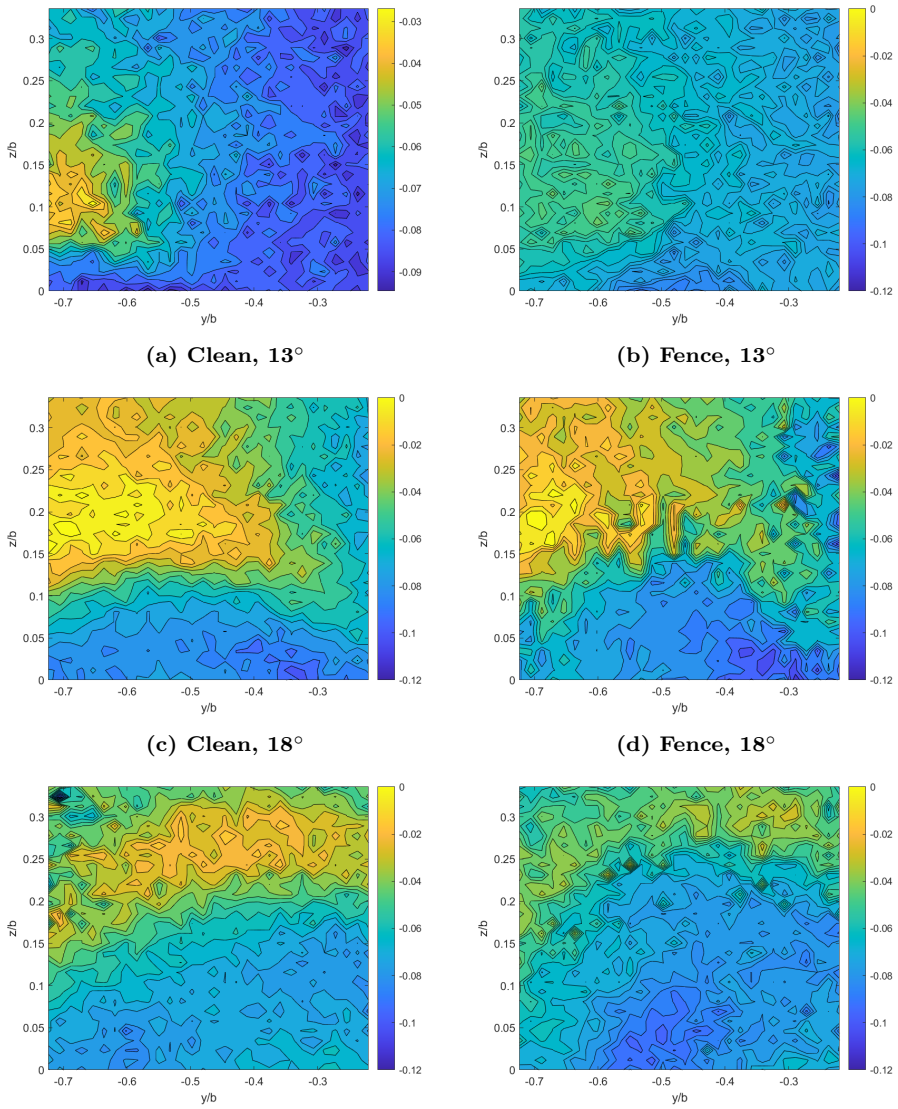

(a) Clean, 13° **(b) Fence, 13°**

(c) Clean, 18° **(d) Fence, 18°**

(e) Clean, 23° **(f) Fence, 23°**

Figure 62. Non-dimensional W-velocity; at DP 3

4.2.7 Vortex Identification Hot Wire Results

The enlarged data planes used to capture both the wing tip vortex and LEV are presented. The migration of the LEV are consistent with the data found in the separation region data planes and more regarding the relationship between the LEV and wing tip vortices is readily observed. All of the following data is arranged as follows. The left-most column shows the clean configuration, the middle column

shows the passive BLF configuration, and the right-most column shows the AFC configuration.

Figure 63 shows the vorticity contours in enlarged data plane at DP 3. The AFC configuration shows the most dramatic separation between the LEV and the wing tip vortex indicating the two vortices stay coherent for longer than the clean and fenced configurations. This is consistent with the earlier tuft data. The passive BLF configuration shows spillage from the primary LEV outboard, making the two vortices less distinct as the AoA increases.

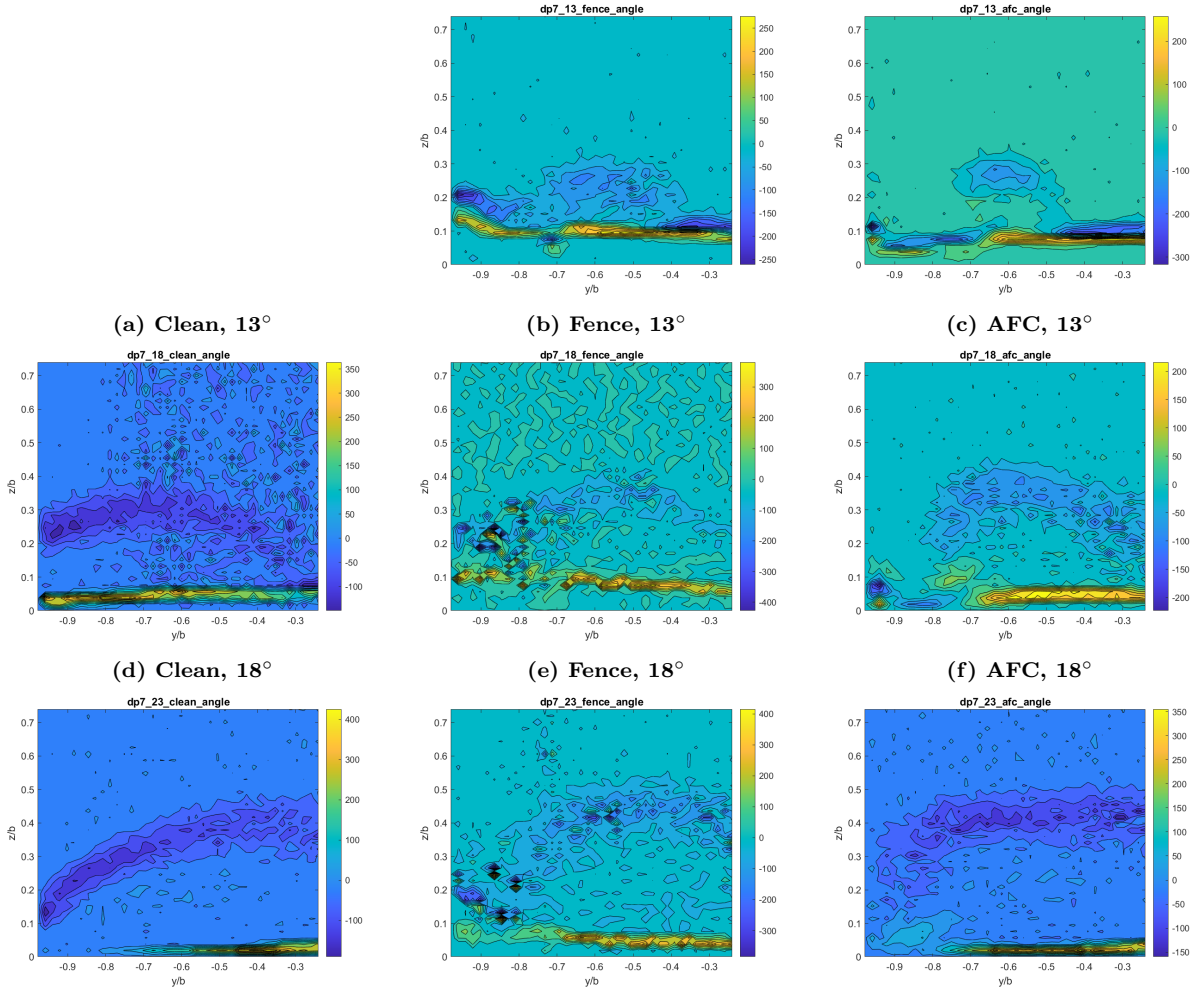

(a) Clean, 13° **(b) Fence, 13°** **(c) AFC, 13°**

(d) Clean, 18° **(e) Fence, 18°** **(f) AFC, 18°**

(g) Clean, 23° **(h) Fence, 23°** **(i) AFC, 23°**

Figure 63. Vorticity contours; at DP 3

Figure 64 shows the non-dimensional streamwise velocity contours at DP 3. The clean configuration still demonstrates a coalesced LEV and wing tip vortex above 18°. Similar to the discussion of the vorticity at this same DP, the truncation of outboard motion is evident in the AFC case. The regions of highest vorticity magnitude are just above the locations of greatest velocity deficit. Additionally, there is a consistent streak of high vorticity noted in the vicinity of the trailing edge.

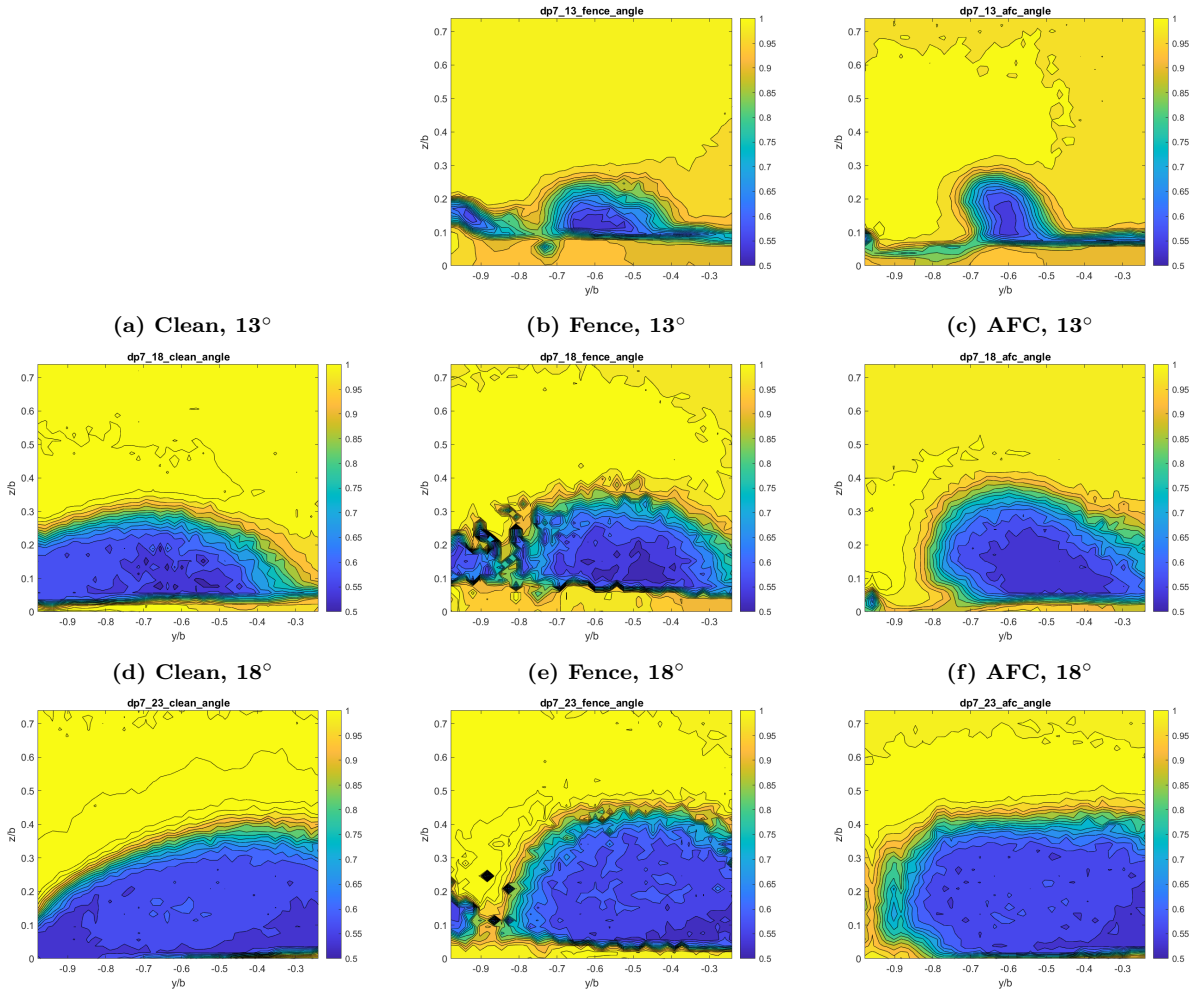

(a) Clean, 13° **(b) Fence, 13°** **(c) AFC, 13°**

(d) Clean, 18° **(e) Fence, 18°** **(f) AFC, 18°**

(g) Clean, 23° **(h) Fence, 23°** **(i) AFC, 23°**

Figure 64. Non-dimensional U-velocity contours; at DP 3

Figure 65 shows the vorticity contours in enlarged data plane at DP 4. Three

inches aft of the previous state, the vorticity magnitudes and locations show consistency for the passive and active flow control configurations and slight growth in the clean configurations. The AFC LEV maintains the greatest distance from the 70% spanwise slot location indicating the blowing impacts the migration of the vortex more than the clean and passive BLF configurations.

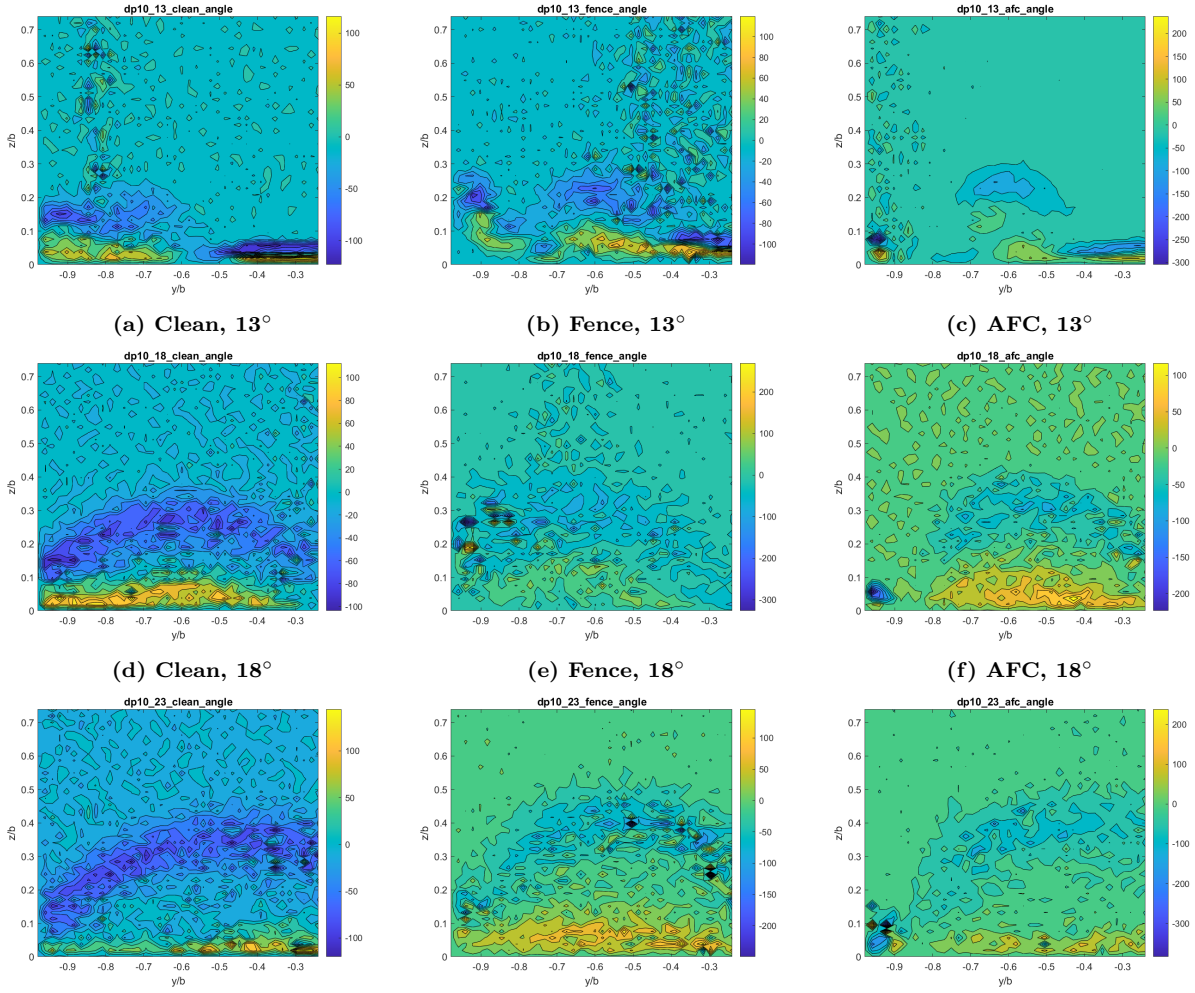

(a) Clean, 13° **(b) Fence, 13°** **(c) AFC, 13°**

(d) Clean, 18° **(e) Fence, 18°** **(f) AFC, 18°**

(g) Clean, 23° **(h) Fence, 23°** **(i) AFC, 23°**

Figure 65. Vorticity contours; at DP 4

Figure 66 shows the non-dimensional streamwise velocity contours at DP 4. The growth of the velocity deficit region is evident between DP 3 and DP 4. Even still, there is evident separation between the wing tip vortex and LEV up to 23°

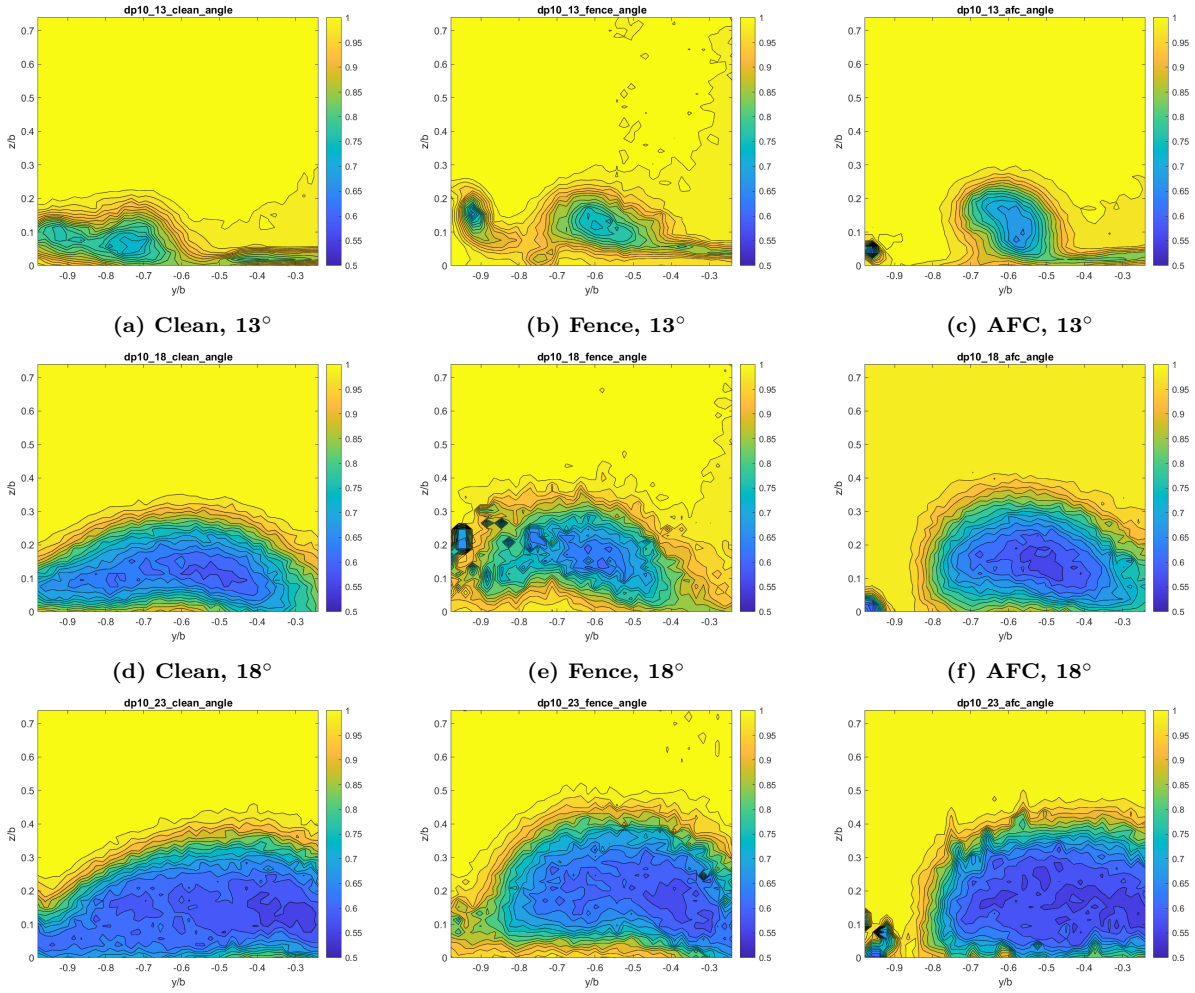

(a) Clean, 13° **(b) Fence, 13°** **(c) AFC, 13°**

(d) Clean, 18° **(e) Fence, 18°** **(f) AFC, 18°**

(g) Clean, 23° **(h) Fence, 23°** **(i) AFC, 23°**

Figure 66. Non-dimensional U-velocity contours; at DP 4

V. Conclusions and Recommendations

5.1 Conclusions

The comparative benefits of AFC boundary layer fences (BLF) to their passive counterparts were quantitatively determined in Demoret (2020) and Tedder (2021) using global force tracking, both experimentally and computationally. The differences were qualitatively studied in the present study using flow visualization methods, such as tuft planes, CTA triple wire traverse, and computational fluid dynamics post-processing. The use of active flow control (AFC) devices was shown to improve aerodynamic performance of a generic cropped delta wing by strengthening the primary LEVs and reducing spanwise flow in the boundary layer. These AFCs increase the maximum lift coefficient by mitigating spanwise flow at outboard locations by severing its propagation. An adverse pressure gradient constrains the flow and resets its direction outboard of the slot. The AFC also strengthens LEVs by injecting momentum in the boundary layer by entrainment. In addition, the use of AFC reduces the drag penalty commonly associated with passive BLFs.

The movement of the wing tip and LEVs were found to be consistent with literature. The evolution and inward migration of the leading edge vortices (LEV) are by both changes in configuration and angle of attack. It is shown in the present study for AFC that the LEVs migrate inboard as the angle of attack increases and begin to breakdown at 18°. The vortices do not fully breakdown until after 23°. By 28°, the vortex core is separated. The reason for this inboard migration against the spanwise flow is attributed to an adverse pressure gradient forming at the wing tip, which was determined by visualizing CFD data on the surface of the wing. This wing tip pressure gradient creates a wall of air that opposes the impinging vortex, causing it to curve inboard. The size of the pressure gradient grows with increases in angle

of attack.

The same trend is true for the passive BLF configuration, albeit less pronounced. The reverse flow is found to expand outward from the center of the LEV core until it comprises most of the separated flow region and LEV. This is consistent with Hitzel et al. (2016) in his explanation of the propagation and evolution of the primary leading edge vortex on a delta wing. When the flow begins its recirculating motion, the LEV bleeds energy and its coalesced core begins breaking down. This is manifested in a drop in the local velocity, which increases the local pressure. This increase in pressure on the suction surface accounts for a global loss of lift felt by the wing.

Turbulence intensity, turbulent kinetic energy, and two components of the Reynolds stress were evaluated to validate the computational data and turbulence model. The turbulent kinetic energy was useful in identifying the vortex centers and shear layers which were used to later quantify the vortex circulation estimates. The circulation was considered for its correlation to lift. Localizing the circulation in just the LEV helped to identify the configurations in which the vortices contributed most to the wing's global lift. In the near-body wake (x/c ¡ 100%), the circulation of the clean wing's leading edge vortex was found to be highest. Moving aft of the trailing edge, the trend reversed and the flow control devices demonstrated the highest vortex cirulation.

5.2 Recommendations

By tracing observable, qualitative phenomena present in the flow field behind the wings in this study to their quantitative performance enhancements noted in past studies, more specific inferences about performance improvements and optimizations can be made in future efforts. Some of these efforts may benefit from alternative visualizations, such as smoke, heated Schlieren, particle image velocimetry (PIV),

and focused computational studies examining wake structures. Additionally, greater resolution in the data collected and subsequent validation of force and moment coefficients would provide valuable insight to a generalized understanding of delta wing performance.

The turbulence data collected by means of the hot wire may serve as an appropriate starting point for refining CFD turbulence models. The lift and drag data provided in Demoret (2020) the wake characterization discussed in the present study could provide a valuable pool of experimental data used to validate future in-depth CFD studies.

Appendix A: Reference Images

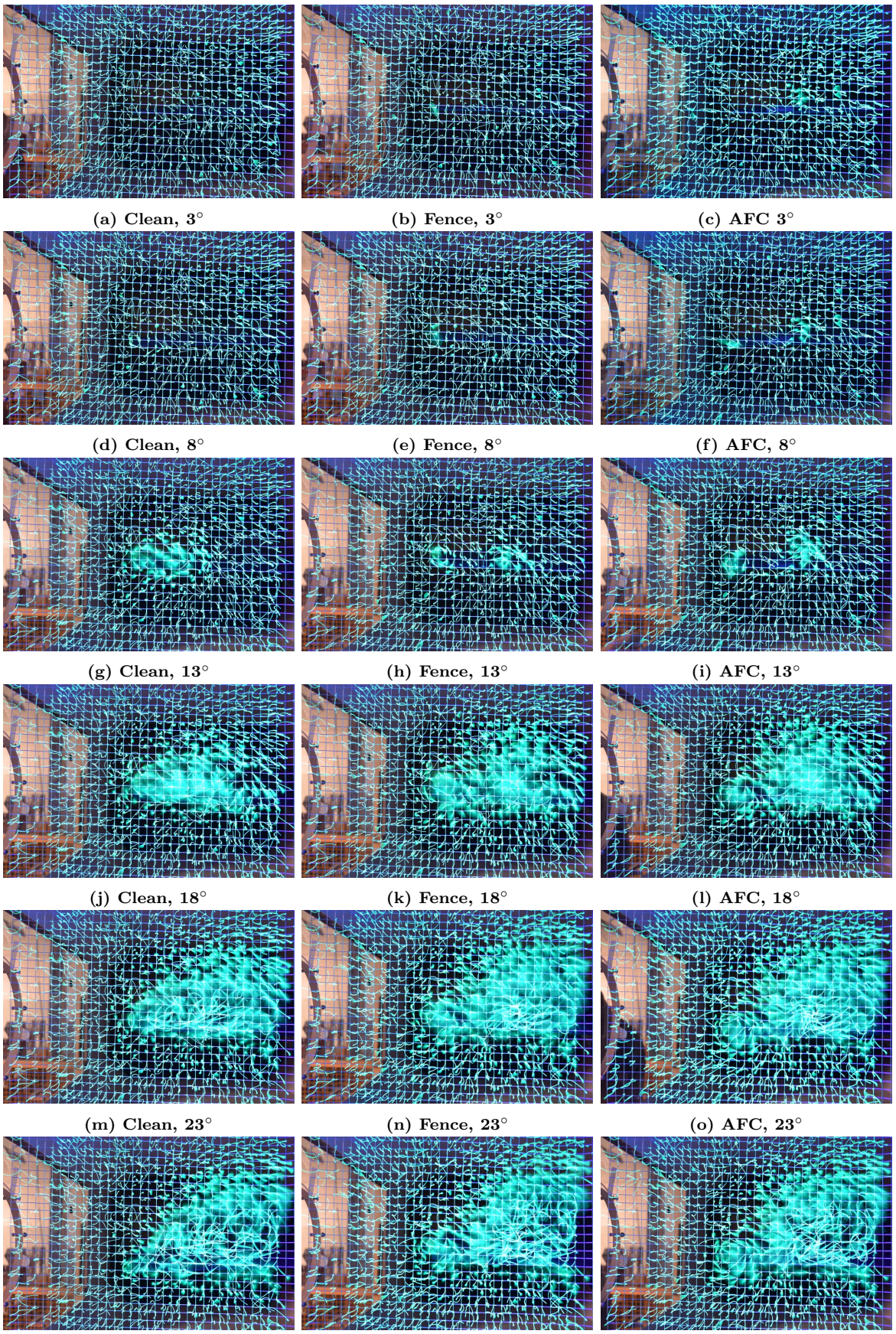

(a) Clean, 3° (b) Fence, 3° (c) AFC 3°

(d) Clean, 8° (e) Fence, 8° (f) AFC, 8°

(g) Clean, 13° (h) Fence, 13° (i) AFC, 13°

(j) Clean, 18° (k) Fence, 18° (l) AFC, 18°

(m) Clean, 23° (n) Fence, 23° (o) AFC, 23°

(p) Clean, 28° (q) Fence, 28° (r) AFC, 28°

Figure 67. Tuft visualization 1.5" aft of trailing edge

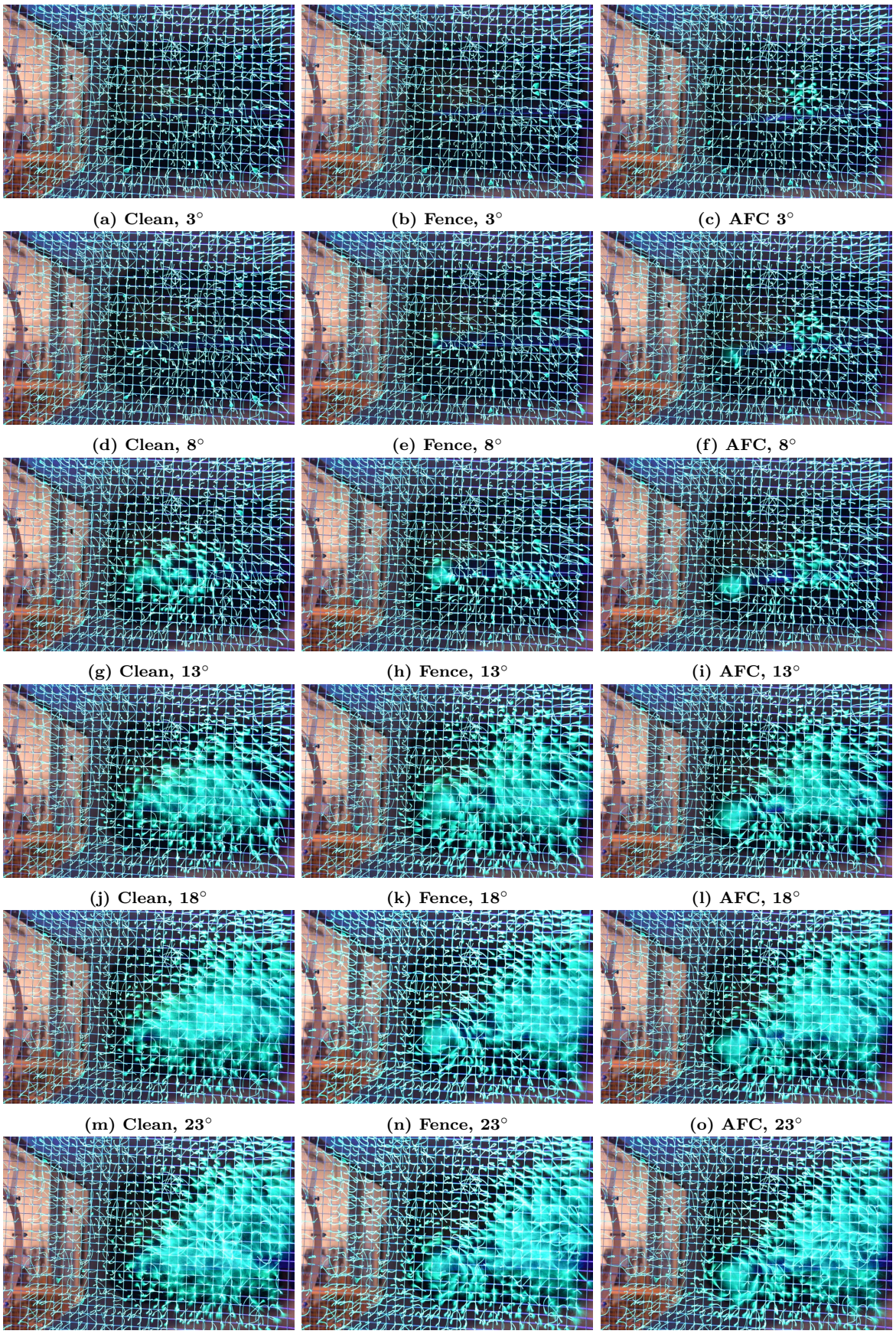

(a) Clean, 3° (b) Fence, 3° (c) AFC 3°

(d) Clean, 8° (e) Fence, 8° (f) AFC, 8°

(g) Clean, 13° (h) Fence, 13° (i) AFC, 13°

(j) Clean, 18° (k) Fence, 18° (l) AFC, 18°

(m) Clean, 23° (n) Fence, 23° (o) AFC, 23°

(p) Clean, 28° (q) Fence, 28° (r) AFC, 28°

Figure 68. Tuft visualization 4.5" aft of trailing edge

Appendix B: MATLAB Hot Wire Data Visualization Code

```
clear; clc; close all;
input = [filename]

%Call function to plot data from hotwire raw data
lenInput = length(input);
for i = 1:lenInput
    [vecName(i), maxtke(i), Gamma(i)] = plotter(input(i));
end
maxGam = max(Gamma(:));

GammaNorm = Gamma/maxGam;

array = [vecName;GammaNorm]
%% Functions
function [vecName, maxtke, Gamma] = plotter(name)
dat = importdata(name);
vecName = erase(name,".txt");

% Plot Switchboard
U_true = 0;
V_true = 0;
Tu_true = 0;
tke_true = 1;
reyn_true = 0;
```

```
halfspan = 298;
leny = 30;
Y = -dat.data(:,2);
Y2 = dat.data(:,2);
Z = -dat.data(:,3);
U = dat.data(:,4);
urms = dat.data(:,5);
W = -dat.data(:,6);
wrms = -dat.data(:,7);
V = -dat.data(:,8);
vrms = -dat.data(:,9);
isUV = contains(name,'uv');

if isUV == true
    uv = dat.data(:,10);
    vw = dat.data(:,11);
    uw = dat.data(:,12);
end

if contains(name,'z60')==true
    Z = Z+60;
elseif contains(name,'z20')==true
    Z = Z+20;
elseif contains(name,'z80')==true
    Z = Z+80;
end
```

```
dz = (Z(2)-Z(1))/(2*halfspan);
dy = (Y(leny+1)-Y(1))/(2*halfspan);

VV = sqrt(U.^2+V.^2+W.^2);
vrms_mean = mean(vrms);
wrms_mean = mean(wrms);

Ymax = max(Y);
Zmax = max(Z);

%This loop breaks the interlaced data into intended rectangular grid within
%a new matrix
for i = 1:leny
    for j = 1:leny
        Ym(i,j) = -((Y(i+(j-1)*leny)-Ymax));
        Zm(i,j) = Z(i+(j-1)*leny);
        Um(i,j) = sqrt((U(i+(j-1)*leny))^2);
        Um_rms(i,j) = sqrt((urms(i+(j-1)*leny))^2);
        Vm_rms(i,j) = sqrt((urms(i+(j-1)*leny))^2);
        Wm_rms(i,j) = sqrt((urms(i+(j-1)*leny))^2);
        Vm(i,j) = V(i+(j-1)*leny);
        Wm(i,j) = W(i+(j-1)*leny);
        VVm(i,j) = VV(i+(j-1)*leny);
        if isUV == true
            uvm(i,j) = uv(i+(j-1)*leny);
```

```
            vwm(i,j) = vw(i+(j-1)*leny);
            uwm(i,j) = uw(i+(j-1)*leny);
        end
    end
end

Ym = (-Ym/2)/298-0.22;
Zm = (Zm/2)/298;
%This loop flips every other row, restoring the intended path of the data

for j = 1:floor(leny/2)
    Zm(:,2*(j)) = flip(Zm(:,2*j));
    Um(:,2*(j)) = flip(Um(:,2*j));
    Um_rms(:,2*(j)) = flip(Um_rms(:,2*j));
    Vm_rms(:,2*(j)) = flip(Vm_rms(:,2*j));
    Wm_rms(:,2*(j)) = flip(Wm_rms(:,2*j));
    Vm(:,2*(j)) = flip(Vm(:,2*j));
    Wm(:,2*(j)) = flip(Wm(:,2*j));
    VVm(:,2*(j)) = flip(VVm(:,2*(j)));
    if isUV == true
        uvm(:,2*(j)) = flip(uvm(:,2*(j)));
        vwm(:,2*(j)) = flip(vwm(:,2*(j)));
        uwm(:,2*(j)) = flip(uwm(:,2*(j)));
    end
end
```

```
Y = -(Y2/2)/298+0.269;
Z = (Z/2)/298;
Um_mean = mean(Um);
Vm_mean = mean(Vm);
Wm_mean = mean(Um);
newName = erase(name,".txt");

% Compute turbulence intensity
meanu = mean(Um(1,:));
maxu = Um(30,1);
Tu = (Um_rms./maxu)

tke = .5*(Um_rms.^2+Vm_rms.^2+Vm_rms.^2)./meanu^2;
maxtke = max(tke(:));

% Find the indices corresponding to values of tke/maxtke higher than 70%
[row, col] = find(tke/maxtke>0.7);
lenCol = length(col);
Vsum = 0;

for i = 1:lenCol
    Vsum = Vsum+VVm(row(i),col(i));
end

% Compute the vorticity numerically
for i=1:leny-1
```

```
    for j=1:leny-1
        vorticity(i+1,j+1) = (Vm(i+1,j)-Vm(i,j))/dz-(Wm(i,j+1)-Wm(i,j))/dy
    end
end

Gamma = 2*Vsum*lenCol*dz*dy;
if U_true == 1
    % plot normalized mean U velocity
    figure;
    contourf(Ym,Zm,-(Um-maxu)/meanu,15)
    xlabel('y/b')
    ylabel('z/b')
    colorbar
    caxis([0 .3])
    saveas(gcf,newName,'png')
end
if V_true == 1
    % plot normalized mean V velocity
    figure;
    contourf(Ym,Zm,(Vm)/meanu,15)
    xlabel('y/b')
    ylabel('z/b')
    colorbar
    caxis([-0.16 -0.02])
    saveas(gcf,append(newName,'_Vm'),'png')
end
```

```
if Tu_true == 1
    % plot normalized mean V velocity
    figure;
    contourf(Ym,Zm,Tu,15)
    xlabel('y/b')
    ylabel('z/b')
    colorbar
    caxis([.1  .35])
    saveas(gcf,append(newName,'_Tu'),'png')
end
if tke_true == 1
    % plot normalized mean V velocity
    figure;
    contourf(Ym,Zm,tke/maxtke,[.7:0.005:1],':')
    xlabel('y/b')
    ylabel('z/b')
    colorbar
    saveas(gcf,append(newName,'_tke'),'png')
end
if contains(name,'uv') == true && reyn_true == 1
    % plot normalized mean V velocity
    figure;
    contourf(Ym,Zm,uwm)
    xlabel('y/b')
    ylabel('z/b')
    colorbar
```

```
    caxis([-10  0])
    saveas(gcf,append(newName,'_uv'),'png')
end
end
```

Bibliography

Anderson, J. D. (2017), *Fundamentals of Aerodynamics*, 6th edn, McGraw-Hill, New York, NY.

Barlow, J. B., Rae, W. H., Pope, A. and Wiley, J. (2015), *Low Speed Wind Tunnel Testing*, Vol. 7, & Sons.

Brown, C. E. and Michael, W. H. (1954), 'Effect of leading-edge separation on the lift of a delta wing', *Journal of the Aeronautical Sciences* **21**(10), 690–694.

Burtsev, A., He, W., Hayostek, S., Zhang, K., Theofilis, V., Taira, K. and Amitay, M. (2021), 'Linear modal instabilities around post-stall swept finite-aspect ratio wings at low reynolds numbers'.

De Giorgi, M. G., De Luca, C. G., Ficarella, A. and Marra, F. (2015), 'Comparison between synthetic jets and continuous jets for active flow control: Application on a naca 0015 and a compressor stator cascade', *Aerospace Science and Technology* **43**, 256–280.

Demoret, A. C. (2020), The effect of passive boundary-layer fences on delta wing performance at low reynolds number, Master's thesis, Air Force Institute of Technology.

Demoret, A. C., Walker, M. M. and Reeder, M. F. (2020), The Effect of Passive Boundary-Layer Fences on Delta Wing Performance at Low Reynolds Number, *in* 'AIAA Scitech 2020 Forum', AIAA.

Fink, N. T. (2015), 'Numerical analysis of incipient separation on 53 degree swept diamond wing'.

Gad-el Hak, M. (2000), *Flow Control: Passive, Active, and Reactive Flow Management*, Cambridge University Press.

Gamble, B. J. and Reeder, M. F. (2009), 'Experimental analysis of propeller-wing interactions for a micro air vehicle', *Journal of Aircraft* **46**(1), 65–73.

Harper, C. W. and Maki, R. L. (1964), A review of the stall characteristics of swept wings, Technical report, NASA.

Hitzel, S. M., Boelens, O. J., Rooij, M. and Hövelmann, A. (2016), 'Vortex development on the avt-183 diamond wing configuration – numerical and experimental findings', *Aerospace Science and Technology* **57**, 90–102.

Luckring, J. M. (2004), 'Reynolds number, compressibility, and leading-edge bluntness effects on delta-wing aerodynamics'.

Marzanek, M. F. (2019), 'Separated flows over non-slender delta wings by', (April).

Naigle, S. C., Hiltner, S. D. and Walker, M. M. (2022), 'Numerical optimization of a vortex generating jet on a non-slender delta wing'.

Ol, M. V. and Gharib, M. (2003), 'Leading-edge vortex structure of nonslender delta wings at low reynolds number'.

Polhamus, E. C. (1996), A survey of reynolds number and wing geometry effects on lift characteristics in the low speed stall region, Technical report, NASA.

Pope, S. B. (2000), *Turbulent Flows*, 1st edn, Cambridge University Press, New York, NY.

Sivells, C. and Neely, R. H. (1947), Method for calculating wing characteristics by lifting-line theory using nonlinear section lift data, Technical report, University of Kansas Center for Research, Inc.

Tedder, N. L. (2021), 'Optimizing design parameters for active flow control boundary-layer fence performance enhancement on a delta wing', p. 174.

Tousi, N., Coma, M., Bergadà, J., Pons-Prats, J., Mellibovsky, F. and Bugeda, G. (2021), 'Active flow control optimisation on sd7003 airfoil at pre and post-stall angles of attack using synthetic jets', *Applied Mathematical Modelling* **98**, 435–464.

Walker, M. M. (2007), The Aerodynamic Performance of the Houck Configuration, Master's thesis, Air Force Institute of Technology.

Walker, M. M. (2018), Replicating the Effects of a Passive Boundary-Layer Fence with Active Flow Control, PhD thesis, Ohio State University.

Wang, X., Yan, J., Dhupia, J. S. and Zhu, X. (2021), 'Active flow control based on plasma synthetic jet for flapless aircraft', *IEEE Access* **9**, 24305–24313.

Wentz, W. H. and Kohlman, D. L. (1968), Wind Tunnel Investigations of Vortex Breakdown on Slender Sharp-Edged Wings, Technical report, University of Kansas Center for Research, Inc.

Williams, M. D., Reeder, M. F., Maple, R. C. and Solfelt, D. A. (2010), 'Modeling, simulation, and flight tests for a T-38 Talon with wing fences', *Journal of Aircraft* **47**(2), 423–433.

REPORT DOCUMENTATION PAGE

Form Approved
OMB No. 0704–0188

1. REPORT DATE *(DD–MM–YYYY)*	2. REPORT TYPE	3. DATES COVERED *(From — To)*
22–02–2022	Master's Thesis	August 2020 — March 2022

4. TITLE AND SUBTITLE

Characterizing Wake Roll-Up and Vortex Structure for Delta-Wing Configurations Featuring Flow-Control Devices at Low Reynolds Number

5a. CONTRACT NUMBER

5b. GRANT NUMBER

5c. PROGRAM ELEMENT NUMBER

6. AUTHOR(S)

Layng, Jeffrey M., Capt, USAF

5d. PROJECT NUMBER

5e. TASK NUMBER

5f. WORK UNIT NUMBER

7. PERFORMING ORGANIZATION NAME(S) AND ADDRESS(ES)

Air Force Institute of Technology
Graduate School of Engineering and Management (AFIT/EN)
2950 Hobson Way
WPAFB OH 45433-7765

8. PERFORMING ORGANIZATION REPORT NUMBER

AFIT-ENY-MS-M-303

9. SPONSORING / MONITORING AGENCY NAME(S) AND ADDRESS(ES)

Air Force Research Lab
Dr. Aaron Altman, RQVA Technical Advisor
2130 8th St
Wright-Patterson AFB, OH 45433
aaron.altman.1@us.af.mil

10. SPONSOR/MONITOR'S ACRONYM(S)

11. SPONSOR/MONITOR'S REPORT NUMBER(S)

12. DISTRIBUTION / AVAILABILITY STATEMENT

Approval for public release; distribution is unlimited.

13. SUPPLEMENTARY NOTES

14. ABSTRACT

Various configurations of a cropped delta wing featuring a NACA 0012 wing-section were evaluated experimentally at a Reynolds number of 5.0 x 10^5 in the Air Force Institute of Technology Low-Speed Wind Tunnel facility. The effects of active flow control (AFC) and passive boundary-layer fences (BLF) were shown to improve high angle of attack delta wing performance. The AFC BLFs were shown to replicate the performance enhancements found in passive BLFs without incurring a drag penalty. An experimental characterization of the wake region is presented to compare the wake roll-up and leading edge vortices for these baseline, passive BLF, and AFC BLF delta wing configurations. Using a tuft mesh and a constant temperature anemometry triple wire probe, the wake was characterized at several discrete planes of interest aft of the trailing edge. This wake data was used to elucidate causes for AFC BLF configuration increasing the maximum lift coefficient by 60.3% . The present study shows this aerodynamic improvement is largely attributed to: 1) strengthening the leading edge vortex (LEV), which delays vortex breakdown, and 2) truncating spanwise flow.

15. SUBJECT TERMS

aerodynamics, delta wing, vortices, wake, active flow control, wing performance, NACA 0012, blunt leading edge

16. SECURITY CLASSIFICATION OF:			17. LIMITATION OF ABSTRACT	18. NUMBER OF PAGES	19a. NAME OF RESPONSIBLE PERSON
a. REPORT	b. ABSTRACT	c. THIS PAGE			Lt Col Michael Walker, AFIT/ENY
U	U	U	U	122	19b. TELEPHONE NUMBER *(include area code)* (937) 255-3636, x4444; michael.walker@afit.edu